ON TWO THEORIES FOR BRITTLE FRACTURE: MODELING AND DIRECT NUMERICAL SIMULATIONS

A Dissertation

by

MALLIKARJUNAIAH SIDDAPURA MUDDAMALLAPPA

Submitted to the Office of Graduate and Professional Studies of
Texas A&M University
in partial fulfillment of the requirements for the degree of

DOCTOR OF PHILOSOPHY

Chair of Committee,	Jay R. Walton
Committee Members,	Wolfgang Bangerth
	Prabir K. Daripa
	K. R. Rajagopal
Head of Department,	Emil Straube

December 2015

Major Subject: Mathematics

ABSTRACT

The work presented in this dissertation focuses on extending a recent effort of developing brittle fracture theory with an aim of achieving bounded crack-tip stress and strain without the use of extra near-tip cohesive surface. The first model studied in this dissertation is attributed to modeling the bulk material response in the context of nonlinear strain-limiting theory elasticity. The second model is a theory of fracture developed by Sendova and Walton based on incorporation of surface mechanics. In the first part of this dissertation, we analyze the nonlinear fracture model using a combination of asymptotic and numerical arguments. We find that the use of nonlinear response relations, for a special case of plane-strain fracture, leads to a highly nonlinear partial differential equation. We obtain an asymptotic solution to this nonlinear boundary value problem and subsequently develop a numerical model using an adaptive finite element method.

In the second part of the dissertation, a main focus is to implement the surface-mechanics class of fracture theory developed by Sendova and Walton using a stable numerical method such as finite elements. If the surface-tension is assumed to be dependent linearly on the in-plane curvature, the resulting jump momentum balance boundary condition will contain higher-order tangential derivatives. We present a reformulation of the crack-surface boundary condition using the boundary Green's function and Hilbert' transform (as Dirichlet-to-Neumann map) and subsequently implemented the model using an adaptive finite element method.

Both the models, studied in this work, predict a physically reasonable crack-tip strain compared to the singular prediction from the linearized elasticity model. More-

over, the crack-tip stress predicted by both the models remain smaller in magnitude compared to the corresponding prediction from the classical linearized model. Finally, since the two models studied in this dissertation do not indicate the singular stress growth in the vicinity of the crack-tip, the crack-tip is not a singular energy sink. Therefore, the classical fracture criterion based upon the singular solution such as Stress Intensity Factor (SIF) or local Energy Release Rate (ERR) is not available. For the nonlinear plane-strain fracture model, we study the behavior of the Critical Crack-Tip Stress as a possible fracture criterion. The numerical results indicate that the cleavage stress is maximum along the line directly ahead of the crack-tip and this result is in agreement with the classical linearized elastic fracture mechanics solution for pure mode-I loading.

DEDICATION

To my parents.

ACKNOWLEDGEMENTS

First and foremost I would like to submit my deepest gratitude to my dissertation advisor Professor Jay R. Walton for his invaluable guidance and support in my research project. I feel privileged to be advised by such an outstanding applied mathematician and generous mentor. I would also like to thank him for his advice on various other topics such as teaching, job search, professional talks and writing style. All his guidance will be a great source for me to advance in my academic career.

I would like to thank Professor K. R. Rajagopal for agreeing to be a member of my dissertation committee and also for providing his insightful suggestions on my research topic. Without his own research on *implicit theory of elasticity* and invaluable guidance, practically half of my dissertation wouldn't have been written. His class on nonlinear solid mechanics was very important to my research project.

I am also grateful to Professor Wolfgang Bangerth for helping me with questions on the deal.II library. I extremely appreciative of his patience in going through and answering my questions regarding code-development, finite elements and numerical method for solving nonlinear equations. I also would like to thank him for all his valuable comments and suggestions to improve the quality of my dissertation.

I also thank Professor Prabir Daripa for serving on my dissertation committee and providing many insightful comments and questions on my research topic. I thank all my professors at Texas A&M University with whom I took classes and they all made me what I am today.

I would like to thank the Department of Mathematics at Texas A&M University for the wonderful research facility offered to me during last six years. I express my thanks to previous and the current associate head of graduate studies for all the mentorships.

I wish to thank Ms. Monique Stewart for all her help in completing the required paper works on time. I am also very appreciative of the financial support provided by the Department of Mathematics and the Air Force Office of Scientific Research through Grant FA9550-08-1-0090.

I would also like to thank my friends Fahad Alrashed, Jun Ren, Vladimir Tomov for their friendship and selflessly helping me whenever I needed. My special thanks goes to two of my advisor's previous students Kun Gou and Lauren Ferguson, who have helped me immensely with whatever research as well as technical difficulties I have encountered.

I would also like to acknowledge Professor Dambaru Bhatta and his family from Edinburg, Texas, for their warm care and encouragement from the day both me and my wife landed in America for our higher studies.

I am grateful to both my family and my in-law's family in India for all their support during my studies in America and they were always a great source of comfort during my hard times. I am falling short of words to express my love and appreciation for my wife Veena and my son Mahit, both were integral part of my life at Texas A&M University. I thank both of them whole heartedly for their love and support.

And finally, I would like to thank god for all the blessings in my life.

NOMENCLATURE

BVP	Boundary Value Problem
DEAL.II	Differential Equations Analysis Library
DOF	Degrees of Freedom
DMB	Differential Momentum Balance
FEM	Finite Element Method
LEFM	Linearized Elastic Fracture Mechanics
IVP	Initial Value Problem
JMB	Jump Momentum Balance
ODE	Ordinary Differential Equation
PDE	Partial Differential Equation

TABLE OF CONTENTS

Page

LIST OF FIGURES

FIGURE Page

LIST OF TABLES

TABLE Page

1. INTRODUCTION*

This chapter provides an introduction to the phenomenon of brittle fracture modeling and direct numerical simulations. Beginning with a motivation for studying brittle fracture modeling in the context of strain-limiting theory of elasticity in Section 1.1, the relevant nonlinear response relations are discussed in Section 1.2. Finally, in Section 1.3, a brittle fracture model with surface-tension as excess property is outlined.

1.1 Motivation

The classical linearized elastic fracture mechanics (LEFM), one of the widely celebrated and most successful theories of applied mechanics, has the well-known inconsistency of predicting stress and strain singularities in the crack-tip neighborhood while the governing equations of LFEM are derived on the assumption of uniform infinitesimal strains. Also, it predicts an elliptical crack-opening profile and a blunt crack-tip. Therefore, a large number of studies have been devoted towards correcting these theoretical underpinnings by introducing a two dimensional Barenblatt-type cohesive zone or three dimensional process zone near the crack-tip [9]. However, these ad hoc representations are difficult to validate experimentally and also parameters involved may not have a clear physical meaning.

It is well documented in the *Fracture Mechanics* literature [9, 21] that within the classical linearized theory of elasticity both stress and strain has $\frac{1}{\sqrt{r}}$ order of singularity, where r is the radial distance from the crack-tip. Clearly no real materials can withstand infinite stresses and predict singular strain filed near the crack-tip. The

*Part of this chapter is reprinted with permission from Springer publications, "On the direct numerical simulation of plane-strain fracture in a class of strain-limiting anisotropic elastic bodies" by S. M. Mallikarjunaiah, J. R. Walton, *International Journal of Fracture*, 192(2), 217-232, 2015; Copyright 2015 by Springer Publications.

crack-tip strain singularity may be attributed to the two important factors, first is the "linear" relationship between stress and strain and second is the classical traction-free crack-face boundary condition. The classical linearized elasticity approach to modeling the material response is proved to be useful in predicting the stress-strain fields in the bulk material "far" away from the crack-tip. But the these models predict a highly inaccurate results near the crack-edge. Therefore, there is a great scope for developing new constitutive models resulting from augmenting the classical models to incorporate the crack-surface effects that might yield improved near-tip stress-strain predictions.

A large number of archiving literature is devoted towards understanding the fracture through *atom-to-continuum* modeling, such as molecular dynamics (for more information see [1]). Another continuum model reformulation is the bond-force based *peridynamic* approach [50] of modeling cracks and fracture. This nonlocal formulation introduces a new force between any two atoms in a horizon. More importantly the *peridynamic* theory is a nonlocal numerical tool, hence a great deal of computational cost is required for the simulation because each particle will interact with its neighbors within the horizon. A main aspect of this nonlocal theory is that integration rather than the differentiation is used to define *force* between material particles. Another serious issue is constructing the correct *peridynamic*-BVP correspond to the actual experiment.

In all the above mentioned brittle fracture theories, the models do not consider the bulk nonlinear response of solids while deriving the constitutive relations. But, there is a clear experimental evidence on titanium alloys, Gum metal alloys and other alloys (see [54]), that these metals respond nonlinearly even when the strains are below 2.5% [39]. The classical linearized elasticity is incapable of predicting such nonlinear material response. These considerations, among others, motivated a recent

introduction of non-linear, strain limiting theories of elasticity.

In a series of recent papers, Rajagopal [34–40] has offered a new approach to modeling the stress-strain behavior of non-dissipative elastic solids beyond the classical Cauchy and Green formulations. In particular, he notes a need for developing non-linear response relations within infinitesimal strain assumption. Infinitesimal strain approximation to classical Cauchy elasticity always lead to a linear relationship between stress and linearized strain. To derive logically consistent nonlinear relationships between stress and linearized strain, Rajagopal [34] introduces a general approach in which stress and strain are connected through an implicit relation. He shows how one can accommodate linearization procedure to derive nonlinear implicit response relations for linearized strain as a nonlinear function of stress. A special sub-class of such models are strain-limiting in that the norm of strain remains uniformly bounded even as the norm of the stress becomes unbounded. Recently Rajagopal and coworkers [8, 12–17, 26, 27, 32, 33, 38, 41, 42] have studied the classical problems of elasticity within the context of these new class of nonlinear elastic response relations.

1.2 The Model Framework and Notations

In this section we develop the modeling framework by first introducing the kinematical setting and notation we use for classical finite elasticity.

1.2.1 Kinematics and Kinetics of Classical Elasticity

Let $\boldsymbol{X}$ be any arbitrary point in a stress-free reference configuration $\mathcal{B}$ of a material body with $\boldsymbol{x} = \boldsymbol{f}(\boldsymbol{X}, t)$ being the corresponding point in the current configuration and $\boldsymbol{f}$ denotes a deformation of the body. Let $\boldsymbol{u}$ and $\boldsymbol{F}$ denote the displacement and deformation gradient through

$$\boldsymbol{u} := \boldsymbol{x} - \boldsymbol{X}\,, \tag{1.1}$$

and

$$\boldsymbol{F} := \frac{\partial \boldsymbol{f}}{\partial \boldsymbol{X}}\,. \tag{1.2}$$

The left and right Cauchy-Green tensors $\boldsymbol{B}$ and $\boldsymbol{C}$ are defined by

$$\boldsymbol{B} := \boldsymbol{F}\boldsymbol{F}^T \tag{1.3}$$

and

$$\boldsymbol{C} := \boldsymbol{F}^T\boldsymbol{F}\,, \tag{1.4}$$

respectively, and the Green-St. Venant tensor $\boldsymbol{E}$ is defined by

$$\boldsymbol{E} = \frac{1}{2}(\boldsymbol{C} - \boldsymbol{I}). \tag{1.5}$$

Let $\boldsymbol{T}$ denote the *Cauchy Stress Tensor*. Then the first and second *Piola-Kirchhoff Stress Tensors*, $\boldsymbol{S}$ and $\overline{\boldsymbol{S}}$, respectively, are defined by

$$\boldsymbol{S} := \boldsymbol{T}\boldsymbol{F}^{-\mathrm{T}}\det(\boldsymbol{F}) \tag{1.6}$$

and

$$\overline{\boldsymbol{S}} := \boldsymbol{F}^{-1}\boldsymbol{S}. \tag{1.7}$$

A material body is said to be *Cauchy Elastic* if its constitutive class is determined by a response function of the form:

$$\boldsymbol{S} = \widehat{\boldsymbol{S}}(\boldsymbol{F}). \tag{1.8}$$

It is said to be *Green Elastic* (or equivalently *Hyperelastic*) if the stress response

function is the gradient of a scalar valued potential

$$\widehat{\boldsymbol{S}}(\boldsymbol{F}) = \partial_{\boldsymbol{F}} \widehat{w}(\boldsymbol{F}). \tag{1.9}$$

We now show the steps of the linearization of the general constitutive equation (1.8) and derive the governing linearized theory of elasticity. First, note that the deformation gradient defined in (1.2) can be written as

$$\boldsymbol{F} = \mathbf{I} + \nabla \boldsymbol{u}, \tag{1.10}$$

in which $\mathbf{I}$ is the second order Identity tensor. Also assume that the reference configuration is residual stress free, i.e.

$$\widehat{\boldsymbol{S}}(\mathbf{I}) = \mathbf{0}. \tag{1.11}$$

Another crucial assumption in the deriving the linearized theory of elasticity is

$$\nabla \boldsymbol{u} \to \mathbf{0}. \tag{1.12}$$

Then we may conclude from (1.8), (1.10) that

$$\begin{aligned}
\widehat{\boldsymbol{S}}(\boldsymbol{F}) &= \widehat{\boldsymbol{S}}(\mathbf{I} + \nabla \boldsymbol{u}) && (1.13)\\
&= \widehat{\boldsymbol{S}}(\mathbf{I}) + D\widehat{\boldsymbol{S}}(\mathbf{I})\left[\nabla \boldsymbol{u}\right] + o\left(\nabla \boldsymbol{u}\right) && (1.14)\\
&= \mathbb{C}\left[\nabla \boldsymbol{u}\right] + o\left(\nabla \boldsymbol{u}\right) && (1.15)\\
&= \mathbb{C}\left[\boldsymbol{\epsilon}\right] + o\left(\nabla \boldsymbol{u}\right), && (1.16)
\end{aligned}$$

where $\mathbb{C}$ is the fourth order elasticity tensor, $\boldsymbol{\epsilon}$ is the infinitesimal strain tensor and $o(\cdot)$ is the **little-o** notation. Then using (1.16) in (1.8), we obtain the asymptotic form

of the constitutive linearized theory of elasticity as

$$\boldsymbol{S} = \mathbb{C}\left[\boldsymbol{\epsilon}\right] + o\left(\nabla \boldsymbol{u}\right). \tag{1.17}$$

Then within the assumption (1.12) the stress $\boldsymbol{S}$ is a linear function of the infinitesimal strain $\boldsymbol{\epsilon}$, i.e.

$$\boldsymbol{S} = \mathbb{C}\left[\boldsymbol{\epsilon}\right]. \tag{1.18}$$

For an *isotropic* body, the above equation (1.18) can be written as

$$\boldsymbol{S} = 2\,\mu\,\boldsymbol{\epsilon} + \lambda\left(\mathrm{tr}(\boldsymbol{\epsilon})\right)\mathbf{I} \tag{1.19}$$

and for *homogeneous* body, the Lamé parameters μ, λ are constants.

It is important to note that the linearized model given in (1.19) is invertible and one can express the linearized strain $\boldsymbol{\epsilon}$ as a linear function of stress $\boldsymbol{S}$ as

$$\boldsymbol{\epsilon} = \frac{1}{2\mu}\boldsymbol{S} - \frac{\lambda}{2\mu\left(2\mu + 3\lambda\right)}\mathrm{tr}(\boldsymbol{S})\mathbf{I}, \tag{1.20}$$

the above relation (1.20) between the linearized strain and the stress is still linear. More importantly the classical fracture boundary value problem, formulated using the constitutive relation (1.20) along with the traction-free crack-face boundary condition, could still predict singular strains in the neighborhood of the crack-tip. Specifically, both stresses and strains will have $\frac{1}{\sqrt{r}}$ singularity, where r is the radial distance from the crack-tip [9,21]. This is clearly unphysical and violation of the linearization assumption (1.12). Thus it is important to have response relations that predicts bounded strains even when stress becomes *very* large in the near-tip neighborhood. In the following section, we will show a derivation of the nonlinear strain-limiting response relations

within the context of Rajagopal's *Implicit theory* of elasticity [34].

1.2.2 Implicit and Strain-Limiting Constitutive Relations

Rajagopal ([34]) considered isotropic implicit elastic constitutive relations of the form:

$$\mathbf{0} = \mathcal{F}(\boldsymbol{B}, \boldsymbol{T}) \tag{1.21}$$

between the Cauchy stress and left Cauchy-Green tensors. He also considered the special case:

$$\boldsymbol{B} := \mathcal{F}(\boldsymbol{T}) \tag{1.22}$$

with special attention given to *Strain Limiting* theories for which there exists a constant $M > 0$ such that

$$\sup_{\boldsymbol{T} \in \mathrm{Sym}} |\mathcal{F}(\boldsymbol{T})| \leq M. \tag{1.23}$$

As Rajagopal [34] notes, the isotropic form (1.22) has the general representation

$$\boldsymbol{B} = \bar{\alpha}_0 \boldsymbol{I} + \bar{\alpha}_1 \boldsymbol{T} + \bar{\alpha}_2 \boldsymbol{T}^2 \tag{1.24}$$

in which the coefficients $\bar{\alpha}_i \quad i = 0, 1, 2$ are scalar-valued functions of the isotropic invariants:

$$\left\{\rho,\ \mathrm{tr}(\boldsymbol{T}),\ \mathrm{tr}(\boldsymbol{T}^2),\ \mathrm{tr}(\boldsymbol{T}^3)\right\}.$$

1.2.2.1 A Class of Anisotropic Strain-Limiting Models

Mai and Walton [28] introduced a class of strain-limiting models of the form:

$$\boldsymbol{E} = \mathcal{F}(\bar{\boldsymbol{S}}) \tag{1.25}$$

relating the Green-St.Venant strain and Second Piola-Kirchhoff stress tensors with the right-hand-side a uniformly bounded function of $\bar{\boldsymbol{S}}$. The class of models defined by (1.25) give rise to very distinct and interesting nonlinear approximation that is not possible within the classical Cauchy or Green elasticity.

An advantage of (1.25) over (1.22) is that under the assumption of "small" displacement gradients,

$$\sup |\nabla_{\boldsymbol{x}} \boldsymbol{u}| = o(\delta), \quad \delta << 1 \tag{1.26}$$

with $|\cdot|$ denoting the Frobenius norm, it follows that:

$$\boldsymbol{E} = \boldsymbol{\epsilon} + o(|\nabla \boldsymbol{u}|)$$

and hence that (1.25), in the infinitesimal strain regime, can be approximated by:

$$\boldsymbol{\epsilon} = \mathcal{F}(\bar{\boldsymbol{S}}) \tag{1.27}$$

in which $\boldsymbol{\epsilon}$ denotes the customary linearized strain tensor

$$\boldsymbol{\epsilon} := \frac{1}{2}\left(\nabla \boldsymbol{u} + \nabla \boldsymbol{u}^{\mathrm{T}}\right). \tag{1.28}$$

Remark 1: Two natural questions to ask are: (i) Under what conditions does (1.25) have an equivalent Cauchy Elastic formulation? (ii) Under what conditions does (1.25) have an equivalent Green or hyperelastic formulation? The first question concerns the invertibility of the response function $\mathcal{F}(\cdot)$ in (1.25) while the second involves the existence of a complementary energy function for (1.25), that is, a scalar-valued potential $w(\bar{\boldsymbol{S}})$ for which $\mathcal{F}(\bar{\boldsymbol{S}}) = \partial_{\bar{\boldsymbol{S}}} w(\bar{\boldsymbol{S}})$. These questions are addressed below for the specific models employed in the simulations. In particular, use is made of the observation that

a necessary condition for the existence of a complementary energy function for (1.25) is that the Fréchet derivative $\mathrm{D}_{\bar{\boldsymbol{S}}}\mathcal{F}(\bar{\boldsymbol{S}})[\cdot]$ of the response function $\mathcal{F}(\cdot)$ be a self-adjoint, fourth-order tensor when regarded as a linear transformation on Sym, the vector space of symmetric, second-order tensors over $\mathcal{R}^3$.

Another advantage of (1.25) over (1.22) is that it readily can accommodate anisotropic behavior. In particular, Mai and Walton [28] introduced a family of strain-limiting anisotropic models constructed within the class of models (1.25) taking the form:

$$\boldsymbol{E} = \phi(\mathbb{K}[\bar{\boldsymbol{S}}])\mathbb{K}[\bar{\boldsymbol{S}}] \tag{1.29}$$

with $\mathbb{K}[\cdot]$ denoting the fourth-order, linearized compliance tensor inverse to the linearized elasticity tensor $\mathbb{E}[\cdot]$. Both $\mathbb{K}[\cdot]$ and $\mathbb{E}[\cdot]$ are constructed to be positive definite, self-adjoint operators on Sym, and they satisfy

$$\mathbb{K}[\mathbb{E}[\boldsymbol{\epsilon}]] = \boldsymbol{\epsilon}, \quad \mathbb{E}[\mathbb{K}[\boldsymbol{\sigma}]] = \boldsymbol{\sigma}. \tag{1.30}$$

Two important special cases studied in the simulations presented below are isotropy and transverse isotropy. For isotropic material,

$$\mathbb{E}[\boldsymbol{\epsilon}] := 2\mu\boldsymbol{\epsilon} + \lambda(\boldsymbol{\epsilon}\cdot\boldsymbol{I})\boldsymbol{I} = 2\mu\left(\boldsymbol{\epsilon} + \frac{\nu}{1-2\nu}(\boldsymbol{\epsilon}\cdot\boldsymbol{I})\boldsymbol{I}\right) \tag{1.31}$$

with μ and λ denoting the customary Lamé parameters and ν denoting Poisson's ratio. In (1.31), $(\boldsymbol{\epsilon}\cdot\boldsymbol{I})$ is the trace-inner-product and $\boldsymbol{I}$ denotes the second-order identity tensor. For transversely isotropic material,

$$\mathbb{E}[\boldsymbol{\epsilon}] := 2\mu\boldsymbol{\epsilon} + \lambda(\boldsymbol{\epsilon}\cdot\boldsymbol{I})\boldsymbol{I} + \gamma(\boldsymbol{\epsilon}\cdot\boldsymbol{M})\boldsymbol{M} \tag{1.32}$$

with $\boldsymbol{M} = \boldsymbol{m} \otimes \boldsymbol{m}$ being the norm-one, rank-one, structural tensor with the unit-vector $\boldsymbol{m}$ defining the axis of symmetry. It is useful to note that (3.9) and (3.10) have the following direct, representations as fourth-order tensors:

$$\mathbb{E} = 2\mu \left(\mathbb{I} + \frac{\nu}{1-2\nu} \boldsymbol{I} \otimes \boldsymbol{I} \right) \tag{1.33}$$

$$\mathbb{E} = 2\mu \left(\mathbb{I} + \frac{\nu}{1-2\nu} \boldsymbol{I} \otimes \boldsymbol{I} + \bar{\gamma} \boldsymbol{M} \otimes \boldsymbol{M} \right) \tag{1.34}$$

in which $\mathbb{I}$ denotes the fourth-order identity tensor, $\bar{\gamma} := \frac{\gamma}{2\mu}$ and in (1.34), ν is the Poisson's ratio corresponding to pure tension in the direction of the axis of symmetry $\boldsymbol{m}$.

In the subsequent numerical study, we utilize a sub-class of (1.29) in which

$$\phi(\mathbb{K}[\bar{\boldsymbol{S}}]) = \tilde{\phi}(|\mathbb{K}^{1/2}[\bar{\boldsymbol{S}}]|) \tag{1.35}$$

in which $\tilde{\phi}(r)$ is a positive, monotone increasing function for which $r\tilde{\phi}(r)$ is uniformly bounded for $0 < r < \infty$, and $\mathbb{K}^{1/2}[\cdot]$ denotes the unique, positive-definite square-root of the compliance tensor $\mathbb{K}[\cdot]$ viewed as a linear transformation on Sym. For illustrative purposes in the finite element implementation, we consider the special case of (1.35) in which

$$\tilde{\phi}(r) := \frac{1}{(1 + (\beta r)^{\alpha})^{1/\alpha}}. \tag{1.36}$$

Substitution of (1.36) in (1.35) gives the uniform bound

$$\begin{aligned} |\boldsymbol{E}| &= \tilde{\phi}(|\mathbb{K}^{1/2}[\bar{\boldsymbol{S}}]|)|\mathbb{K}[\bar{\boldsymbol{S}}]| \\ &\leq \frac{1}{\beta}\frac{|\mathbb{K}[\bar{\boldsymbol{S}}]|}{|\mathbb{K}^{1/2}[\bar{\boldsymbol{S}}]|} \\ &= \frac{1}{\beta}\sqrt{\frac{\bar{\boldsymbol{S}}\cdot\mathbb{K}^2[\bar{\boldsymbol{S}}]}{\bar{\boldsymbol{S}}\cdot\mathbb{K}[\bar{\boldsymbol{S}}]}} \\ &\leq \frac{1}{\beta}\sqrt{\xi_m}, \quad \text{for all} \quad \bar{\boldsymbol{S}} \in \text{Sym} \end{aligned} \tag{1.37}$$

where ξ_m denotes the maximum eigenvalue of $\mathbb{K}[\cdot]$ viewed as a linear transformation on Sym.

Remark 2: The model (1.25), (1.35) is readily seen to have an associated complementary energy function. Indeed, we first observe that

$$\partial_{\boldsymbol{S}}|\mathbb{K}^{1/2}[\boldsymbol{S}]| = \partial_{\boldsymbol{S}}\sqrt{\boldsymbol{S}\cdot\mathbb{K}[\boldsymbol{S}]} = \frac{\mathbb{K}[\boldsymbol{S}]}{|\mathbb{K}^{1/2}[\boldsymbol{S}]|}. \tag{1.38}$$

It follows that

$$\partial_{\boldsymbol{S}}\hat{w}(|\mathbb{K}^{1/2}[\boldsymbol{S}]|) = \frac{\hat{w}'(|\mathbb{K}^{1/2}[\boldsymbol{S}]|}{|\mathbb{K}^{1/2}[\boldsymbol{S}]|}\mathbb{K}[\boldsymbol{S}]$$

and hence that $\hat{w}(|\mathbb{K}^{1/2}[\boldsymbol{S}]|)$ is a complementary energy function for the model (1.25), (1.35) provided

$$\hat{w}'(r) = r\tilde{\phi}(r) \tag{1.39}$$

or equivalently

$$w(r) = \int r\tilde{\phi}(r)rdr.$$

Remark 3: To investigate the invertibility of the model (1.25), (1.35), we first apply

the operator $\mathbb{E}^{1/2}[\cdot]$ to the constitutive relation obtaining

$$\mathbb{E}^{1/2}[\boldsymbol{E}] = \tilde{\phi}(|\mathbb{K}^{1/2}[\boldsymbol{S}]|)\mathbb{K}^{1/2}[\bar{\boldsymbol{S}}]. \tag{1.40}$$

Taking the norm of both sides of (1.40) gives

$$|\mathbb{E}^{1/2}[\boldsymbol{E}]| = \tilde{\phi}(|\mathbb{K}^{1/2}[\boldsymbol{S}]|)|\mathbb{K}^{1/2}[\bar{\boldsymbol{S}}]| = \psi(|\mathbb{K}^{1/2}[\boldsymbol{S}]|) \tag{1.41}$$

where $\psi(r) := r\,\tilde{\phi}(r)$. Therefore, if $\psi(r)$ is monotone, and hence invertible with inverse $\psi^{-1}(r)$, one has

$$|\mathbb{K}^{1/2}[\boldsymbol{S}]| = \psi^{-1}(|\mathbb{E}^{1/2}[\boldsymbol{E}]|)$$

and hence that the constitutive relation can be inverted to give

$$\bar{\boldsymbol{S}} = \xi(|\mathbb{E}^{1/2}[\boldsymbol{E}]|)\mathbb{E}[\boldsymbol{E}] \tag{1.42}$$

with

$$\xi(r) := \frac{1}{\tilde{\phi}\,(\psi^{-1}(r))}.$$

Remark 4: It is natural to ask why we chose the model (1.29), (1.35) rather than the apparently simpler model

$$\phi(\mathbb{K}[\bar{\boldsymbol{S}}]) = \tilde{\phi}(|\mathbb{K}[\bar{\boldsymbol{S}}]|). \tag{1.43}$$

The reason is that the model (1.29), (1.43) is not hyperelastic for any non-constant function $\tilde{\phi}(r)$. To see this, as noted above, it suffices to show that the Fréchet derivative $\mathrm{D}_{\boldsymbol{S}}\mathcal{F}(\boldsymbol{S})[\cdot]$ is not a self-adjoint fourth-order tensor. To that end, one merely needs to

observe that

$$\mathrm{D}_{\boldsymbol{S}}|\mathbb{K}[\boldsymbol{S}]|[\boldsymbol{H}_s] = \frac{\mathbb{K}[\boldsymbol{S}]\cdot\mathbb{K}[\boldsymbol{H}_s]}{|\mathbb{K}[\boldsymbol{S}]|} \tag{1.44}$$

where $\boldsymbol{H}_s$ is an arbitrary symmetric second-order tensor. It then follows from (1.29), (1.35) and (1.44) that

$$\mathrm{D}_{\boldsymbol{S}}\mathcal{F}(\boldsymbol{S}) = \tilde{\phi}(|\mathbb{K}[\boldsymbol{S}]|)\mathbb{K} + \frac{\tilde{\phi}'(|\mathbb{K}[\boldsymbol{S}]|)}{|\mathbb{K}[\bar{\boldsymbol{S}}]|}\mathbb{K}[\boldsymbol{S}]\otimes\mathbb{K}^2[\boldsymbol{S}]. \tag{1.45}$$

Since $\mathbb{K}[\boldsymbol{S}]\otimes\mathbb{K}^2[\boldsymbol{S}] \neq \mathbb{K}^2[\boldsymbol{S}]\otimes\mathbb{K}[\boldsymbol{S}]$, it is clear that the fourth-order tensor (1.45) is self-adjoint as an operator on Sym if and only if $\tilde{\phi}'(r) = 0$ for all $0 \leq r$.

Remark 5: From the above comments, it is evident that the model (1.29), (1.35), (1.36) is both invertible and hyperelastic. In particular, the complementary energy has the form $\hat{w}(|\mathbb{K}[\boldsymbol{S}]|)$ with

$$\hat{w}(r) = \int \frac{r\,dr}{(1+(\beta r)^\alpha)^{1/\alpha}} \tag{1.46}$$

from which it is evident that the complementary energy grows linearly with $|\bar{\boldsymbol{S}}|$, that is,

$$\hat{w}(|\mathbb{K}[\boldsymbol{S}]|) = O(|\bar{\boldsymbol{S}}|) \quad \text{as} \quad |\bar{\boldsymbol{S}}| \to \infty. \tag{1.47}$$

Also, substitution of (1.36) into (1.42) gives the equivalent hyperelastic formulation of (1.29), (1.35), (1.36):

$$\bar{\boldsymbol{S}} = \frac{\mathbb{E}[\boldsymbol{E}]}{(1-(\beta|\mathbb{E}^{1/2}[\boldsymbol{E}]|)^\alpha)^{1/\alpha}}, \tag{1.48}$$

with associated strain energy function $\check{w}(|\mathbb{E}^{1/2}[\boldsymbol{E}|)$

$$\check{w}(r) := \int \frac{r\,dr}{(1-(\beta r)^\alpha)^{1/\alpha}}. \tag{1.49}$$

Thus, from (1.47), (1.48) and (1.49), it is clear that both the stress and the strain energy can become unbounded even though the strain remains bounded. However, asymptotic arguments were given in [41] and [23] for a special class of strain-limiting models that at a mode III or mode I crack tip, neither the stress nor the strain become singular. The direct numerical simulations given in the next chapters for the more general class of models considered here, are fully consistent with these asymptotic results.

Remark 6:

Another important motivation behind the construction of the model (1.29), (1.35), (1.36) is that as $\beta \to 0$, the model converges to the linear stress-strain relation

$$\boldsymbol{E} = \mathbb{K}[\bar{\boldsymbol{S}}]. \tag{1.50}$$

It is important to recognize that (1.50) is not linearized elasticity since it involves the nonlinear Green-St. Venant strain tensor $\boldsymbol{E}$. The linearized theory of elasticity arises from (1.50) when $\boldsymbol{E}$ is infinitesimally small. Thus, one might define the infinitesimal strain regime by this requirement in which case (1.50) reduces to the linearized elastic model

$$\boldsymbol{\epsilon} = \mathbb{K}[\boldsymbol{\sigma}] \tag{1.51}$$

where $\boldsymbol{\epsilon}$ is the linearized strain tensor and $\boldsymbol{\sigma}$ is "the" stress tensor since there is no longer a distinction between the Cauchy and Piola-Kirchhoff stress tensors. However, another approach to defining the infinitesimal strain regime for (1.29), (1.35), (1.36) is to require that $\beta \gg 1$. This gives rise to a nonlinear relation between the stress $\bar{\boldsymbol{S}}$ and the strain $\boldsymbol{E}$ that, by constitutive restriction, must be infinitesimal and hence satisfy $\boldsymbol{E} \approx \boldsymbol{\epsilon}$. This latter notion of infinitesimal regime has the advantage over (1.51)

in that the infinitesimal strain assumption can never be violated even if the stress becomes unbounded in contrast to the linearized theory of elasticity (1.51) for which the infinitesimal strain assumption is violated for boundary value problems in which there are strain concentrating features such as crack tips, re-entrant corners, etc. For this reason, we adopt this latter notion of infinitesimal strain model that takes the form

$$\boldsymbol{\epsilon} = \tilde{\phi}(|\mathbb{K}^{1/2}[\boldsymbol{S}]|)\mathbb{K}[\boldsymbol{S}] \tag{1.52}$$

in which $\boldsymbol{S}$ can be viewed unambiguously as "the" stress due to the infinitesimal strain assumption.

1.3 Introduction to Brittle Fracture Modeling with Surface-Tension Excess Property

The second part of this dissertation is devoted to the numerical implementation of the brittle fracture model developed by Sendova and Walton [47]. A main goal is to reformulate the crack-face boundary condition that contains higher-order tangential derivatives and then implement the model using a stable numerical method (such as finite elements). The simplest fracture boundary value problem to study within the context of the theory of developed by Sendova and Walton (in [47]) is the case of anti-plane shear or mode III fracture. For the scope of this dissertation, we consider only the two-dimensional case, but the model can be easily extended to three dimensions. Also, the problem studied is quasi-static and we assume no crack-growth due to loading. Our main aim is to study the deformation of the crack under loading and also to understand the stress-strain concentration in the crack-tip neighborhood.

Oh, Walton and Slattery [31] developed a new fracture theory based on the earlier work of Slattery et al. [49] and the theory they presented in [31] is based upon an extension of continuum mechanics to the nanoscale[2]. In [31] they assumed an existence of a

[2]The word *nanoscale* in [31] is used to the neighborhood (within 10 nm) of a material interface

two-dimensional *dividing surface* (similar to *Gibbs* isotherm) lying along the material interface between bulk intact material and air or vaccum. This surface can account for atomistic effects through an ascribed surface excess properties such as internal energy, free energy, stress, mass, etc. They studied the classical Griffith problem of a mode-I crack in an infinite linear elastic body under tensile stress and by assigning surface tension as an excess property of the dividing surface. They have also included a bulk correction term for the intermolecular forces near the interface. Because of the highly nonlinear nature of the problem, they seek a singular perturbation solution using a perturbation parameter. They showed that the fracture tip is sharp contrary to the blunt crack-tip of the LEFM model and another important result was that stress at the crack-tip was finite. A significant advantage of the fracture modeling approach of Oh, Walton and Slattery [31] is that it doesn't require any adjustable parameter for bridging domains (such as near and far from the fracture-tip). Further, this theory is based on the classical continuum approach to modeling the material behavior and takes into account of forces in the vicinity of the fracture surfaces.

Then, Sendova and Walton [47] developed a more detailed brittle fracture model with surface tension (cases of both constant and curvature dependent) as excess property of the dividing surface. They consider the case of straight mode-I crack of finite length in an infinite linear elastic body subjected to uniform tensile loading. To derive the governing equations, Sendova and Walton considered an arbitrary part of the body intersecting the dividing surface (which coincides with the crack-surface Σ_κ in the reference configuration). The parameterized crack-surface (both upper and lower crack-surfaces) in the reference configuration is given by

$$\Sigma_\kappa^{\pm} = \left\{ \boldsymbol{X} : |X_1| \leq 1,\ X_2 = 0^{\pm} \right\}, \tag{1.53}$$

where $\boldsymbol{X}$ is a point in the reference configuration and $(\cdot)^{\pm}$ denotes upper and lower crack-surfaces. Then the corresponding, parameterized, upper-lower crack surface in the current configuration is given by

$$\Sigma^{\pm} = \left\{ \boldsymbol{x} : x_1 = X_1 + u_1(X_1, 0^{\pm}),\ x_2 = u_2(X_1, 0^{\pm}),\ |X_1| \leq 1 \right\}, \tag{1.54}$$

where $\boldsymbol{x} = (x_1,\, x_2)$ is the arbitrary point in the current configuration and $(u_1,\, u_2)$ is the corresponding displacement vector. Then Sendova and Walton [47] balances the forces acting on the arbitrary part containing the crack-tip and obtained two balance equations, namely a differential momentum balance equation for bulk body and a jump momentum balance equation across both upper and lower crack surfaces. The equation of differential momentum balance equation derived in [47] is same as the one derived from classical linear elastic fracture mechanics model i.e.

$$\mathrm{Div}\, \mathbf{T}_{\kappa} + \mathbf{b}_{\kappa} = \mathbf{0} \quad \text{in} \quad \Omega\,, \tag{1.55}$$

inwhich $\mathbf{T}_{\kappa}$ is the first Piola-Kirchhoff stress and $\mathbf{b}_{\kappa}$ is the mutual body force term. Further in [47] they have considered a surface tension as an excess property to the dividing surface, which yields a new expression for the jump momentum balance (JMB) along the crack surface, given by

$$J \left(\mathrm{div}_{\sigma}\, \mathbf{T}^{(\sigma)} \otimes \mathbf{n}^{\pm} \right)_m \mathbf{F}^{-T} \mathbf{N}^{\pm} + [\![\mathbf{T}_{\kappa}]\!] \mathbf{N}^{\pm} = \mathbf{0}. \tag{1.56}$$

Where the symbol $\mathbf{F}$ is the deformation gradient, $J = \det\mathbf{F}$, div_{σ} indicates the surface-divergence, $\mathbf{N}^{-}[\mathbf{N}^{+}]$ and $\mathbf{n}^{-}[\mathbf{n}^{+}]$ are outward unit normals to the upper[lower] crack profile in the reference and current configuration, respectively. The subscript $(\cdot)_m$ refers to the quantities in material description. The double bracket term $[\![\cdot]\!]$ indicates

the jump across the fracture surface from the bulk material phase of the body to the phase bounded by the opened fracture surface. In [49], the authors showed the surface Cauchy stress tensor, $\mathbf{T}^{(\sigma)}$ is modeled as Eulerian and may be written as a constant multiple (which is an excess property, i.e. surface tension) of a projection tensor onto the tangent space to the crack-surface in the current configuration (Σ), i.e.

$$\mathbf{T}^{\sigma} = \tilde{\gamma}\mathbf{P}, \tag{1.57}$$

in which $\tilde{\gamma}$ is surface tension and it is a function of tangential component. Then the jump momentum balance in Cartesian component form[3] is

$$\begin{aligned}\sigma_{12} =& -\frac{(1+u_{1,1})^2 + u_{1,2}u_{2,1}}{\sqrt{(1+u_{1,1})^2 + u_{2,1}^2}}\left(\frac{\tilde{\gamma}'(X_1)(1+u_{1,1})^2}{(1+u_{1,1})^2 + u_{2,1}^2}\right.\\ &\left. + \frac{\tilde{\gamma}'(X_1)\left[u_{2,1}^2 u_{1,12} + u_{2,1}(1+u_{1,1})(u_{1,11}-u_{2,12}) - (1+u_{1,1})^2 u_{2,11}\right]}{\left((1+u_{1,1})^2 + u_{2,1}^2\right)^2}\right),\end{aligned} \tag{1.58}$$

$$\begin{aligned}\sigma_{22} =& -\sqrt{(1+u_{1,1})^2 + u_{2,1}^2}\left(\frac{\tilde{\gamma}'(X_1)(1+u_{1,1})u_{2,1}}{(1+u_{1,1})^2 + u_{2,1}^2}\right.\\ &\left. - \frac{\tilde{\gamma}(X_1)(1+u_{1,1})\left[u_{2,1}^2 u_{1,12} + u_{2,1}(1+u_{1,1})(u_{1,11}-u_{2,12}) - (1+u_{1,1})^2 u_{2,11}\right]}{\left((1+u_{1,1})^2 + u_{2,1}^2\right)^2}\right),\end{aligned} \tag{1.59}$$

where $X \in \Sigma^+$ and a similar expression holds for Σ^- and also $u_{i,j} = \frac{\partial u_i}{\partial x_j}$. Further in [47], Sendova and Walton assumed that the linear elastic constitutive behavior to model the response of the bulk material in the reference configuration, hence Hooke's law can be used to model the response of the material. Further they [47] have considered two cases for the surface tension, either a constant or an expression that depends

[3]For a detailed derivation of the JMB please refer the Appendix A in [47]

linearly on the curvature of the fracture surface and no mutual body force correction term ($\mathbf{b}_\kappa = 0$ in (1.55)). They analyze the fracture boundary value problem appealing to Dirichlet-to-Neumann and Neumann-to-Dirichlet maps and derived a singular integrodifferential equation for the upper, crack-face, opening displacement on the compact interval $|X_1| < 1$. Then the singular integrodifferntial equation was analyzed through regularization to a second-kind Fredholm integral equation. For the model using curvature-dependent surface tension, Sendova and Walton [47] prove that crack-tip stresses are bounded and crack-surfaces (both upper and lower) closes with a sharp crack-tip.

In [19], for the first time, Ferguson proposed a finite element based numerical implementation of the brittle fracture model developed by Sendova and Walton [47]. For the classical Griffith crack problem in the case of constant surface tension, the numerical results presented in [19] agrees very well with the theoretical results of [47]. Further, Walton [53] studied the case of mixed-mode fracture BVP and gave a modification to curvature-dependent surface tension model. For the mixed-mode (combination of both mode-I and mode-II[4]) type of loading the only symmetry that exists is that the displacement vector field is symmetric through origin. Hence deriving a singular integrodifferential system was not straight forward. It was shown that, when the surface tension is assumed to be constant on the crack-surface, the classical square-root crack-tip stress singularity is replaced by a weak (logarithmic) singularity. But a modified model in which the surface tension is assumed to depend upon odd-order tangential derivatives of the tangential displacement component and even-order tangential derivatives of the normal displacement component as

[4]In Mode-II fracture the *shear* stresses acting parallel to the plane of the crack and perpendicular to the crack front.

$$\tilde{\gamma} = \gamma_0 + \gamma_1\, u_{1,1}(X_1, 0) + +\gamma_2\, u_{1,111}(X_1, 0) + \gamma_3\, u_{2,11}(X_1, 0), \tag{1.60}$$

yields bounded crack-tip stress. In the above surface-tension model (1.60), the constants γ_0, γ_1, γ_2 and γ_3 denotes dimensionless surface-tension parameters.

Remark 6: It should be noted that the fracture modeling approach, studied in [47, 53], by ascribing the excess property (such as surface tension, surface energy etc) is different from the Barenbalt-type cohesive zone model. The latter theory introduces an entirely new cohesive surface in the bulk material near the fracture edge and has adjustable parameters (such as traction and width of the cohesive zone) in the constitutive law. More importantly, cohesive zone approach has several disadvantages such as the parameters involved may not have a clear physical meaning and are difficult to validate experimentally. Although the cohesive zone model has been studied extensively the physical existence of the cohesive zone is still an issue of debate. But the former approach uses the conventional continuum mechanics ideas and assumes the existence of surface Cauchy stress tenor and models it as a projection into the surface tangent plane. One of the most significant features of the surface-mechanics model [47] is that it doesn't introduces any artificial surface near the *physical* crack-tip and avoids adjustable ad hoc choices of parameters that are present in most other models (including cohesive and process zone models).

However, FEM based numerical implementation of Sendova and Walton [47] modeling approach is challenging due to fact that the JMB has higher order tangential derivatives. One would require higher order smoothness for the test functions on the crack-surface compared to rest of the domain. In the second part of this dissertation, we study a reformulation of the fracture boundary conditions to remove the higher-order derivatives in the case of mode-III fracture. The resultant boundary condition

along with the bulk-material response relation is solved using two different approaches. Both methods agree very well and the numerical predictions are consistent with the theoretical predictions presented in [47].

The rest of this dissertation is organized as follows: In Chapter 2, we formulate and study the asymptotic behavior the solution fracture BVP for a single plane-strain crack using strain-limiting theory of elasticity. We present an asymptotic and numerical optimization technique to study the solution behavior near the mode-I crack-tip. Further in Chapter 3 we study a finite elements based numerical implementation of a single, static, pure mode-I crack in a class of nonlinear strain-limiting anisotropic elastic body. We derive a linearized version of the strong form using Damped Newton's method and obtain the solution to the weak-form using Finite Element Method (FEM). In Chapter 4, we have outlined an approach for implementing a brittle fracture theory with surface tension excess property. We give an elaborate procedure of the reformulation of the crack-surface boundary condition as an Fredholm second kind integral equation for the Neumann data. We present the results of the finite elements based numerical implementation, in particular, we will show that the numerical results agree very well with the theoretical results of [47]. Finally, in Chapter 5 we give a detailed explanation on the results obtained in this dissertation and also some ideas for future research. We are particularly interested in developing computational models for the curvature-dependent class of surface-mechanics based brittle fracture theory and also to study dynamic fracture problems in the context of both theories presented in this dissertation.

2. MODELING A SINGLE PLANE-STRAIN QUASI-STATIC CRACK WITHIN THE CONTEXT OF A NONLINEAR STRAIN-LIMITING THEORY OF ELASTICITY*

In this chapter, we study a crack-tip asymptotic analysis of the solution to nonlinear crack-boundary value problem. The nonlinear response relation studied in this chapter, is derived within the context of the general implicit theory of elasticity. We demonstrate, using a combination of asymptotic and numerical procedure, the state of crack-tip stress-strain in a static, isotropic, nonlinear elastic body. Our main aim is to layout an approach for modeling brittle fracture using strain-limiting theory of elasticity.

2.1 The Material Model

The problem studied in this chapter is a straight, mode-I crack in an infinite, isotropic, elastic body subjected to plane-strain loading. The crack is assumed to be lying along $X_2 = 0$. The response of the body is modeled using a special class of strain-limiting constitutive relation. The issue here is to understand the asymptotic behavior of the solution to the nonlinear fracture BVP in a neighborhood of the crack-tip. In contrast to the classical linearized models, the nonlinear response relations introduced by Rajagopal [34] and Mai and Walton [28], limit the crack-tip strains to a physically realistic level. Hence, these strain-limiting models of elasticity offers an intriguing framework to study brittle fracture.

For the problem on hand, with the aim toward understanding the crack-tip asymp-

*Part of this chapter is reprinted with permission from Elsevier Publications, "Modeling fracture in the context of a strain-limiting theory of elasticity: A single plane-strain shear crack" by Kun Gou, M. Mallikarjuna, K. R. Rajagopal, Jay R. Walton, *International Journal of Engineering Science*, Special Issue on "Qualitative Methods in Engineering Science", 88, 73-82, 2015; Copyright 2015 Elsevier.

totics, we consider a special form of nonlinear elastic response relation as:

$$\boldsymbol{\epsilon} = \hat{\boldsymbol{\epsilon}}\left(\mathbf{T}\right) := \phi\left(|\mathbb{K}[\mathbf{T}]|\right)\mathbb{K}^2[\mathbf{T}] \tag{2.1}$$

and where $\phi(\cdot)$ is a monotone decreasing function satisfying

$$\lim_{r\to\infty} r\phi(r) = M < \infty. \tag{2.2}$$

In the strain-limiting model (2.1), the stresses have been non-dimensionalized by the reference shear modulus. Also, in (2.1), the symbol $\mathbb{K}[\cdot]$ denotes a general linearized elastic compliance tensor and $|\cdot|$ denotes the Frobenius norm as:

$$|\mathbb{K}[\mathbf{T}]|^2 := \mathbb{K}[\mathbf{T}]\colon \mathbb{K}[\mathbf{T}] = \mathbf{T}\colon \mathbb{K}^2[\mathbf{T}], \tag{2.3}$$

where the colon-operator ($:$) denotes the trace inner product between second order tensors and also the symbol $\mathbf{T}$ denotes the Cauchy stress tensor. To invert the above strain-limited constitutive relation (2.1), define a 4^{th} order positive-definite, elasticity tensor $\mathbb{E}$ as the inverse of the compliance tensor, i.e.

$$\mathbb{E}[\cdot] = \mathbb{K}^{-1}[\cdot]. \tag{2.4}$$

Both $\mathbb{K}[\cdot]$ and $\mathbb{E}[\cdot]$ are constructed to be positive definite, self-adjoint operators and they satisfy

$$\mathbb{K}[\mathbb{E}[\boldsymbol{\epsilon}]] = \boldsymbol{\epsilon}, \qquad \mathbb{E}[\mathbb{K}[\mathbf{T}]] = \mathbf{T}\,. \tag{2.5}$$

Taking the action of $\mathbb{E}$ on (2.1) yields

$$\mathbb{E}[\boldsymbol{\epsilon}] = \phi\left(|\mathbb{K}[\mathbf{T}]|\right)\mathbb{K}[\mathbf{T}]. \tag{2.6}$$

Then taking the norm of both sides of the equation (2.6) gives

$$|\mathbb{E}[\boldsymbol{\epsilon}]| = \phi\left(|\mathbb{K}[\mathbf{T}]|\right)|\mathbb{K}[\mathbf{T}]|. \tag{2.7}$$

Then define

$$\psi\left(|\mathbb{K}[\mathbf{T}]|\right) = \phi\left(|\mathbb{K}[\mathbf{T}]|\right)|\mathbb{K}[\mathbf{T}]|, \tag{2.8}$$

and taking the inversion of the equation (2.8) gives

$$|\mathbb{K}[\mathbf{T}]| = \psi^{-1}\left(|\mathbb{E}[\boldsymbol{\epsilon}]|\right). \tag{2.9}$$

Finally we write the inverted constitutive relation for stress in-terms of strain as:

$$\mathbf{T} = \frac{\mathbb{E}[\boldsymbol{\epsilon}]}{\phi\left(\psi^{-1}\left(\mathbb{E}[\boldsymbol{\epsilon}]\right)\right)} \quad . \tag{2.10}$$

For the special form of $\phi(\cdot)$

$$\phi(r) = \frac{1}{1+\beta r} \tag{2.11}$$

considered, the above inverted stress-strain relation (2.10) reduces to

$$\mathbf{T} = \frac{\mathbb{E}[\boldsymbol{\epsilon}]}{1-\beta\,|\mathbb{E}[\boldsymbol{\epsilon}]|} \quad , \tag{2.12}$$

where β is a modeling parameter and $\frac{1}{\beta}$ is the limiting-strain norm.

It should be clear that in general for the implicit nonlinear response relations it is not possible to express either second Piola-Kirchhoff stress tensor in terms of Green-St. Venant tensor $\boldsymbol{E}$ or the Cauchy stress tensor $\mathbf{T}$ in terms of left Cauchy-Green tensor $\boldsymbol{B}$. But note that a special form of the strain-limiting model (2.11) considered here is globally invertible and hence we can construct the inverted constitute relation

(2.12). But the inverted form (2.12) is not utilized to derive the main analytical result about the crack-tip asymptotic stress and strain behavior. The inversion procedure is included here for the special sub-class of more general class of Rajagopal's *Implicit Theory of Elasticity* [34].

2.2 Plane-Strain Mode-I Fracture Problem

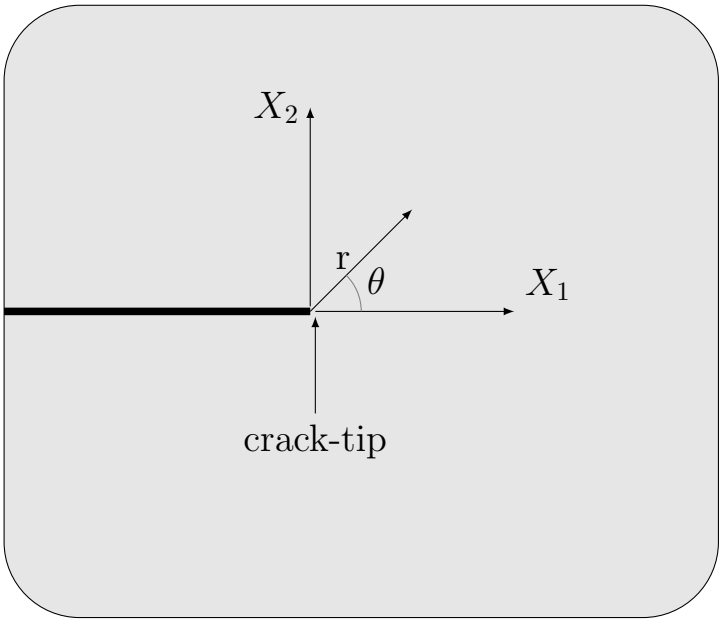

Figure 2.1: Infinite elastic slab containing a semi-infinite crack.

Consider a semi-infinite, quasi-static, Griffith crack in an infinite planar as depicted in Figure 2.1. The figure also illustrates the cartesian coordinates X_1, X_2 and the polar coordinates r, θ, lies in the $X_1 - X_2$ plane, are centered at the crack-tip. A main issue here is to study the asymptotic behavior of the solution to the nonlinear fracture boundary value problem in a neighborhood of the crack-tip. The use of strain-limited response relations to study fracture readily prevents the crack-tip strain singularity,

but it leaves open to investigate whether or not crack-tip stress becomes unbounded within the asymptotic expansions considered for the primary variable.

The vector $\boldsymbol{x} = (x_1, x_2)$ denotes a point in the current configuration of the body. As usual $\boldsymbol{u}(x_1, x_2)$ denotes the displacement of the material point $\boldsymbol{X} = (X_1, X_2)$. Further, the stress-strain response relation formulated in this work is valid under the assumption of infinitesimal strain, i.e. the displacement gradient is assumed to be *very small*[2]. Therefore there is no distinction between the reference and current configurations. Hence we can interchange the symbols $\boldsymbol{x}$ and $\boldsymbol{X}$.

In this part of the dissertation, we study a strain-limiting nonlinear fracture BVP through a formal, crack-tip, asymptotic analysis and then in the subsequent chapter we develop a finite element numerical model. Also we would like to emphasize a point on the finite element numerical results of the model, that the numerical simulations can never fully resolve the asymptotic behavior of the crack-tip stress field, but it can be used to gain an useful insight into the stress behavior predicted by the reference linearized elasticity model. The strain-limiting model admit a logically consistent linearization yielding a nonlinear relationship between stress and linearized strain, such nonlinear relationship can't be obtained by the linearization procedure of the classical model. Further, the sequence of finer computational meshes near the crack-tip neighborhood will only lend the support to rigorous asymptotic analysis, but won't fully resolve the crack-tip stress behavior.

In this chapter, we study the asymptotic behavior of the crack-tip stress, analytically, using a special form of strain-limited bulk nonlinear constitutive relation (2.1).

[2]For a detailed discussion on how small does the displacement gradient have to be for the linearized theory to apply, please refer [39].

To that end, we introduce the Airy stress potential $\Phi(x, y)$ which satisfies

$$\operatorname{div}(\operatorname{adj}(\mathrm{D}^2\Phi)) = 0, \tag{2.13}$$

where $\operatorname{div}(\cdot)$ is the usual divergence operator, $\operatorname{adj}(\cdot)$ denotes the adjugate[3] matrix and the symbol $\mathrm{D}^2(\cdot)$ is the Hessian operator. Conveniently, we can then define

$$\mathbf{T} := \operatorname{adj}(\mathrm{D}^2\Phi) \tag{2.14}$$

this guaranties the satisfaction of the equilibrium equation (without the body force term)

$$\operatorname{div}(\mathbf{T}) = 0. \tag{2.15}$$

Then the above constitutive relation (2.1) can be rewritten as follows

$$\begin{aligned} \hat{\boldsymbol{\epsilon}}(\mathbf{T}) &= \phi\left(|\mathbb{K}[\mathbf{T}]|\right)\mathbb{K}^2[\mathbf{T}] \\ &= \phi\left(|\mathbb{K}[\operatorname{adj}(\mathrm{D}^2\Phi)]|\right)\mathbb{K}^2[\operatorname{adj}(\mathrm{D}^2\Phi)] \\ &= \phi\left(|\mathbb{K}[\mathrm{D}^2\Phi]|\right)\mathbb{K}^2[\mathrm{D}^2\Phi]. \end{aligned} \tag{2.16}$$

In the above equations, we have used the well-known identities for a 2-dimensional, plane-strain problem. To study a question of whether or not the nonlinear fracture boundary value problem admits the classical crack-tip stress singularity, it is natural to perform the asymptotic analysis of the strain compatibility equation for the Airy stress potential Φ. To this end we consider the compatibility equation for the strain tensor in the form:

[3]The adjugate matrix of a square matrix is the transpose of its cofactor matrix.

$$0 = \operatorname{div}\operatorname{div}\left(\phi\left(|\mathbb{K}[\mathrm{D}^2\Phi]|\right)\mathbb{K}^2[\mathrm{D}^2\Phi]\right). \tag{2.17}$$

Expanding the above equation

$$0 = \operatorname{div}\operatorname{div}\left(\mathbb{K}(\mathbf{A})\right) + 2\frac{\nabla\phi(|\mathbf{A}|)}{\phi(|\mathbf{A}|)} \cdot \operatorname{div}\left(\mathbb{K}(\mathbf{A})\right) + \frac{\mathrm{D}^2\phi(|\mathbf{A}|)}{\phi(|\mathbf{A}|)} \cdot \mathbb{K}(\mathbf{A}) \tag{2.18}$$

where

$$\mathbf{A} := \mathbb{K}[\mathrm{D}^2\Phi]. \tag{2.19}$$

Symmetry and the Boundary Conditions:

For the plane-strain problem on hand, the horizontal displacements are symmetric and the vertical displacements are antisymmetric with respect to the vertical axis. i.e. if $\boldsymbol{u} = (u(x, y, z), v(x, y, z), w(x, y, z))$ is the displacement in the body, then

$$u(x, -y, z) = u(x, y, z), \quad v(x, -y, z) = -v(x, y, z), \tag{2.20}$$

and the usual plane-strain assumption yields $w = 0$. Therefore, the asymptotic analysis can be done over the upper-half plane.

The classical pure mode-I problem imposes zero traction on the crack-face (i.e. along $x_2 = 0^+$ and $|x_1| < 0$) with far-field tensile loading applied remotely to the body. Also the symmetry implies that the crack-opening displacement (i.e. $v(x, y)$) vanishes along the line ahead of the semi-infinite crack.

In order to simplify the calculations, we formulate the nonlinear fracture problem in a polar coordinate system (r, θ) centered at the crack-tip. Therefore, for the problem on hand, the boundary conditions are given by

$$\partial_\theta\Phi(r, 0+) = \partial_\theta^3\Phi(r, 0+) = \Phi(r, \pi-) = \partial_\theta^2\Phi(r, \pi-) = 0 \text{ for } r > 0. \tag{2.21}$$

The goal is to study the asymptotic behavior of solutions to (2.18), subjected to the boundary conditions (2.21), in the neighborhood of the crack-tip (i.e. $r \to 0^+$). To that end, it is helpful to recall the asymptotic analysis of the classical linear elastic case.

2.3 Linear Elastic Case

In the case of classical, linearized, elastic, plane strain fracture problem, the compatibility equation is given by

$$0 = \operatorname{div}\operatorname{div}\mathbf{A} = \frac{1}{\mu}\mathrm{C}_1 \triangle^2 \Phi \tag{2.22}$$

where

$$\mathrm{C}_1 := \frac{1}{4}\left(1 + \frac{\mu}{\kappa}\right), \tag{2.23}$$

μ is the reference shear modulus, κ is the bulk modulus and $\triangle^2$ denotes the classical bi-harmonic operator. The bi-harmonic equation admits solutions of the form

$$\Phi(r,\theta) = r^{\alpha}\,\hat{\Phi}(\theta). \tag{2.24}$$

Since the bi-harmonic operator seperates

$$\triangle^2 \Phi(r,\theta) = r^{\alpha-4}\,\mathcal{L}_b\left[\hat{\Phi}(\theta)\right] \tag{2.25}$$

where

$$\mathcal{L}_b\left[\hat{\Phi}(\theta)\right] := \hat{\Phi}''''(\theta) + \left(\alpha^2 + (\alpha-2)^2\right)\hat{\Phi}''(\theta) + \alpha^2(\alpha-2)^2\hat{\Phi}(\theta). \tag{2.26}$$

The goal is to find nontrivial solutions to the fourth-order ordinary differential equation

$$0 = \mathcal{L}_b \left[\hat{\Phi}(\theta) \right] \tag{2.27}$$

subject to the homogeneous boundary conditions

$$\hat{\Phi}(\pi) = \hat{\Phi}''(\pi) = \hat{\Phi}'(0) = \hat{\Phi}'''(0) = 0. \tag{2.28}$$

A convenient strategy for finding such solutions is to introduce the Fourier expansion

$$\hat{\Phi}(\theta) = \sum_{\mathrm{n}=0}^{\infty} a_n \cos(\gamma_n \theta) \tag{2.29}$$

which takes advantage of the obvious symmetries of $\hat{\Phi}(\theta)$. The expansion (2.29) satisfies the boundary conditions (2.28) provided

$$\gamma_n = \frac{1}{2} + n\pi, \qquad \text{for} \qquad n = 0, 1, \ldots. \tag{2.30}$$

Substitution of (2.29) into (2.27) gives

$$0 = \sum_{n=0}^{\infty} a_n M_n(\alpha) \cos(\gamma_n \theta) \tag{2.31}$$

where

$$M_n(\alpha) := \gamma_n^4 - \left(\alpha^2 + (\alpha - 2)^2 \right) \gamma_n^2 + \alpha^2 (\alpha - 2)^2. \tag{2.32}$$

Nontrivial solutions to (2.31) can be constructed by choosing

$$a_n = 0 \qquad \text{for} \qquad n = 2, 3 \ldots \tag{2.33}$$

and finding the values of α for which

$$M_n(\alpha) = 0 \qquad \text{for} \qquad n = 0, 1. \tag{2.34}$$

One sees immediately that α must satisfy

$$\gamma_0^2 + \gamma_1^2 = \alpha^2 + (\alpha - 2)^2. \tag{2.35}$$

The above equation (2.35) has two roots $\alpha = \frac{1}{2}$ and $\alpha = \frac{3}{2}$. But for $\alpha = \frac{1}{2}$ the displacement $u_r \to \infty$. Also since the stresses behave as $r^{\alpha-2}$ like $r \to 0+$, choosing $\alpha = \frac{3}{2}$ gives rise to the classical square-root singularity in stresses at the crack-tip.

Remark 1:

Restricting the domain of the operator $\mathcal{L}_b[\cdot]$ to functions satisfying the homogeneous boundary conditions (2.28), it follows from the above analysis that when $\alpha = \frac{3}{2}$, the null-space of $\mathcal{L}_b[\cdot]$ is a two-dimensional subspace spanned by $\cos(\gamma_0\theta)$ and $\cos(\gamma_1\theta)$.

2.4 Nonlinear Crack-Tip Asymptotic Analysis

The non-linear fracture model (2.18) along with the boundary conditions (2.21) does not admit elementary separation of variable solutions of the type (2.24). However, it does admit solutions in the form of an asymptotic series

$$\Phi(r, \theta) \sim \sum_{j,k=0}^{\infty} r^{\alpha j+k} \hat{\Phi}_{jk}(\theta), \quad \text{as} \quad r \to 0^+ , \tag{2.36}$$

where α is any positive real number and it's leading value defines the crack-tip singularity. Then the asymptotic behavior near the crack-tip of solutions to (2.18) can be

obtained from the observation that for functions of the form (2.36),

$$\operatorname{div}\operatorname{div}\left(\phi(|\mathbf{A}|)\mathbb{K}(\mathbf{A})\right) \quad \sim \quad r^{\alpha-4}\,\hat{\mathcal{L}}\left[\hat{\Phi}(\theta)\right] \quad \text{as} \quad r\to 0+ \tag{2.37}$$

where $\hat{\mathcal{L}}\,[\cdot]$ is a nonlinear, fourth-order differential operator. Before the construction of the explicit form of the operator, we first note that

$$\mathbf{A}(r,\theta) = r^{\alpha-2}\hat{\mathbf{A}}(\theta) \tag{2.38}$$

with

$$\begin{aligned}\mu\hat{\mathbf{A}}(\theta) := &\left(\frac{1}{4}\left(\frac{\mu}{\kappa}-1\right)\hat{\Phi}''(\theta)+\left(\frac{\alpha^2}{4}\left(\frac{\mu}{\kappa}-1\right)+\frac{\alpha(\alpha-1)}{2}\right)\hat{\Phi}(\theta)\right)\mathrm{j}_1(\theta)\otimes\mathrm{j}_1(\theta)\\ &+\left(\frac{1}{4}\left(\frac{\mu}{\kappa}+1\right)\hat{\Phi}''(\theta)+\left(\frac{\alpha^2}{4}\left(\frac{\mu}{\kappa}-1\right)+\frac{\alpha}{2}\right)\hat{\Phi}(\theta)\right)\mathrm{j}_2(\theta)\otimes\mathrm{j}_2(\theta)\\ &+\frac{\alpha-1}{2}\hat{\Phi}'(\theta)(\mathrm{j}_1(\theta)\otimes\mathrm{j}_2(\theta)+\mathrm{j}_2(\theta)\otimes\mathrm{j}_1(\theta))\,,\end{aligned} \tag{2.39}$$

where $\mathrm{j}_1(\theta)$, $\mathrm{j}_2(\theta)$ denote the standard orthonormal polar basis. In order to construct the explicit form of the operator $\hat{\mathbb{L}}\,[\cdot]$ in (2.37), we need to consider the cases for the value of α (i.e. $1<\alpha\leq 2$ and $\alpha>2$) separately. First, notice that for the choice of ϕ as in (2.11), one can easily show that

$$\phi(r^{\alpha-2}|\hat{\mathbf{A}}(\theta)|) \sim \begin{cases} 1 & \text{if} \quad \alpha>2 \\ \frac{r^{2-\alpha}}{\beta|\hat{\mathbf{A}}(\theta)|} & \text{if} \quad \alpha<2 \end{cases} \quad \text{as} \quad r\to 0+, \tag{2.40}$$

and also

$$\phi'(s) = -\beta\phi(s)^2 \tag{2.41}$$

$$\phi''(s) = 2\beta^2\phi(s)^3 \tag{2.42}$$

From (2.38), (2.39), (2.40) and (2.41), it is evident that for $\alpha > 2$, the asymptotic forms of the nonlinear operators in (2.18) as $r \to 0+$ are strictly greater powers of r than the linear operator in (2.18). Indeed, the asymptotic order of the nonlinear terms in (2.18) as $r \to 0+$ is $r^{2(\alpha-3)}$. Thus for $\alpha > 2$, the nonlinear operator (2.17) has the same asymptotic behavior as $r \to 0+$ as does the linear operator in (2.18). Hence for $\alpha > 2$, the only nontrivial asymptotic (as $r \to 0+$) null-spaces of the nonlinear operator (2.17) occur for $\alpha = 5/2, 7/2 \ldots$ in agreement with the linear theory. Also, $\alpha = 5/2$ corresponds to the cusp-shaped displacement profiles and bounded crack-tip stress distributions.

For $\alpha < 2$, all the three terms in (2.18) have asymptotic order $r^{\alpha-4}$ as $r \to 0+$. The asymptotic ordinary differential operator $\hat{\mathbb{L}}[\hat{\Phi}(\theta)]$ takes the form

$$\mu\hat{\mathcal{L}}[\hat{\Phi}(\theta)] = \hat{\mathcal{L}}_1[\hat{\Phi}(\theta)] + \hat{\mathcal{L}}_2[\hat{\Phi}(\theta)] + \hat{\mathcal{L}}_3[\hat{\Phi}(\theta)]. \tag{2.43}$$

Where $\hat{\mathcal{L}}_i[\cdot]$, $i = 1, 2, 3$ are defined as follows

$$\hat{\mathcal{L}}_1[\hat{\Phi}(\theta)] := \lim_{r\to 0+} r^{\alpha-4} \operatorname{div}\operatorname{div}(\mathbb{K}(\mathbf{A})) \tag{2.44}$$

$$\hat{\mathcal{L}}_1[\hat{\Phi}(\theta)] := \mathrm{C}_2 \left[\hat{\Phi}''''(\theta) + \left(\alpha^2 + (\alpha-2)^2\right)\hat{\Phi}''(\theta) + \alpha^2(\alpha-2)^2\hat{\Phi}(\theta)\right] \tag{2.45}$$

and C_2 is given by

$$\mathrm{C}_2 = \frac{1}{8\mu}\left(\frac{\mu^2}{\kappa^2} + 1\right) \tag{2.46}$$

$$\begin{aligned}\hat{\mathcal{L}}_2[\hat{\Phi}(\theta)] &:= \lim_{r\to 0+} r^{\alpha-4}\, 2\frac{\nabla\phi(|\mathbf{A}|)}{\phi(|\mathbf{A}|)} \cdot \operatorname{div}(\mathbb{K}(\mathbf{A})) \\ &= \frac{-2}{|\hat{\mathbf{A}}(\theta)|}\{H_1 \cdot F_1 + H_2 \cdot F_2\}. \end{aligned} \tag{2.47}$$

Where H_1, H_2, F_1, F_2 are defined as follows

$$H_1 := (\alpha - 2)|\hat{\mathbf{A}}(\theta)| \tag{2.48}$$

$$H_2 := \frac{\left(|\hat{\mathbf{A}}(\theta)|^2\right)'}{2|\hat{\mathbf{A}}(\theta)|} \tag{2.49}$$

$$\begin{aligned} F_1 := {} & \frac{\alpha - 2}{8\mu^2}\left(\frac{\mu^2}{\kappa^2} - 1\right)(\hat{\Phi}''(\theta) + \alpha^2\hat{\Phi}(\theta)) + \frac{\alpha(\alpha-1)(\alpha-2)}{4\mu^2}\hat{\Phi}(\theta) + \frac{(\alpha-1)}{4\mu^2}\hat{\Phi}''(\theta) \\ & + \left(\alpha(\alpha-2)\hat{\Phi}(\theta) - \hat{\Phi}''(\theta)\right) \end{aligned} \tag{2.50}$$

$$\begin{aligned} F_2 := {} & \frac{(\alpha-1)(\alpha-2)}{4\mu^2}\hat{\Phi}'(\theta) + \frac{1}{8\mu^2}\left(\frac{\mu^2}{\kappa^2} - 1\right)(\hat{\Phi}'''(\theta) + \alpha^2\hat{\Phi}'(\theta)) + \frac{1}{4\mu^2}(\hat{\Phi}'''(\theta) \\ & + \alpha\hat{\Phi}'(\theta)) + \frac{2(\alpha-1)}{4\mu^2}\hat{\Phi}'(\theta). \end{aligned} \tag{2.51}$$

From (2.39), one can show that

$$\mu^2|\hat{\mathbf{A}}(\theta)|^2 = \left(\hat{\mathcal{L}}_4[\hat{\Phi}(\theta)]\right)^2 + \left(\hat{\mathcal{L}}_5[\hat{\Phi}(\theta)]\right)^2 + \frac{(\alpha-1)^2}{2}\left(\hat{\Phi}'(\theta)\right)^2 \tag{2.52}$$

in which $\hat{\mathcal{L}}_4[\cdot]$ and $\hat{\mathcal{L}}_5[\cdot]$ are the second-order linear operators defined as follows

$$\hat{\mathcal{L}}_4[\hat{\Phi}(\theta)] := \frac{1}{4}\left(\frac{\mu}{\kappa} - 1\right)\hat{\Phi}''(\theta) + \left(\frac{\alpha^2}{4}\left(\frac{\mu}{\kappa} - 1\right) + \frac{\alpha(\alpha-1)}{2}\right)\hat{\Phi}(\theta) \tag{2.53}$$

$$\hat{\mathcal{L}}_5[\hat{\Phi}(\theta)] := \frac{1}{4}\left(\frac{\mu}{\kappa} + 1\right)\hat{\Phi}''(\theta) + \left(\frac{\alpha^2}{4}\left(\frac{\mu}{\kappa} + 1\right) + \frac{\alpha}{2}\right)\hat{\Phi}(\theta). \tag{2.54}$$

From (2.52), one has

$$\frac{d}{d\theta}|\hat{\mathbf{A}}(\theta)|^2 = 2\hat{\mathcal{L}}_4[\hat{\Phi}(\theta)]\hat{\mathcal{L}}_4[\hat{\Phi}'(\theta)] + 2\hat{\mathcal{L}}_5[\hat{\Phi}(\theta)]\hat{\mathcal{L}}_5[\hat{\Phi}'(\theta)] + (\alpha-1)^2\hat{\Phi}(\theta)\hat{\Phi}'(\theta). \tag{2.55}$$

Next one shows that the operator $\hat{\mathcal{L}}_3[\cdot]$ in (2.43) takes the form

$$\begin{aligned}\hat{\mathcal{L}}_3[\hat{\Phi}(\theta)] &:= \lim_{r\to 0+} r^{\alpha-4}\,\mathbb{K}(\mathbf{A})\cdot\frac{\mathrm{D}^2\phi(|\mathbf{A}|)}{\phi(|\mathbf{A}|)} \\ &= \beta|\hat{\mathbf{A}}|\Bigg(\mathrm{S}_1\frac{(2-\alpha)(1-\alpha)}{\beta|\hat{\mathbf{A}}|}+\mathrm{S}_2\left[\left(\frac{1}{\beta|\hat{\mathbf{A}}|}\right)''+\frac{(2-\alpha)}{\beta|\hat{\mathbf{A}}|}\right] \\ &\quad -\frac{2(\alpha-1)^2}{4\mu^2}\hat{\Phi}'(\theta)\left(\frac{1}{\beta|\hat{\mathbf{A}}|}\right)'\Bigg). \end{aligned} \tag{2.56}$$

Where S_1 and S_2 are given by

$$\mathrm{S}_1 := \frac{1}{8\mu^2}\left(\frac{\mu^2}{\kappa^2}-1\right)\left(\hat{\Phi}''(\theta)+\alpha^2\,\hat{\Phi}(\theta)\right)+\frac{\alpha(\alpha-1)}{4\mu^2}\hat{\Phi}(\theta) \tag{2.57}$$

$$\mathrm{S}_2 := \frac{1}{8\mu^2}\left(\frac{\mu^2}{\kappa^2}-1\right)\left(\hat{\Phi}''(\theta)+\alpha^2\,\hat{\Phi}(\theta)\right)+\frac{1}{4\mu^2}\left(\hat{\Phi}''(\theta)+\alpha\,\hat{\Phi}(\theta)\right) \tag{2.58}$$

Remark 2:

One important observation for the analysis below is that the asymptotic nonlinear operator $\hat{\mathcal{L}}[\cdot]$ is homogeneous of degree 1 even though the full nonlinear operator in (2.37) has no homogeneity properties. Clearly, it is easy to sees that

$$\hat{\mathcal{L}}[\xi\hat{\Phi}(\theta)] = \xi\hat{\mathcal{L}}[\hat{\Phi}(\theta)] \tag{2.59}$$

for all scalars ξ.

Remark 3:

Since the operator $\hat{\mathcal{L}}[\cdot]$ is nonlinear, the nullset is in general not a subspace of its domain. However, by virtue of (2.59), it is scale *invariant* in that

$$\xi\mathrm{Null}\{\hat{\mathcal{L}}\}\subset\mathrm{Null}\{\hat{\mathcal{L}}\} \tag{2.60}$$

for all $\xi \in \mathbb{R}$.

In order to fully resolve whether or not the nonlinear strain-limiting model predicts the bounded crack-tip stress and strains, we have the following theorem,

Theorem 2.4.1. *Consider the following initial value problem (IVP)*

$$\hat{\mathcal{L}}[\hat{\Phi}(\theta)] = 0 \tag{2.61}$$

$$\hat{\Phi}'(0) = \hat{\Phi}'''(0) = 0 \tag{2.62}$$

$$\hat{\Phi}(0) = v_0 \tag{2.63}$$

$$\hat{\Phi}''(0) = v_2 \tag{2.64}$$

and then seek values of v_0 *and* v_2 *for which*

$$\hat{\Phi}(\pi) = \hat{\Phi}''(\pi) = 0. \tag{2.65}$$

Then, for $1 \leq \alpha \leq 2$*, only when* $v_0 = v_2 = 0$ *does the solution to the IVP (2.61)-(2.64) satisfy the boundary conditions (2.65). Namely, there is only trivial solution* $\hat{\Phi} \equiv 0$ *for the boundary value problem (2.61), (2.62) and (2.65).*

A numerical argument for the proof of the theorem (2.4.1) is postponed to next section. First we will describe a shooting technique based numerical optimization strategy for the two-point boundary value problem (2.61)–(2.65).

2.5 Numerical Solution of the Asymptotic ODE

In [41] Rajagopal and Walton showed that, for the case of a single anti-plane shear crack problem, governed by a class of strain-limiting constitutive model, the fracture BVP does not admit classical crack-tip stress singularity. The proof in [41] depends mainly on the factorization of the corresponding governing second order quasi-

linear PDE. But for the problem considered here, the governing fourth-order PDE doesn't seem to admit a similar factorization. Therefore, we employ a combination of asymptotic and numerical strategy for the proof of the above stated theorem 2.4.1. To that end, we first explain a shooting technique based numerical optimization algorithm and then present a discussion towards the existence of trivial solution for a particular range of α.

2.5.1 Numerical Optimization Startegy

Let $\hat{\Phi}(\theta; \boldsymbol{v}; \alpha)$ denote the solution of the IVP (2.61)-(2.64), in which

$$\boldsymbol{v} := \begin{pmatrix} v_0 \\ v_2 \end{pmatrix} \tag{2.66}$$

with $|v|_2 = \sqrt{v_0^2 + v_2^2} \neq 0$, and $1 \leq \alpha \leq 2$. By virtue of the scale invariance of the solution (2.59) $\xi\hat{\Phi}(\theta; v; \alpha)$ with any $\xi \in R$, is also a solution to the same initial value problem (2.61)-(2.64). Then define the objective functions as

$$f_{\pm}(\boldsymbol{v}) = |\hat{\Phi}_{\pm}(\pi; \boldsymbol{v}; \alpha)| + |\hat{\Phi}''_{\pm}(\pi; \boldsymbol{v}; \alpha)|, \tag{2.67}$$

with $\hat{\Phi}_{\pm}(\pi; \boldsymbol{v}; \alpha)$ denoting the numerical solution of the IVP (2.61)-(2.64). Thus, for our numerical search by shooting technique for the solution, we only need to consider $|v|_2 = 1$, hence v_0 and v_2 are connected by the relation $v_2 = \pm\sqrt{1 - v_0^2}$. Therefore, only two parameters v_0 and α are needed for this numerical study. But the actual numerical calculations were carried out in both directions of v_2, i.e. for both $v_2 = +\sqrt{1 - v_0^2}$ and $v_2 = -\sqrt{1 - v_0^2}$.

The following *algorithm* presents a detailed description of the optimization procedure used to find the minimum value of the objective function $f_{\pm}(v)$ for a particular

value of v_0 and α.

Algorithm 2.5.1 *1. For any $-1 \leq v_0 \leq 1$ and $1 \leq \alpha \leq 2$, using the fourth order Runge-Kutta method, find the solution $\hat{\Phi}_{\pm}(\theta; v_0; \alpha)$ for the initial value problem (2.61)–(2.64).*

2. Then construct the function

$$f_{\pm}(\boldsymbol{v}) = |\hat{\Phi}_{\pm}(\pi; \boldsymbol{v}; \alpha)| + |\hat{\Phi}'_{\pm}(\pi; \boldsymbol{v}; \alpha)|. \tag{2.68}$$

3. Find the minimum value of the objective function $f_{\pm}(\mathbf{v})$ on the rectangular domain

$$1 \leq \alpha \leq 2\,, \qquad -1 \leq v_0 \leq 1, \tag{2.69}$$

by considering 10^3 points on each edge.

4. Then select the each local minimum point of the function $f_{\pm}(v)$ as the initial guess for Newton's method based optimization procedure. This procedure will give the updated minimum value of the function.

*5. If all the updated function values are bigger than the **tolerance**, we can then conclude that there is only a trivial solution for the IVP (2.61)–(2.64), Otherwise, there exists a nontrivial solution.*

2.5.2 Numerical Result

For the numerical computations, we need to consider two cases based on the sign of v_2. The plots of $f_{\pm}(v_0; \alpha)$ is shown in Figures 2.2 and 2.3. As explained in the algorithm, we choose several local minimum points from the plot, and use each of them as an initial guess in Newton optimization algorithm to search the updated function values. Four points are selected from the plot as demonstrated in column one of Ta-

original point	value of $f(v_0;\alpha)$	updated point	updated $f(v_0;\alpha)$
(-0.0101 1.347)	0.047809	(-0.0106 1.3481)	0.02314
(0.0101 1.245)	0.048936	(0.0105 1.2285)	0.02197
(-0.0303 1.204)	0.05290	(-0.03148 1.1885)	0.03758
(-0.0303 1.163)	0.05275	(-0.03189 1.1746)	0.03835

Table 2.1: Updated points and function values by optimization algorithm for the case of $v_2 = +\sqrt{1 - v_0^2}$.

ble 2.1. The second column titled as value of $f(v_0;\alpha)$ illustrates the corresponding function values at these points. Using each of these points as initial guess in optimization generates updated point for local minimum, as shown in column three. The last column calculates the function values in the updated points respectively.

From the values in the second and last columns, we can see that they are all bigger than 0.01, not small enough to produce a solution. We thus conclude that no nontrivial solution exists for the IVP (2.61)–(2.64).

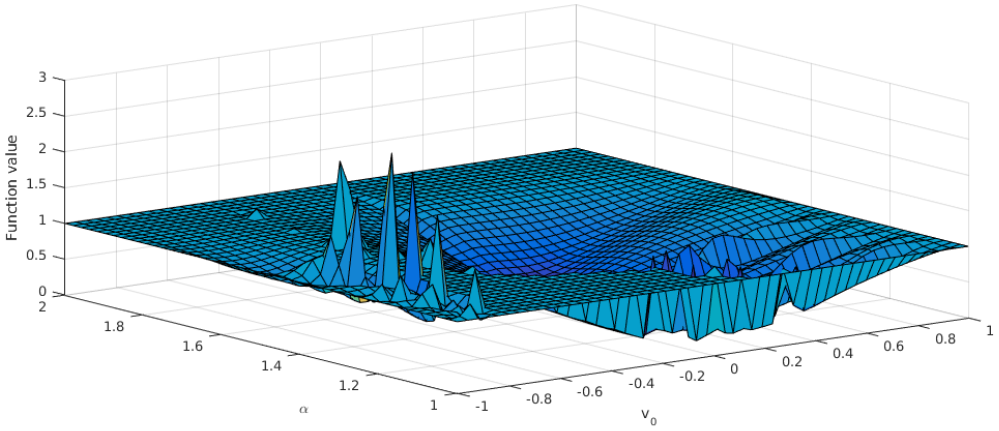

Figure 2.2: The plot of the values of the objective function $f_{\pm}(\boldsymbol{v})$ with $v_2 = +\sqrt{1 - v_0^2}$.

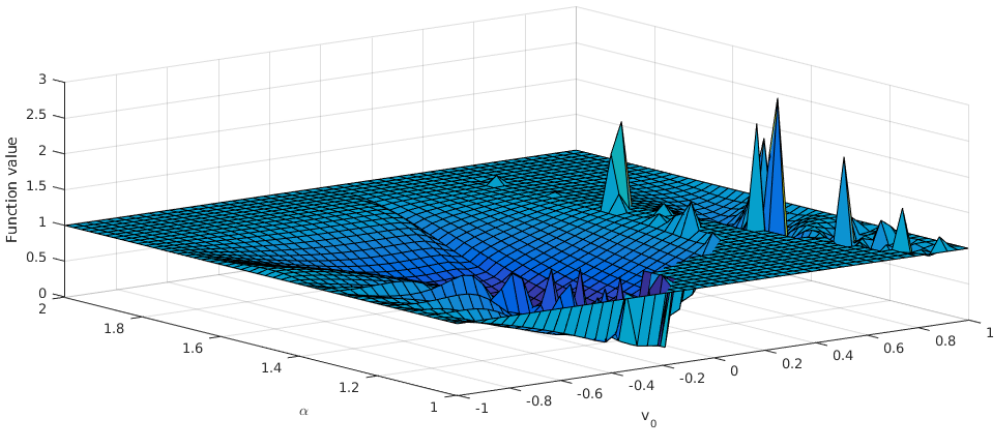

Figure 2.3: The plot of the values of the objective function $f_{\pm}(\boldsymbol{v})$ with $v_2 = -\sqrt{1 - v_0^2}$.

A suggestive proof[4] of the theorem 2.4.1

Proof. The proof of this theorem mainly based on the numerical optimization argument of the IVP (2.61)-(2.64). We first find the minimum value of the objective function $f_{\pm}(\mathbf{v})$ on each of the four sides of the rectangular domain and then using *Newton's* optimization method with previously computed minimum value of $f_{\pm}$ and α as the initial guess. By this procedure we get the minimum values of the objective function (2.68) on the rectangular domain (2.69) greater than 0.01. But the same procedure for the linear crack problem yield zero as the global minimum of (2.68) occurring for $\alpha = 1.5$. Hence we conclude that there is no nontrivial solution for the IVP (2.61)-(2.64) satisfying the boundary condition (2.65).

To be clear we make no claims about the robustness and optimality of the numerical procedure applied here–our principal focus was to obtain preliminary results about the solution behavior to this highly nonlinear problem. Although the numerical procedure

[4]The proof presented here is not mathematically rigorous but it will still give a clear idea of the asymptotic behavior of the solution to nonlinear crack-BVP.

employed here uses only uniform grid points to compute the minimum value of the objective function, but the result obtained is consistent with similar result obtained for the scalar anti-plane shear fracture problem [41]. We believe that the present numerical result is encouraging and we will focus on a more efficient numerical algorithm in the future. A more suited numerical optimization procedure is to choose the non-uniform or adaptive grid points near the local minimum values of the objective function and this will be a topic of future study. □

2.6 Conclusions

In this chapter, we have extended the previous contribution [41] of studying brittle fracture in the context of strain-limiting theories of elasticity to the more challenging plane-strain setting. It is clear that the use of strain-limiting, nonlinear response relations avoids logical inconsistent crack-tip strain singularity. Then a main issue on hand is to verify whether or not the new models predict the same classical crack-tip stress singularity. Here we presented argumets for the plane-strain fracture that any crack-tip stress singularity cannot exist within the general class of asymptotic forms (2.36) for the Airy stress potential. Using a combination of asymptotic and numerical optimization algorithm, we have demonstrated that the use of nonlinear, strain-limiting response relations to study crack-tip solution behavior in brittle elastic solids, predicts bounded stress in the neighborhood of crack-tip.

3. NUMERICAL MODEL FOR PLANE-STRAIN FRACTURE IN A CLASS OF STRAIN-LIMITING NONLINEAR ANISOTROPIC ELASTIC BODIES

In this chapter, we develop a numerical model for the opening mode fracture within the context of strain-limiting theory of elasticity. We first derive a governing quasi-linear elliptic partial differential equation for the displacement-vector in the body and then give a detailed finite element formulation along with the corresponding numerical results. Our main aim is to illustrate whether or not the nonlinear strain-limiting response relations predict a physically reasonable crack-tip stress and strain.

3.1 Mathematical Model

Consider a two-dimensional (2D) infinite, linear, anisotropic elastic body Ω containing a straight, Griffith crack of length $2l$ and occupies the segment $-l \leq x_1 \leq l$ and $x_2 = 0$. The body is subjected to a far-field, uniform, tensile load σ. The physical domain and the loading condition is depicted in Figure 3.1. In this chapter, our attention is restricted to the numerical implementation of a quasi-static fracture problem, hence we assume no crack-growth due to loading. The plane-strain assumption yield two independent displacement components which only depend on the in-plane coordinates. Let $\mathbf{u} = (u_1(x_1, x_2), u_2(x_1, x_2))$ denote the displacement field in the body. For the quasi-static problem on hand, we utilize a strain-limiting nonlinear response relation developed in [28] of the form:

$$\boldsymbol{E} = \mathcal{F}(\bar{\boldsymbol{S}}), \tag{3.1}$$

relating the Green-St.Venant strain $\boldsymbol{E}$ and Second Piola-Kirchhoff stress tensor $\bar{\boldsymbol{S}}$. The right-hand-side of the above equation (3.1) is a uniformly bounded function of $\bar{\boldsymbol{S}}$.

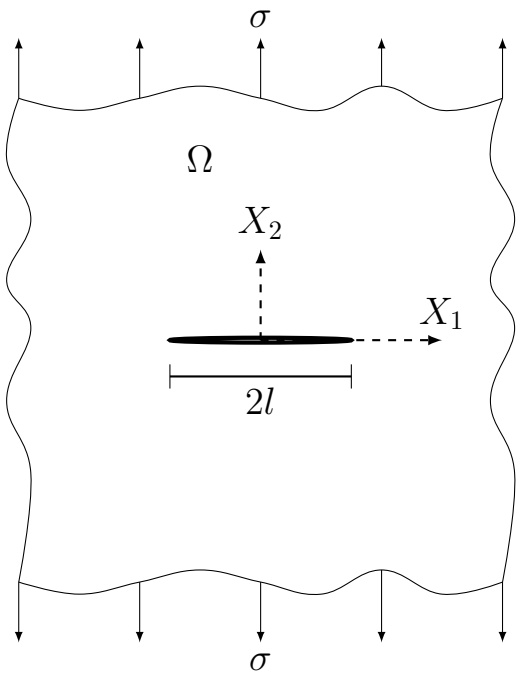

Figure 3.1: Infinite elastic slab with crack of length $2l$ under pure mode I loading

Then under the assumption of "small" displacement gradients of the form:

$$\sup |\nabla_{\boldsymbol{x}} \boldsymbol{u}| = o(\delta) \quad \delta \ll 1, \tag{3.2}$$

with the symbol $|\cdot|$ denoting the Frobenius norm and $o(\cdot)$ is the **little-o** notation, it follows that:

$$\boldsymbol{E} = \boldsymbol{\epsilon} + o(|\nabla \boldsymbol{u}|) \tag{3.3}$$

and hence that (3.1), in the infinitesimal strain regime, can be approximated by:

$$\boldsymbol{\epsilon} = \mathcal{F}(\bar{\boldsymbol{S}}) \tag{3.4}$$

in which $\boldsymbol{\epsilon}$ denotes the customary linearized strain tensor, i.e.

$$\boldsymbol{\epsilon} := \frac{1}{2}\left(\nabla \boldsymbol{u} + \nabla \boldsymbol{u}^{\mathrm{T}}\right). \tag{3.5}$$

The above constitutive equation (3.4) can be written for the special case of strain-limiting response relation in the infinitesimal regime as:

$$\boldsymbol{\epsilon} = \tilde{\phi}\left(|\mathbb{K}^{1/2}[\boldsymbol{S}]|\right)\mathbb{K}[\boldsymbol{S}] \tag{3.6}$$

with $\tilde{\phi}(r)$ given by

$$\tilde{\phi}(r) := \frac{1}{(1+(\beta r)^{\alpha})^{1/\alpha}}. \tag{3.7}$$

in which both α and β are modeling parameters and $\frac{1}{\beta}$ gives the limiting-strain norm. Note that when $\beta = 0$, the model (3.6)-(3.7) will be the reference linearized elasticity model. Further, a main motivation for considering such a nonlinear function (3.7) is from the study of Bulíček et al [12]. They have provided a proof of the existence of weak solution to the anti-plane stress problem on V-notch domains. The existence and uniqueness of solution to the new class of strain-limiting nonlinear elasticity models was studied for both convex and non-convex domains. The form of the nonlinear function considered here (3.7) is same as the one studied in [12]. The authors have proved the existence of weak solution to the non-convex anti-plane stress scalar problem for $a \in (0,2)$[1] and further for the convex domains the weak solution exists for $a \in (0,\infty)$.

Remark 1: Mai and Walton [28] showed that models of the type (3.1), (3.4), (3.7) can fail to be rank-one convex (strongly elliptic) if strains become too large but are rank-one convex otherwise. Also Mai and Walton [28] gave the sufficient condition for

[1]Note that the symbol a in equation (2.6) of [12] is same of the parameter α used in our study.

the invertibility of the strain-limiting models of the type (3.1) and showed how one can construct the hyperelastic models from (3.1).

Then we consider an inverted form of the above constitutive relationship (3.1), also we know that there is no distinction between the Stress tensors $\bar{\boldsymbol{S}}$ and $\boldsymbol{\sigma}$, one can rewrite the stress as a function of strain as:

$$\boldsymbol{\sigma} = \frac{\mathbb{E}[\boldsymbol{\epsilon}]}{(1 - (\beta|\mathbb{E}^{1/2}[\boldsymbol{\epsilon}]|)^{\alpha})^{1/\alpha}}. \tag{3.8}$$

In this chapter, we study two important cases of isotropy and transverse isotropy. For isotropic elastic material,

$$\mathbb{E}[\boldsymbol{\epsilon}] := 2\mu\boldsymbol{\epsilon} + \lambda(\boldsymbol{\epsilon} \cdot \boldsymbol{I})\boldsymbol{I} = 2\mu\left(\boldsymbol{\epsilon} + \frac{\nu}{1-2\nu}(\boldsymbol{\epsilon} \cdot \boldsymbol{I})\boldsymbol{I}\right) \tag{3.9}$$

with μ and λ denoting the customary Lamé parameters and ν denoting Poisson's ratio. In (3.9), $(\boldsymbol{\epsilon} \cdot \boldsymbol{I})$ is the trace-inner-product and $\boldsymbol{I}$ denotes the second-order identity tensor. For transversely isotropic material,

$$\mathbb{E}[\boldsymbol{\epsilon}] := 2\mu\boldsymbol{\epsilon} + \lambda(\boldsymbol{\epsilon} \cdot \boldsymbol{I})\boldsymbol{I} + \gamma(\boldsymbol{\epsilon} \cdot \boldsymbol{M})\boldsymbol{M} \tag{3.10}$$

with $\boldsymbol{M} = \boldsymbol{m} \otimes \boldsymbol{m}$ being the norm-one, rank-one, structural tensor with the unit-vector $\boldsymbol{m}$ defining the axis of symmetry. For the structural tensor $\boldsymbol{M}$, we consider two special cases such as:

(1) $\boldsymbol{M} = \boldsymbol{e}_1 \otimes \boldsymbol{e}_1$ then $\boldsymbol{\epsilon} \cdot \boldsymbol{M} = \epsilon_{11}(x_1, x_2)$

(2) $\boldsymbol{M} = \boldsymbol{e}_2 \otimes \boldsymbol{e}_2$ then $\boldsymbol{\epsilon} \cdot \boldsymbol{M} = \epsilon_{22}(x_1, x_2)$.

Where ϵ_{11} and ϵ_{22} are respectively $1-1$ and $2-2$ component's of the strain-tensor. The case (1) corresponds to the case in which the axis of the crack is assumed to be

along $\boldsymbol{e}_1$. and in case (2) the axis of the crack is assumed to be orthogonal to $\boldsymbol{e}_2$. For the remainder of this chapter, all calculations are shown for case (1). But some representative numerical results are also presented for case (2).
Then rewriting (3.10) as:

$$\mathbb{E}[\boldsymbol{\epsilon}] := \mu \left(2\,\boldsymbol{\epsilon} + \bar{\gamma_1}\ (\boldsymbol{\epsilon} \cdot \boldsymbol{I})\boldsymbol{I} + \bar{\gamma_2}\ \epsilon_{11}\boldsymbol{e}_1 \otimes \boldsymbol{e}_1\right), \tag{3.11}$$

in which $\bar{\gamma_1} = \frac{2\nu}{1-2\nu}$ and $\bar{\gamma_2} = \frac{\nu}{\mu}$. Using (3.11) in (3.8) and non-dimensionalize the stresses by the shear modulus and length scales by l (half length of the crack). Hence the only material parameter required for the computations is Poisson's ratio ν.

In the absence of body force, the stress tensor needs to satisfy the equilibrium equation

$$\operatorname{div} \boldsymbol{\sigma} = \boldsymbol{0} \qquad \text{in} \quad \Omega\,, \tag{3.12}$$

where div is the divergence operator.

For the classical, isotropic, problems in elasticity, there are two main methods that one can use to solve the boundary value problems. In the first method, one work with displacement field as the primary unknown and then the conservation of linear momentum leads to Navier equations. In such approaches the strain-compatibility conditions will be automatically satisfied. The second method introduces a scalar potential which automatically satisfies equilibrium equation and then work with the compatibility condition for strains. The latter method needs higher regularity for the space of test functions if one chooses to solve the corresponding boundary value problem (BVP) using a finite element method. Therefore, we choose work with the former method, hence in our finite element formulation displacement is the primary unknown and we seek the (*weak*-)solution to equilibrium equation.

3.2 Numerical Model

In the case of two-dimensional, pure mode-I type of loading the horizontal displacements are symmetric and the vertical displacements are anti-symmetric, i.e.

$$u_1(X_1, -X_2) = u_1(X_1, X_2), \tag{3.13}$$

$$u_2(X_1, -X_2) = -u_2(X_1, X_2), \tag{3.14}$$

$$u_3(X_1, X_2) = 0 \quad \text{(plane strain assumption)}. \tag{3.15}$$

Also in plain-strain problems normal stresses are symmetric and shear stresses are anti-symmetric, i.e.

$$\sigma_{11}(X_1, -X_2) = \sigma_{11}(X_1, X_2), \tag{3.16}$$

$$\sigma_{22}(X_1, -X_2) = \sigma_{22}(X_1, X_2), \tag{3.17}$$

$$\sigma_{12}(X_1, -X_2) = -\sigma_{12}(X_1, X_2). \tag{3.18}$$

Therefore, the solution to pure mode-I problem is symmetric about both X_1 and X_2 axes. Hence we reduce the problem from the entire plane to the upper right quarter-plane. But for the numerical implementation we approximate the upper right quarter-plane by a finite square domain $D = [-b, 0] \times [b, 2b]$ and the same is depicted in Figure 3.2. Further, since the nondimensionalized half-length of the crack is 1, then we have to choose b sufficiently large. The upper crack surface in the undeformed configuration is denoted by $\Gamma_0 = [0, 1] \times \{0\}$. So that the mid-point of the upper-crack face is at the origin.

Using the inverted constitutive relation (3.8) in the equilibrium equation (3.12) we

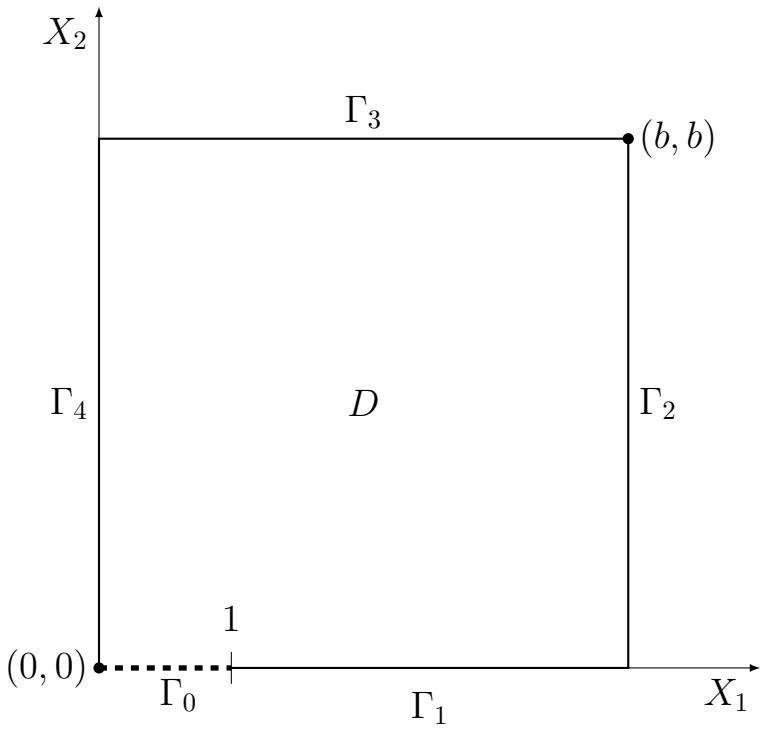

Figure 3.2: Finite computational domain for pure mode-I fracture problem.

get a second order, quasilinear partial differential equation (PDE)

$$-\nabla \cdot \left(\frac{\nabla \mathbf{u} + \nabla \mathbf{u}^T + \bar{\gamma_1} \nabla \cdot \mathbf{u}\, \mathbf{I} + \bar{\gamma_2}\, u_{1,1} \boldsymbol{e}_1 \otimes \boldsymbol{e}_1}{\left(1 - \left(\beta \left|\mathbb{E}^{1/2}\left[\boldsymbol{\epsilon}\right]\right|\right)^{\alpha}\right)^{1/\alpha}} \right) = \mathbf{0} \quad \text{in} \quad D. \tag{3.19}$$

Boundary Conditions:

Here we briefly explain the boundary conditions for our numerical simulation. The classical fracture boundary value problem imposes zero-traction on the crack-face Γ_0. The right-face Γ_2 is also kept traction-free. The top-face Γ_3 is still subjected to the uniform tensile-load σ. But the symmetry of the solution results in some new boundary condition on the bottom-face Γ_1 and the left-face Γ_4. First on the bottom-face, the opening plane displacement component vanishes along the line directly ahead of the

crack-tip (i.e. for $1 \leq X_1 \leq b$, $X_2 = 0$) and the shear component of the stress also vanish along the bottom-face i.e.

$$u_2(X_1, 0) = 0, \tag{3.20}$$

$$\sigma_{12}(X_1, 0) = 0. \tag{3.21}$$

Similarly, along the left-face Γ_4 (i.e. for $1 \leq X_2 \leq b$, $X_1 = 0$) both the horizontal displacement component and the shear component of the stress tensor along with $u_{1,2}(0, X_2)$ are all zero, i.e.

$$u_1(0, X_2) = 0, \tag{3.22}$$

$$u_{1,2}(0, X_2) = 0, \tag{3.23}$$

$$\sigma_{12}(0, X_2) = 0. \tag{3.24}$$

Combining all the above we have the following boundary conditions,

$$\text{on} \quad \Gamma_0 \quad \boldsymbol{\sigma}\,\vec{n} = \mathbf{0}, \tag{3.25}$$

$$\text{on} \quad \Gamma_1 \quad u_2(x, 0) = 0 \quad \text{and} \quad \sigma_{12}(x, 0) = 0, \tag{3.26}$$

$$\text{on} \quad \Gamma_2 \quad \boldsymbol{\sigma}\,\vec{n} = \mathbf{0}, \tag{3.27}$$

$$\text{on} \quad \Gamma_3 \quad \boldsymbol{\sigma}\,\vec{n} = \begin{pmatrix} 0 \\ \sigma \end{pmatrix} \tag{3.28}$$

$$\text{on} \quad \Gamma_4 \quad u_1(0, y) = 0, \quad \sigma_{12}(0, y) = 0$$

$$\text{and} \quad u_{2,1}(0, y) = 0. \tag{3.29}$$

Here $\vec{n}$ denotes a unit normal vector, σ is the uniform tensile load on the top surface and σ_{12} is the $(1,\ 2)-$component of the Cauchy stress tensor $\boldsymbol{\sigma}$. Finally, the PDE (3.19) together with the boundary conditions (3.25)-(3.29) constitutes the nonlinear fracture boundary value problem for the new class of strain-limiting elastic bodies.

3.3 Finite Element Implementation

For the nonlinear material model studied in this chapter, one needs to solve the quasilinear elliptic PDE system (3.19) subjected to the boundary conditions (3.25)-(3.29). But this doesn't seems to admit a possibility of an exact solution, hence we choose to solve the BVP by a finite element method. First we linearize the PDE (3.19) using *damped Newton's method* and then use a standard Galerkin FEM to find the numerical solution. In the method implemented here, we compute the $(n+1)^{st}$ approximate solution using the previous n^{th} solution and to achieve a better global convergence of the numerical solution we use a damping parameter, α^n. Further, we use a back tracking line search algorithm to compute α^n at each inner *Newton* iterations.

The *Newton's method* used to solve the above boundary value problem takes the form:

$$F'\left(\mathbf{u^n}, \delta\mathbf{u^n}\right) = -F(\mathbf{u^n}) \tag{3.30}$$

$$\mathbf{u^{n+1}} = \mathbf{u^n} + \alpha^{\mathbf{n}}\delta\mathbf{u^n}. \tag{3.31}$$

Here α^n is the step length, and the function $F(\cdot)$ is given by the following:

$$F(\mathbf{u}) = -\nabla\cdot\left(\frac{\nabla\mathbf{u} + \nabla\mathbf{u^T} + \bar{\gamma_1}\,\nabla\cdot\mathbf{u}\,\mathbf{I} + \bar{\gamma_2}\,\mathbf{u}_{1,1}\mathbf{e_1}\otimes\mathbf{e_1}}{\left(\mathbf{1} - \left(\beta\,|\mathbb{E}^{\mathbf{1/2}}\ [\boldsymbol{\epsilon}]\,|\right)^{\alpha}\right)^{\mathbf{1}/\alpha}}\right). \tag{3.32}$$

In the *Newton's method* (3.30) the symbol F' denotes the Fréchet derivative of F in

the direction of $\delta\mathbf{u}$ and is defined as:

$$F'(\mathbf{u}, \delta\mathbf{u}) = \lim_{h\to 0} \frac{F(\mathbf{u} + h\,\delta\mathbf{u}) - F(\mathbf{u})}{h}\ . \tag{3.33}$$

Using (3.32) in (3.33) and after a lengthy calculation we get the following expression for F':

$$F' = -\nabla\cdot\left[\frac{\nabla\delta\mathbf{u} + \nabla\delta\mathbf{u}^T + \bar{\gamma_1}\,\nabla\cdot\delta\mathbf{u}\,\mathbf{I} + \bar{\gamma_2}\,\delta u_{1,1}\boldsymbol{e}_1\otimes\boldsymbol{e}_1}{(1-\beta^\alpha\ |\mathbb{E}^{1/2}\ [\boldsymbol{\epsilon}]\,|^\alpha)^{1/\alpha}} - \frac{\beta^\alpha\ \mathbb{E}[\boldsymbol{\epsilon}]\ \theta_1\{\mathbf{u}\}\ \theta_2\{\mathbf{u},\delta\mathbf{u}\}}{(1-\beta^\alpha\ |\mathbb{E}^{1/2}\ [\boldsymbol{\epsilon}]\,|^\alpha)^{1+1/\alpha}}\right], \tag{3.34}$$

in which the functions $|\mathbb{E}^{1/2}\,[\boldsymbol{\epsilon}]\,|$, $\theta_1\{\mathbf{u}\}$ and $\theta_2\{\mathbf{u},\delta\mathbf{u}\}$ are defined as follows:

$$\begin{aligned}
\left|\mathbb{E}^{1/2}\,[\boldsymbol{\epsilon}]\right|^2 &= \mathbb{E}^{1/2}[\boldsymbol{\epsilon}]\colon \mathbb{E}^{1/2}\,[\boldsymbol{\epsilon}] \\
&= \boldsymbol{\epsilon}\colon \mathbb{E}^{1/2}[\mathbb{E}^{1/2}\,[\boldsymbol{\epsilon}]] \\
&= \boldsymbol{\epsilon}\colon \mathbb{E}\,[\boldsymbol{\epsilon}] \\
&= \frac{1}{2}\left(\nabla\mathbf{u} + \nabla\mathbf{u}^T\right)\colon\ \left(\nabla\mathbf{u} + \nabla\mathbf{u}^T\right) +\ \bar{\gamma_1}\ (\nabla\cdot\mathbf{u})^2 +\ \bar{\gamma_2}\ (u_{1,1})^2 \\
\theta_1\{\mathbf{u}\} &= \left|\mathbb{E}^{1/2}\,[\boldsymbol{\epsilon}]\right|^{\alpha-2} \\
\theta_2\{\mathbf{u},\delta\mathbf{u}\} &= \frac{1}{2}\left(\left|\mathbb{E}^{1/2}\,[\boldsymbol{\epsilon}]\right|^2\right)' \\
&= \left(\nabla\mathbf{u} + \nabla\mathbf{u}^T\right)\colon\ \left(\nabla\delta\mathbf{u} + \nabla\delta\mathbf{u}^T\right) +\ \bar{\gamma_1}\ (\nabla\cdot\mathbf{u})\,(\nabla\cdot\delta\mathbf{u}) +\ \bar{\gamma_2}\,u_{1,1}\,\delta u_{1,1}.
\end{aligned}$$

Substituting (3.34) in (3.30), we get the linearized PDE in which we want to solve for the Newton update $\delta\mathbf{u}$ by knowing the previous solution $\mathbf{u}$,

$$\begin{aligned}
&-\nabla\cdot\left[\frac{(\nabla\delta\mathbf{u} + \nabla\delta\mathbf{u}^T) + \bar{\gamma_1}\,(\nabla\cdot\delta\mathbf{u})\,\mathbf{I} + \bar{\gamma_2}\,\delta u_{1,1}\boldsymbol{e}_1\otimes\boldsymbol{e}_1}{(1-\beta^\alpha\ |\mathbb{E}^{1/2}\,[\boldsymbol{\epsilon}]\,|^\alpha)^{1/\alpha}} - \frac{\beta^\alpha\ \mathbb{E}[\boldsymbol{\epsilon}]\ \theta_1\{\mathbf{u}\}\ \theta_2\{\mathbf{u},\delta\mathbf{u}\}}{(1-\beta^\alpha\ |\mathbb{E}^{1/2}\ [\boldsymbol{\epsilon}]\,|^\alpha)^{1+1/\alpha}}\right] \\
&= \nabla\cdot\left[\frac{(\nabla\mathbf{u} + \nabla\mathbf{u}^T) + \bar{\gamma_1}\ (\nabla\cdot\mathbf{u})\,\mathbf{I} + \bar{\gamma_2}\,u_{1,1}\boldsymbol{e}_1\otimes\boldsymbol{e}_1}{(1-\beta^\alpha\ |\mathbb{E}^{1/2}\,[\boldsymbol{\epsilon}]\,|^\alpha)^{1/\alpha}}\right].
\end{aligned} \tag{3.35}$$

Starting with the above linearized strong formulation (3.35), one can find the weak formulation by integrating (3.35) against the test function $\mathbf{v} = (v_1, v_2)$ over the domain D and using the boundary values appropriately.

The weak formulation of the solution algorithm requires finding $\delta\mathbf{u} \in \mathcal{U}$ such that

$$A_{\mathbf{u}}(\delta\mathbf{u}, \mathbf{v}) = L_{\mathbf{u}}(\mathbf{v}) \qquad \forall \quad \mathbf{v} \in \mathcal{U} \tag{3.36}$$

in which $A_{\mathbf{u}}(\delta\mathbf{u}, \mathbf{v})$ and $L_{\mathbf{u}}(\mathbf{v})$ are bilinear and linear forms respectively given by:

$$\begin{aligned} A_{\mathbf{u}}(\delta\mathbf{u}, \mathbf{v}) = \int_D \Bigg\{ & \frac{\left(\nabla\delta\mathbf{u} + \nabla\delta\mathbf{u}^T + \bar{\gamma_1}\,\nabla\cdot\mathbf{u}\,\mathbf{I} + \bar{\gamma_2}\,u_{1,1}\boldsymbol{e}_1\otimes\boldsymbol{e}_1\right) : \mathbf{v}}{\left(1 - \beta^\alpha\,|\mathbb{E}^{1/2}\,[\boldsymbol{\epsilon}]\,|^\alpha\right)^{1/\alpha}} \\ & + \frac{\beta^\alpha\;\theta_1\{\mathbf{u}\}\;\theta_2\{\mathbf{u}, \delta\mathbf{u}\}\;\mathbb{E}[\boldsymbol{\epsilon}]\colon \mathbf{v}}{\left(1 - \beta^\alpha\,|\mathbb{E}^{1/2}\,[\boldsymbol{\epsilon}]\,|^\alpha\right)^{1+1/\alpha}} \Bigg\}\, dD\,, \end{aligned} \tag{3.37}$$

$$\begin{aligned} L_{\mathbf{u}}(\mathbf{v}) = & -\int_D \frac{\left(\nabla\mathbf{u} + \nabla\mathbf{u}^T + \bar{\gamma_1}\,\nabla\cdot\mathbf{u}\,\mathbf{I} + \bar{\gamma_2}\,u_{1,1}\boldsymbol{e}_1\otimes\boldsymbol{e}_1\right) : \mathbf{v}}{\left(1 - \beta^\alpha|\mathbb{E}^{1/2}\,[\boldsymbol{\epsilon}]\,|^\alpha\right)^{1/\alpha}}\, dD \\ & + \int_{\Gamma_4} v_2\,\sigma\,, \end{aligned} \tag{3.38}$$

where $\mathcal{U}$ is the *Sobolev* space given by

$$\mathcal{U} := \left\{\mathbf{u} \in H^1(D) :\; u_2|_{\Gamma_1} = 0 \text{ and } \; u_1|_{\Gamma_4} = 0\right\}. \tag{3.39}$$

A corresponding conforming finite element formulation is given by: for any $h > 0$, let $\mathcal{T}_h$ be the discretization of D into quadrilaterals K with diameter h_K less than h. Let $\mathcal{U}_h$ be the finite dimensional subspace of $\mathcal{U}$ defined by:

$$\mathcal{U}_h = \Big\{ \mathbf{u}_h \in C^0\left(\bar{D},\ \mathbb{R}^2\right) : \mathbf{u}_h|_K \in (\mathbb{Q}_1)^2 \quad \forall \quad K \in \mathcal{T}_h, \\ u_{h2}|_{\Gamma_1} = 0,\, u_{h1}|_{\Gamma_4} = 0 \Big\} \cap H^1\left(D,\ \mathbb{R}^2\right), \quad (3.40)$$

in which $\mathbf{u}_h = (u_{h1}, u_{h2})$ is a smooth test function. Then the discrete finite element formulation reads: find $\delta\mathbf{u}_h \in \mathcal{U}_h$ such that

$$A_{\mathbf{u}}(\delta\mathbf{u}_h, \mathbf{v}_h) = L_{\mathbf{u}}(\mathbf{v}_h) \qquad \forall \quad \mathbf{v}_h \in \mathcal{U}_h. \quad (3.41)$$

3.4 Numerical Implementation

To solve the nonlinear fracture boundary value problem and the corresponding variational formulation developed in the previous section, we have used a continuous Galerkin Finite Element Method (FEM) [18]. The C++ language based computational program was developed using the open source *deal.II* library [5, 6]. More information about the library can be found using the webiste `http://www.dealii.org/`.

For our computational model, we assume that the material is a transversely isotropic brittle elastic solid. The various parameters used in the computation are as follows: the Poisson's ration is 0.35, the strain-limiting parameter $\beta = 0.0, 0.09, 0.5, 1.0, 2.0, 10.0$ and $\alpha = 1.0, 0.9, 1.8$. In most of the computations, (dimensionless) uniform loading on the top face was fixed as $\sigma = 0.001$. We have also studied the effect of σ on the solution and also on the crack-tip stress.

Our main aim in this chapter is to illustrate the difference in predictions of stress and strain near the crack-tip exhibited by the reference linearized model and the nonlinear strain-limiting model. Also, we are interested in knowing whether or not the strain-limiting model predict a smooth cusp-shaped crack-opening displacement

profile.

3.4.1 Mesh Refinement Strategy

The accuracy of the finite element solution of the discrete weak form (3.41) depends primarily on the mesh size. This can be realized by deriving *a priori* error estimates which are mainly in terms of the exact solution u and the computed numerical solution u_h. For the simple case of Laplace equation, one can obtain *a priori* error estimates [18] as

$$||u - u_h|| \leq Ch^2, \tag{3.42}$$

in which h is the maximum size of the each element and the constant C depends on the exact solution u, the domain, shape functions and also on the dimension of the problem, but it is independent of the mesh size h. But for the problem considered in this work we don't have the exact solution on hand. Hence the numerical value of the constant C is unknown and therefore the numerical bound as given in (3.42) can't be computed. Also, a global mesh refinement based approach can reduce the error in the numerical solution, but computationally this may not be an efficient strategy. In addition, for the domain with high stress concentration region, such as crack or re-entrant notch, a fine mesh is necessary in the neighborhood of these regions where the solution varies considerably.

A major issue in generating adaptive meshes for the computations is how to estimate which cell is to be refined or coarsened. To this end a number of studies available in the finite element literature [4, 22], which provide a criteria for the adaptive mesh refinements. In this work, we employ a *posterior* error estimator developed for Laplace equation by Gago et al. in [22] and the same as been implemented in the *deal.II* library. The numerical code exploits the *KellyErrorEstimator* functionality of the *deal.II* library to get adaptive meshes for the numerical simulations.

Here we briefly explain the adaptive mesh refinement idea of [22]. Suppose η_K denotes the error indicator in the finite element solution and it is defined as:

$$\eta_K = \frac{h}{24} \int_{\partial K} [\partial_n u_h]^2 \, ds, \tag{3.43}$$

where $[\partial_n u_h]$ is the jump in the normal derivative of the finite element solution of u_h, across the element boundary ∂K. After the computation of the error estimator for each cell we then need to decide which cells should be refined or coarsened. In the numerical code, we refine the 30% of cells with highest error indicator η_K and coarsen those of 3% of elements with lowest errors. The implemented solution algorithm consists of the successive application of the following loop, i.e.

$$\text{SOLVE} \;\rightarrow\; \text{ESTIMATE} \;\rightarrow\; \text{MARK} \;\rightarrow\; \text{REFINE}. \tag{3.44}$$

Figure 3.3 illustrates the global and adaptive refinements of the computational domain. Both figures are obtained by refining the computational domain 6 times globally and adaptively. In the case of adaptive refinement of the domain, we notice that around the crack-tip the density of the mesh is far larger than the other parts of the domain. Small cells near the crack-tip are justified in order to capture the sharp variations in the quantities of interest. However, we do not need such high levels of refinement in the large portion of the domain away from the crack-tip neighborhood, using a highly refined mesh (in the case of global mesh refinement) is a waste of computational effort and cost. This point is clearly emphasized in Figure 3.3.

3.4.2 Algorithm

The main steps involved in the computation of the numerical solution of the non-linear fracture boundary value problem are listed as follows:

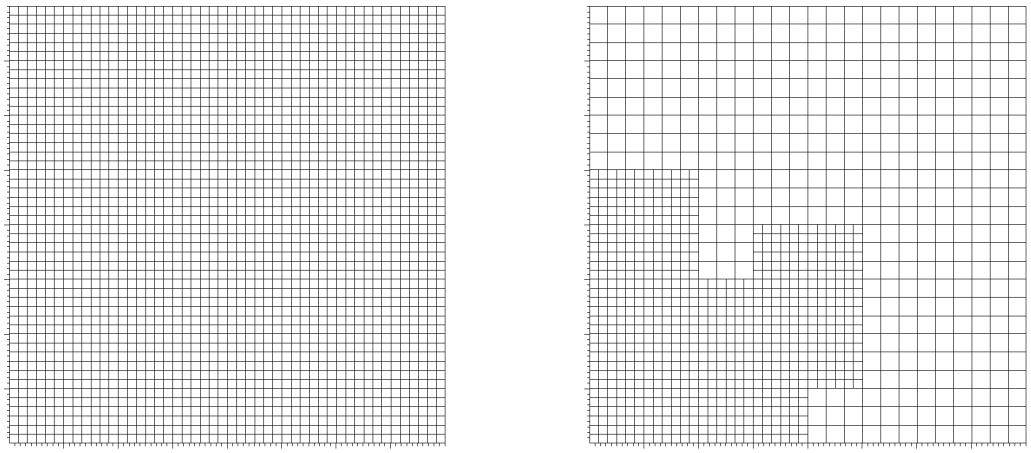

(a) Global-refinement (b) Adaptive-refinement

Figure 3.3: Computational domain indicating both global and adaptive mesh refinement.

(1) Load the run-time parameters such as uniform far-field load σ, modeling parameters β and α, the material parameter poisson's ration ν, from the parameter-file.

(2) Create a coarse domain $[0, b] \times [0, b]$ and indicate the boundary parts such as crack-face, bottom boundary (*excluding* crack-face), left, right and top boundary. Mark these parts of the boundary for applying boundary conditions later.

(3) Set up the vector valued, bilinear (i.e. Q_1), finite element and the corresponding degrees of freedom.

(4) Start with a function $\mathbf{u}^0 = \mathbf{0}$ and modify it in such a way that the values of $\mathbf{u}^0$ along the boundary are equal to the correct boundary values.

(5) Assemble the system for the *Newton update*, $\delta\mathbf{u}^n$, and add in the contribution of the boundary condition on the top surface.

(6) Solve the resulting linear system using a *conjugate gradient* method since the matrix for the *Newton update* is symmetric and positive definite.

(7) Compute a step length, α^n, using a backtracking line search algorithm.

(8) Then compute the new approximate solution by

$$\mathbf{u}^{n+1} = \mathbf{u}^n + \alpha^n \delta \mathbf{u}^n.$$

(9) Repeat the inner *Newton* iterations.

(10) Post-processing: output the numerical results, these include the displacements (both u_1 and u_2) on the entire body, the crack-face displacement $u_2(x_1, 0)$, the stress component σ_{22} and the strain component ϵ_{22} along the line ahead of the crack-tip.

3.5 Numerical Results and Discussion

The discrete weak formulation (3.41) defined in the previous section was solved using a Finite Element Method (FEM). The main objective of the numerical computation is to study the effect of the modeling parameters such as the strain-limiting parameter β and the power of the nonlinear function $\phi(\cdot)$ on the solution of the nonlinear fracture boundary value problem.

In our numerical code, the initial uniform coarse mesh was adaptively refined thirteen times so that the final mesh had close to $1,947,554$ total degrees of freedom, with over 200,000 active cells. Table 3.1 shows the number of refinement cycle, the number of total active cells and the total DOF used for a square domain with $b = 8$. The zeroth refinement cycle refers to the initial coarse mesh of the domain, which contains 64 cells and 1 cell on the crack-face. We typically ran the program for 13 refinement

cycles, for which the final cycle has more than a thousand cells along the crack face.

Cycle	Total Active Cells	Total DOF
0	64	578
1	124	1,118
2	238	2,214
3	454	3,974
4	862	7,626
5	1,639	14,800
6	3,115	28,390
7	5,908	53,832
8	11,209	102,376
9	21,229	195,536
10	40,138	370,704
11	75,844	699,422
12	143,176	1,323,432
13	210,508	1,947,554

Table 3.1: Number of refinements, total number of cells and degree of freedom for the computational domain.

To validate our numerical code for the nonlinear problem, we have performed two tasks. We first created a domain without a crack in it and tested the code for the prescribed tensile load. We observed that the value of the stress component σ_{22} is uniform throughout the domain. Secondly, we considered the "real" domain that is described in Section-(3.2) and set $\beta = 0$ in the nonlinear constitutive model (3.19).

Suppose $u_2^L(\Gamma_0)$ denotes the Y-displacement of the linear problem on the crack-face, similarly $u_2^{NL}(\Gamma_0)$ indicates the crack-face Y-displacement of the nonlinear problem (with $\beta = 0$ and $\alpha = 1.0$). Then the "relative-difference" (RD) in values of $u_2(\Gamma_0)$ on the crack-face is obtained using the formula:

$$\text{RD} := \frac{\left|u_2^L(\Gamma_0) - u_2^{NL}(\Gamma_0)\right|_\infty}{|u_2^L(\Gamma_0)|_\infty} \tag{3.45}$$

in which $|\cdot|_\infty$ denotes the l^∞ norm. The computed value of the above quantity RD is 4.6497E-7, which is reasonable and we believe that this difference is not significant. Hence we believe that, when $\beta = 0$, the solution to the nonlinear fracture problem tend to the general solution to the reference linear fracture problem. Also, solution to the nonlinear fracture problem is sensitive to the limiting-strain modeling parameter β, the following simulation results clearly shows that for $\beta \gg 1$, even very near the (mathematical) crack-tip, both stress and strain remain smaller in magnitude compared with the corresponding values from classical LEFM model. Further, in all the following graphs, the "dots" means the value of the variable presented in the corresponding graph. A uniform mesh points are selected along the bottom-face of the domain, but the underlying computational mesh is fine and there is clearly a "large" number of quadrature points exist between any two points used to plot the following graphs.

Figure 3.4, and 3.5 indicates the comparison of LEFM and the strain-limiting model with parameters $\beta = 0$, $\alpha = 1.0$, $\sigma = 0.001$ and $\bar{\gamma_2} = 1.0$. In the computations for all these figures the axis of the crack was assumed to be along $\boldsymbol{e}_1$. The crack-face displacement profile u_2 is depicted in Figure 3.4 and the plot of dimensionless stress component (σ_{22}/σ) is shown in Figure 3.5.

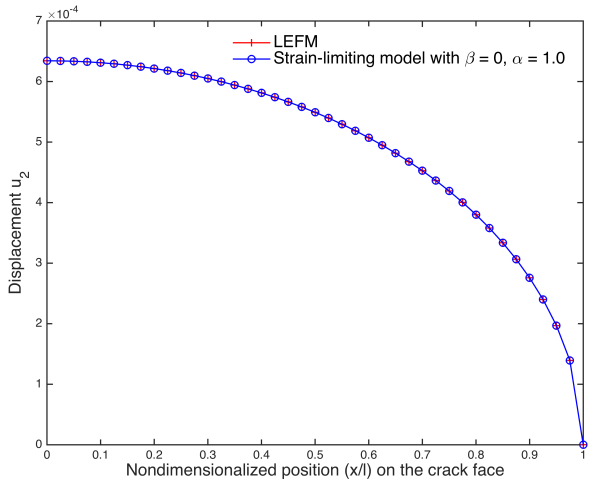

Figure 3.4: Crack-face displacement u_2 both for LEFM and strain-limiting anisotropic models.

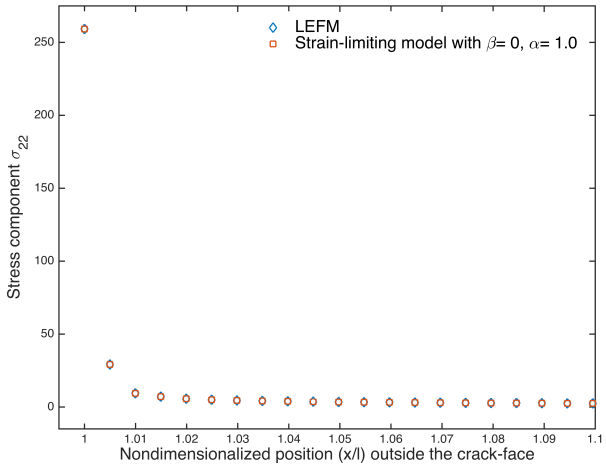

Figure 3.5: Stress component σ_{22} along a line leading up to crack-tip both for LEFM and strain-limiting anisotropic models.

It is clear from Figure 3.4 and 3.5 that the solution to the nonlinear crack problem

with $\beta = 0$ captures the corresponding solution of the linear crack problem and predicts the same stress concentration at the crack-tip as the linearized model. Hence one can recover the classical singular solution as $\beta \to 0$ from the strain-limiting nonlinear models.

Cycle	$\beta = 0.0$	$\beta = 2.0$	$\beta = 10.0$
0	0.000557145	0.000106602	5.4342e-06
1	0.000608284	0.000116602	7.114743e-06
2	0.000622366	0.0001207938	7.8831114e-06
3	0.000628506	0.0001235774	9.122183e-06
4	0.000631589	0.000124788	1.14572e-06
5	0.000633133	0.0001253948	1.171491e-06
6	0.000633905	0.0001256988	1.1823871e-06
7	0.000634292	0.00012584341	1.21945981e-06
8	0.000634485	0.00012584562	1.2414361e-06
9	0.000634582	0.00012584574	1.242891e-06
10	0.000634654	0.00012584574	1.243571e-06
11	0.000634654	0.00012584574	1.243571e-06
12	0.000634654	0.00012584574	1.243571e-06
13	0.000634654	0.00012584574	1.243571e-06

Table 3.2: Convergence of the center node displacement for various limiting stain parameter β across refinement cycles.

Before, we start presenting the results of the numerical simulation of the nonlinear fracture boundary value problem, first we look at the convergence of the center-node

opening displacement (i.e. $u_2(0, 0)$) for various parameters such as β, σ and $\bar{\gamma}_2$. Table 3.2[2] indicates the convergence of the center-node displacement for various limiting-strain parameter across refinements. The other parameters used for computations are $\alpha = 1.0$, $\sigma = 0.001$ and $\bar{\gamma}_2 = 1.0$.

Cycle	$\bar{\gamma}_2 = 0.0$	$\bar{\gamma}_2 = 1.0$	$\bar{\gamma}_2 = 10.0$
0	0.000581406	0.0001106602	4.81513e-05
1	0.00063155	0.0001207938	5.33073e-05
2	0.00064616	0.0001235774	5.46268e-05
3	0.000652708	0.000124788	5.51194e-05
4	0.000655983	0.0001253948	5.5367e-05
5	0.00065762	0.0001256978	5.54911e-05
6	0.000658435	0.0001258488	5.5553e-05
7	0.000658842	0.00012584558	5.55838e-05
8	0.000658855	0.00012584562	5.55866e-05
9	0.000658855	0.00012584574	5.55866e-05
10	0.000658855	0.00012584574	5.55866e-05
11	0.000658855	0.00012584574	5.55866e-05
12	0.000658855	0.00012584574	5.55866e-05
13	0.000658855	0.00012584574	5.55866e-05

Table 3.3: Convergence of the center node displacement for various values of the parameter $\bar{\gamma}_2$ across refinement cycles.

[2]The table depicts the values up to 9-decimal places for the presentation purpose only, the actual numerical-code computes these values using *double precision*.

Table 3.3 show how the center-node displacement i.e. $u_2(0,0)$ converges as the computational domain refined adaptively using *KellyErrorEstimator*[3] class of *deal.II* library. It is clear from Table 3.3 that the solution converges for a fixed value of $\bar{\gamma}_2$ and also decreases with increasing value of $\bar{\gamma}_2$.

Cycle	$\sigma = 0.001$	$\sigma = 0.01$
0	0.0001106602	0.00548815
1	0.0001207938	0.00598835
2	0.0001235774	0.0061249
3	0.000124788	0.00618387
4	0.0001253948	0.00621322
5	0.0001256978	0.00622773
6	0.00012584887	0.00623487
7	0.0001259021	0.0062451197
8	0.00012591142	0.0062452785
9	0.0001259242	0.006245386
10	0.0001259242	0.006245386
11	0.0001259242	0.006245386
12	0.0001259242	0.006245386
13	0.0001259242	0.006245386

Table 3.4: Convergence of the center node displacement for various values top-face tensile loading σ across refinement cycles.

[3]For more information on how to use *KellyErrorEstimator* class in the finite element program please refer to the documentation of *deal.II* library and also video lectures of Professor Bangerth [3].

Table 3.4 shows the convergence of center-node displacement for different top-face tensile load σ. The table clearly indicates the convergence of the solution for each value of σ. The local refinement based adaptive solution algorithm offers distinctive advantage over the global refinement of the computational domain.

3.5.1 Error Reduction Factor

We know that from equation (3.42), the accuracy of the finite element solution depends on the mesh size and it is clear from Figure 3.3 that a very high grid resolution is required in the neighborhood of the crack-tip to adequately capture the variation in the quantities of interest (such as stress and strain). In order to realize the accuracy of the finite element solution, we need to compute the error in the finite element solution as a function of mesh-size[4]. But for the current boundary value problem we don't have exact (solution) displacement field in the body. Hence we define "Error Reduction Factor" (ERF), as a function of number of degrees of freedom, by considering the displacement field obtained from finest mesh (i.e. after last refinement) as an "exact solution". For the problem studied here the ERF is given by:

$$\text{ERF} = \frac{|u_2^{LR}(0,0) - u_2^{i}(0,0)|}{|u_2^{LR}(0,0) - u_2^{i-1}(0,0)|}, \quad i = 2, 3, \ldots LR, \tag{3.46}$$

in which the term $u_2^{LR}(0,0)$ denotes the center-node displacement (y-displacement) at the last-refinement and we compute this quantity as a function of the number of degrees of freedom. The computed quantity, ERF, is approximately 2.0, which is reasonable for the linear finite element used to approximate the quasi-linear elliptic partial differential equation. Figure 3.6 depicts the *log-log* plot of the difference in the

[4]In the case of adaptive finite element method the accuracy of the numerical solution depends on the number of degrees of freedom.

error, which is the difference in the center-node displacement ($u_2(0,\ 0)$) of the current refinement level with the last refinement level. We notice that the error is reduced considerably for the higher values of the modeling parameter β.

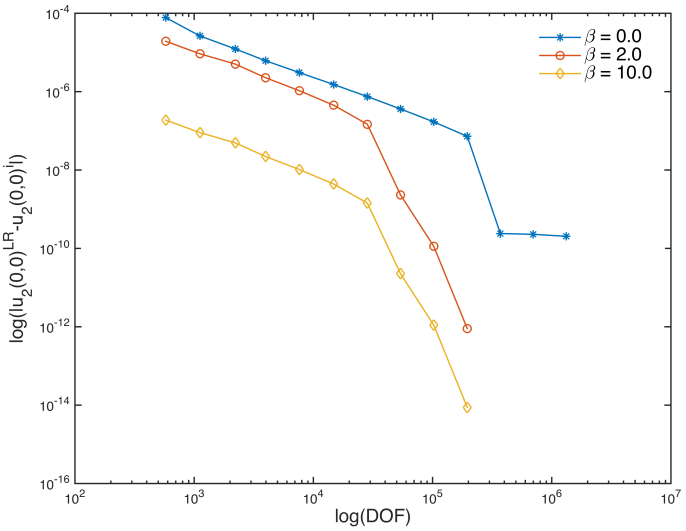

Figure 3.6: The *log-log* plot of the error as a function of the degrees of the freedom.

Figure 3.7a, 3.7b denotes the 2D plots of the displacement components u_1 and u_2 respectively. Both figures, 3.7a and 3.7b, depicts the symmetry boundary conditions. Whereas Figure 3.8 depicts the vector plot of the both displacement components. The vector direction in Figure 3.8 indicates that the displacement is large towards to the top-face compared to the bottom-face.

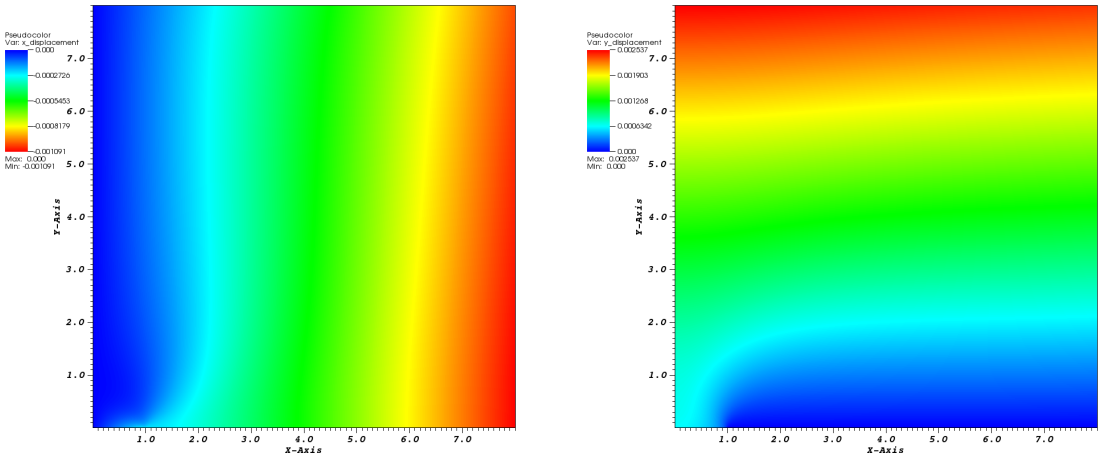

(a) x-displacement (b) y-displacement

Figure 3.7: The displacement vector $\mathbf{u}$ in the entire body for the nonlinear strain-limiting model.

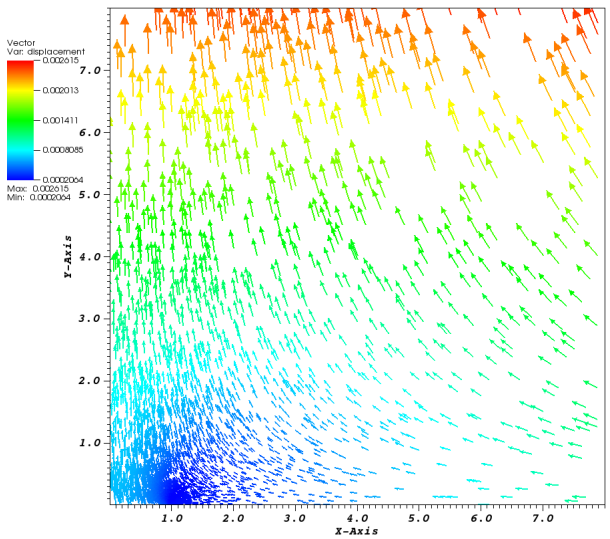

Figure 3.8: The vector plot of the displacement $\mathbf{u}$ for the nonlinear strain-limiting model.

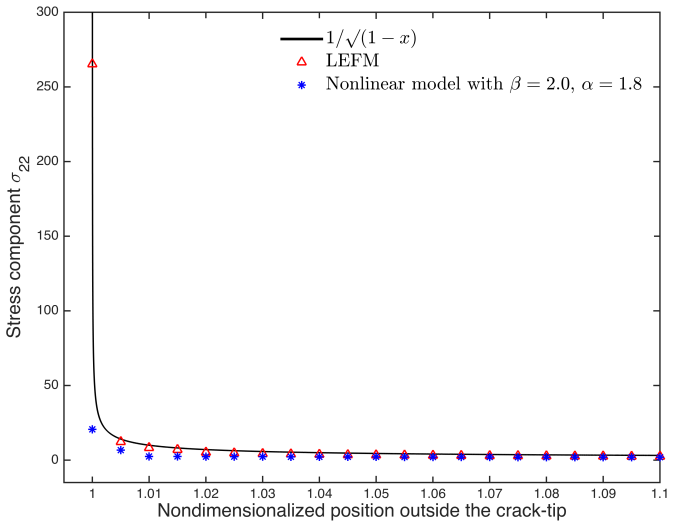

Figure 3.9: Comparison of dimensionless stress component σ_{22}/σ for LEFM and strain-limiting anisotropic model and the axis of the crack was assumed to be along $\boldsymbol{e}_1$.

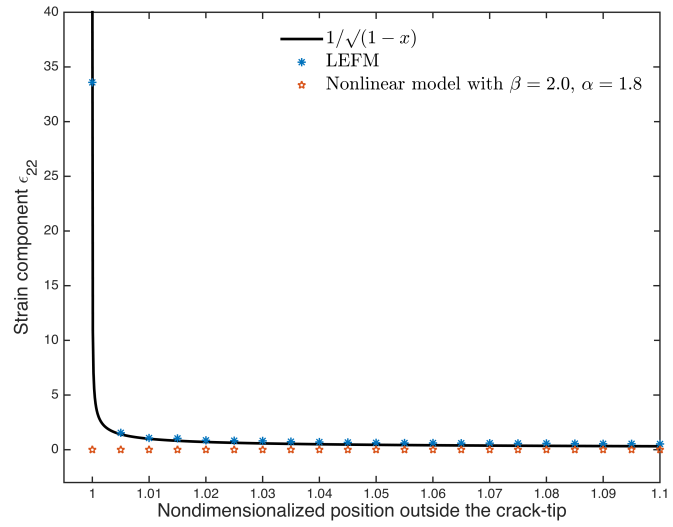

Figure 3.10: Comparison of strain component ϵ_{22} for LEFM and strain-limiting model and the axis of the crack was assumed to be along $\boldsymbol{e}_1$.

Figure 3.9 shows the comparison of the non-dimensional stress component (σ_{22}/σ) for LEFM and nonlinear strain-limiting models. For the nonlinear problem, σ_{22} was computed using the parameter values $\beta = 2.0$, $a = 1.8$. For these computations the axis of the crack was assumed to be along $\boldsymbol{e}_1$. It is clear from the figure that in the case of LEFM the stress component becomes large upon approaching the crack-tip along the radial line ahead of the crack-tip. In addition, our LEFM numerical results predict the same classical singular near-tip stress concentration (i.e. $\frac{1}{\sqrt{1-x}}$), which clearly indicates that our numerical code is correctly capturing the classical singularity. Further, it is clear from the graph that the strain limiting model does not predict the same magnitude of stress concentration near the crack tip as exhibited by the classical LEFM model. The growth of the stress near the crack-tip in the case of nonlinear model is far-slower compared with the reference classical linearized model. Although this is purely a numerical argument and nevertheless the result is consistent with the previous asymptotic study of the pure mode-I problem by Gou et al. [23]. Also, it is important to know that the asymptotic analysis only gives the behavior of the solution as $r \to 0^+$ (where r is the radial distance from the crack-tip). Even working with large density of mesh near the crack-tip, we are only 10^{-4} away from the crack-tip. Therefore we need "very" small mesh-size ($h \ll 10^{-4}$) near the crack-tip to fully resolve about the growth of near-tip stress in the nonlinear model.

Figure 3.10 depicts the comparison of the strain component ϵ_{22} both for LEFM and stain-limiting models. The parameter values used for the computation are same as the values used in the computation for Figure 3.9. As expected the magnitude of ϵ_{22} is much smaller than the predicted value of the classical linearized model. In the case of strain-limiting nonlinear model, ϵ_{22} remains bounded near 0 compared to the unphysical singular prediction of LEFM. The numerical data from the simulation of the classical model are fitted with the curve $\frac{1}{\sqrt{x-1}}$. They both agree very well

up to some accuracy. Figure 3.10 clearly shows the advantage of formulating brittle fracture theory within the context of nonlinear strain-limiting models of elasticity. One can guaranteed to have physically reasonable crack-tip strain and is consistent with the assumption of the starting point of the derivation of the model. Further, another important point to notice that these results are obtained without the use of unphysical crack-edge cohesive zone or the use of extra elements near the crack-tip.

Figure 3.11 is same as in Figure 3.9, except the orientation of the crack-axis is now orthogonal to $\boldsymbol{e}_1$. The parameters used in the computations are $\beta = 2.0$ and $\alpha = 1.8$. Again it is clear from the figure that even very near the crack-tip the value of σ_{22} in the case of nonlinear model is small in magnitude compared with it's counterpart from the classical model.

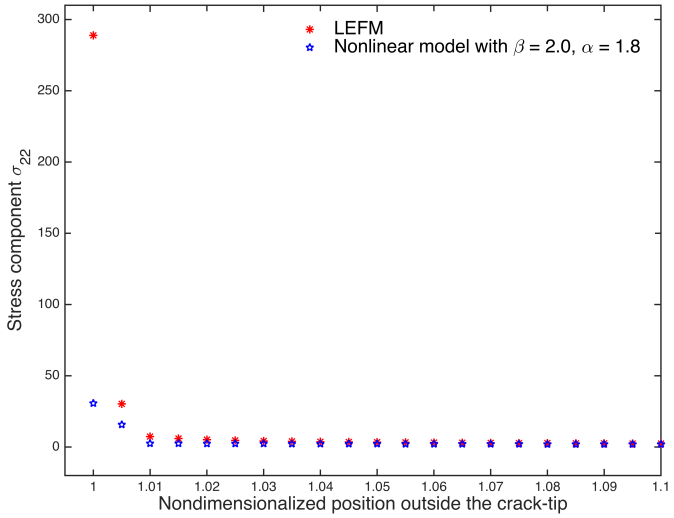

Figure 3.11: Comparison of dimensionless stress component σ_{22}/σ for LEFM and strain-limiting anisotropic model and the axis of the crack was assumed to be along $\boldsymbol{e}_2$.

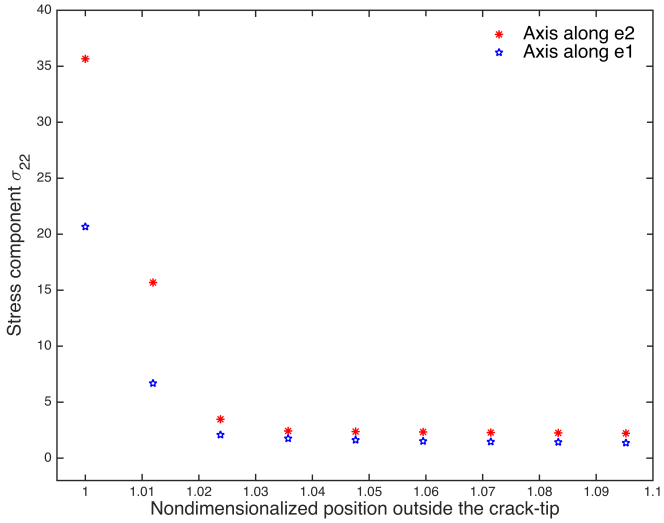

Figure 3.12: Comparison of dimensionless stress component σ_{22}/σ for strain-limiting anisotropic model with the axis of the crack was assumed to be along $\boldsymbol{e}_1$ and orthogonal to $\boldsymbol{e}_1$.

Figure 3.12 indicates that the value of σ_{22} is higher in the case of axis of the crack orthogonal to $\boldsymbol{e}_1$ compared to the same when the axis of the crack assumed along $\boldsymbol{e}_1$. The parameters used in the computation are $\beta = 2.0$, $a = 1.8$, $\sigma = 0.001$.

Figure 3.13 show that both linear and nonlinear stress component σ_{22} agree very well away from the crack-tip for a certain set of parameter values. It is only near the crack tip that the two solutions differ with the linearized elastic solution exhibiting the customary square-root singularity in stress and strain while the strain-limiting solution remains orders of magnitude smaller in stress and strain. For the illustrative purpose the numerical results are shown in Figure 3.13 are along a line $x_1 = 1.0$ and $0 \leq x_2 \leq 8$. The parameters used in the computation are $\beta = 2.0$, $\alpha = 1.8$, $\sigma = 0.001$, $\bar{\gamma}_2 = 1.0$ and the axis of the crack was assumed to be along $\boldsymbol{e}_1$.

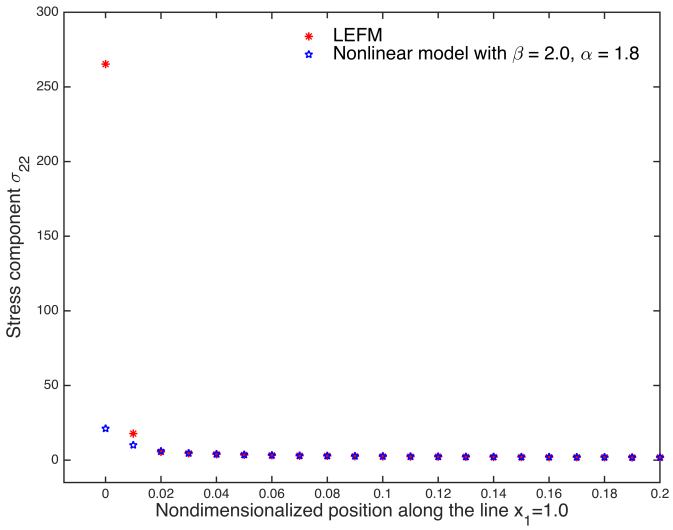

Figure 3.13: Plot of dimensionless σ_{22}/σ along line $x_1 = 1.0$, $0 \leq x_2 \leq 8$ both for LEFM and Strain-Limiting model.

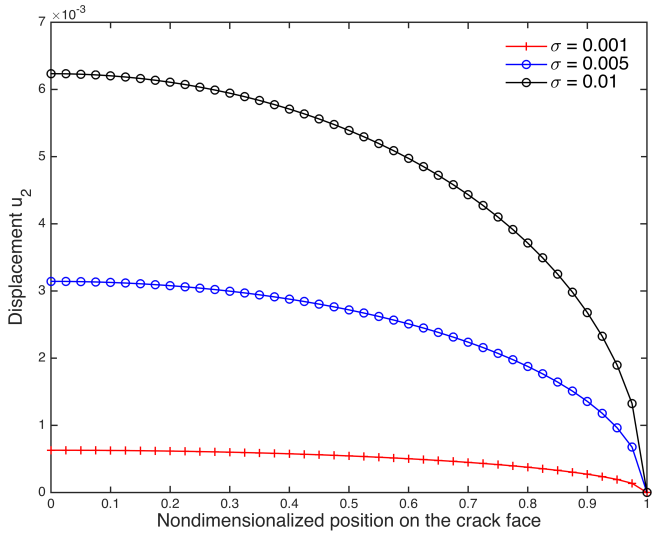

Figure 3.14: Plot of crack-face displacement component u_2 for different top face tensile loading.

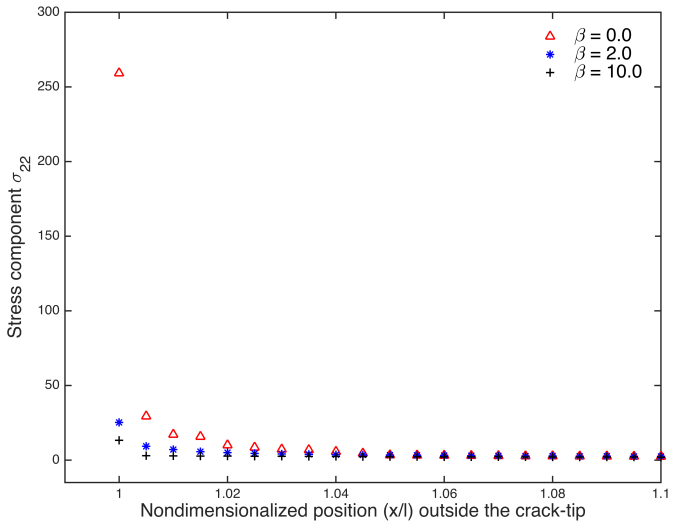

Figure 3.15: Effect of strain-limiting modeling parameter β on the stress component σ_{22} along the line leading up to crack-tip for strain-limiting anisotropic models. The axis of the crack was assumed to be along $\boldsymbol{e}_1$. The parameters used in the computation are $\alpha = 1.8$, $\sigma = 0.001$ and $\bar{\gamma}_2 = 1.0$.

Figure 3.14 shows the effect of the top-face load on the crack-face displacement. It is clear from the plot that the displacement increases with the increasing top-face load. The crack-face displacement is significantly "small" for the nonlinear model compared to the linear model and is indicative of the strain-hardening behavior. For the computations the axis of the crack was assumed to be along $\boldsymbol{e}_1$ and the parameters used are $\beta = 2.0$, $\alpha = 1.8$, $\sigma_S = 0.001$ and $\bar{\gamma}_2 = 1.0$.

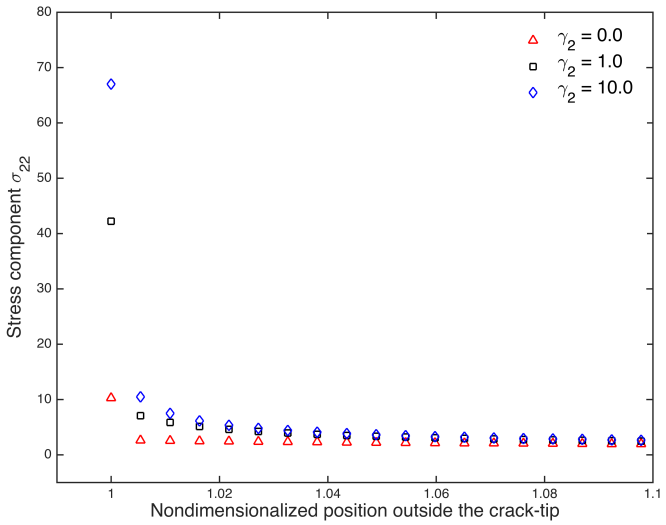

Figure 3.16: Effect of $\bar{\gamma}_2$ on the stress component σ_{22} along the line leading up to crack-tip for strain-limiting anisotropic model. The axis of the crack was assumed to be along $\boldsymbol{e}_2$.

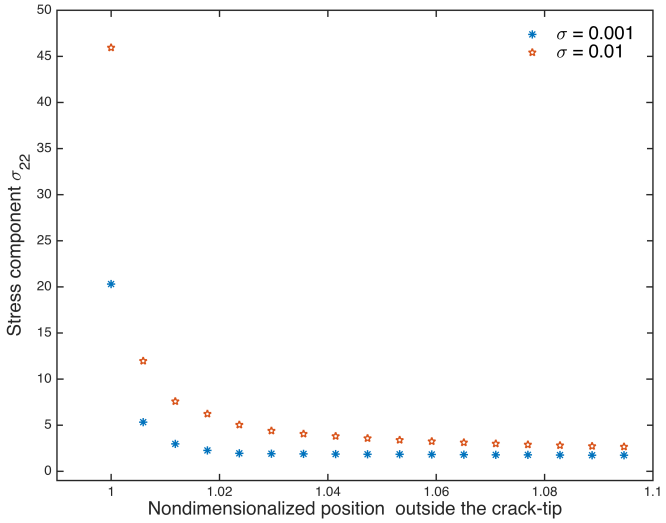

Figure 3.17: Effect of top-face tensile load σ on the stress component σ_{22} along the line leading up to crack-tip for the strain-limiting anisotropic model. The axis of the crack was assumed to be along $\boldsymbol{e}_1$.

Figure 3.15 shows the non-dimensional stress component (σ_{22}/σ) along the bottom face leading up to the crack-tip for increasing values of the strain-limiting parameter β. When $\beta \gg 1$ the crack-tip stresses significantly less than that when $\beta < 1$ (such as $\beta = 0.5$). With the value $\beta = 0.0$ one can recover the classical crack-tip stress behavior and also the bounded crack-tip stress and strain results obtained using the nonlinear models without the use of extra-elements (or *cohesive law*) in the crack-tip neighborhood.

Figure 3.16 indicates the effect of $\bar{\gamma}_2$ on the nonlinear σ_{22} along the line ahead of the crack-tip. The graph shows that the crack-tip σ_{22} increases with the increasing value of $\bar{\gamma}_2$. The parameters used in the computation are $\beta = 2.0$, $\alpha = 1.8$, $\sigma = 0.001$. In Figure 3.17 a plot is presented showing the effect of the top-face load on the crack-tip stress. The figure clearly indicates that the value of crack-tip σ_{22} increases with the increasing top-face loading. Again, the parameters used in the computation are same as the ones used in Figure 3.16.

Figure 3.18 shows the convergence of the crack-opening displacement $u_2(x_1, 0)$ as the computational mesh is refined. The local refinement criterion used in our program introduces more and more active cells in the neighborhood of the crack-tip. Various parameters along with the crack-axis orientation used in the computation are same as those used in the computation for Figure 3.15. This figure strongly indicates the convergence of the solution in our finite element algorithm.

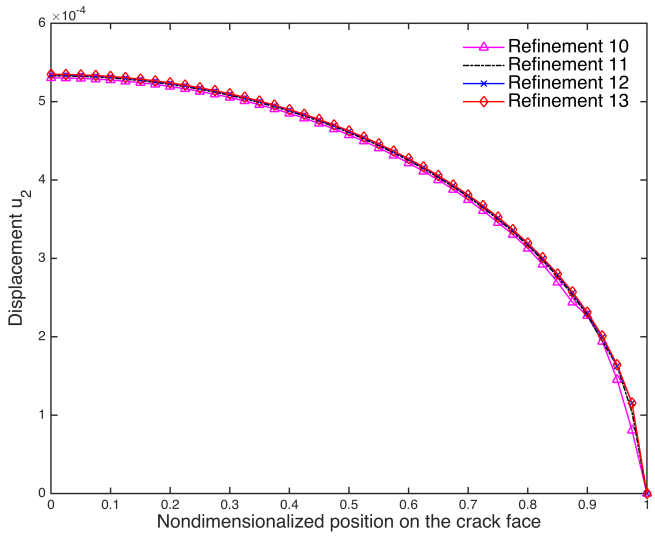

Figure 3.18: Convergence of the crack-face opening displacement $u_2(x_1, 0)$ for various adaptive refinements of the domain.

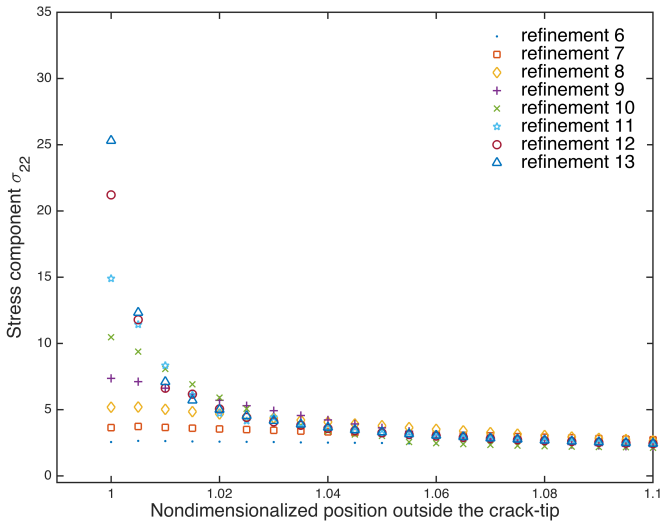

Figure 3.19: Dimensionless near-tip stress component σ_{22}/σ for various adaptive refinements of the domain.

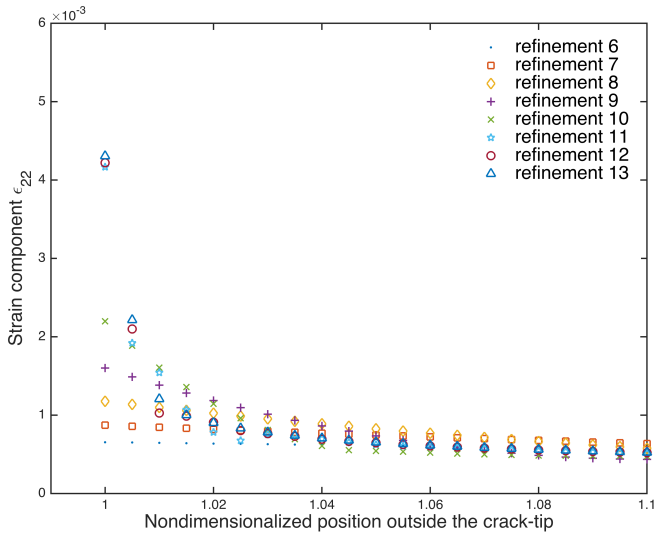

Figure 3.20: Near-tip strain component ϵ_{22} for various adaptive refinements of the domain.

Figures 3.19 and 3.20 shows the near-tip stress-strain values for various adaptive refinement levels of the domain. In Figure 3.20, an important trend in the convergence of strain component ϵ_{22} can be observed, unfortunately the stress component in figure 3.19 doesn't shows the similar convergence trend. But the obtained numerical results indicate that, even very near (with the finer mesh), the mathematical crack-tip, both stress and strain remains orders of magnitude smaller compared with the respective values predicted by the classical model.

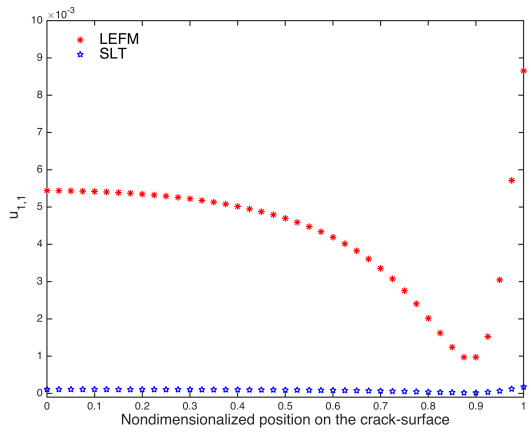

(a) $u_{1,1}$ behind the crack-tip

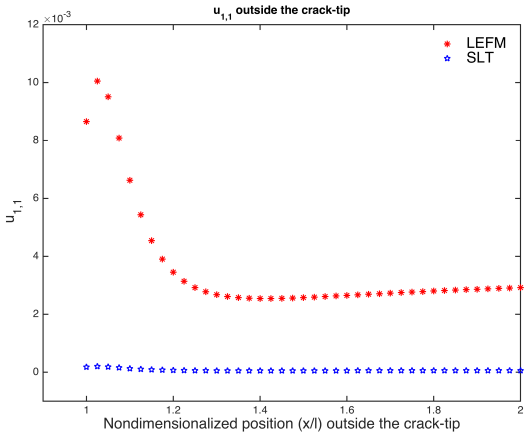

(b) $u_{1,1}$ in-front of the crack-tip

Figure 3.21: $u_{1,1}$ along line leading up to the crack-tip.

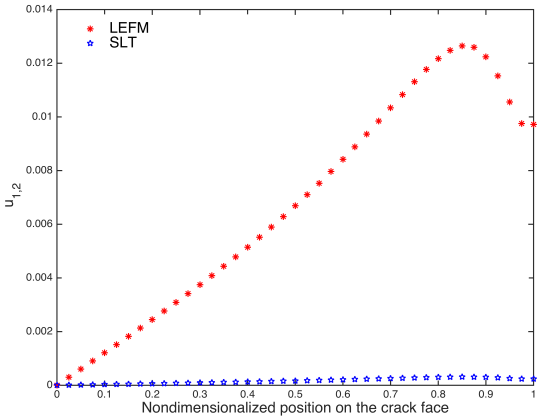

(a) $u_{1,2}$ behind the crack-tip

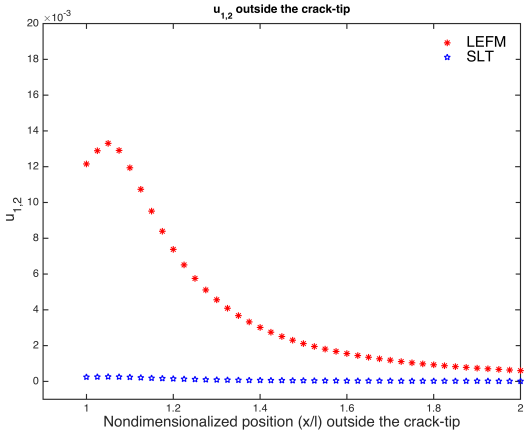

(b) $u_{1,2}$ in-front of the crack-tip

Figure 3.22: $u_{1,2}$ along line leading up to the crack-tip.

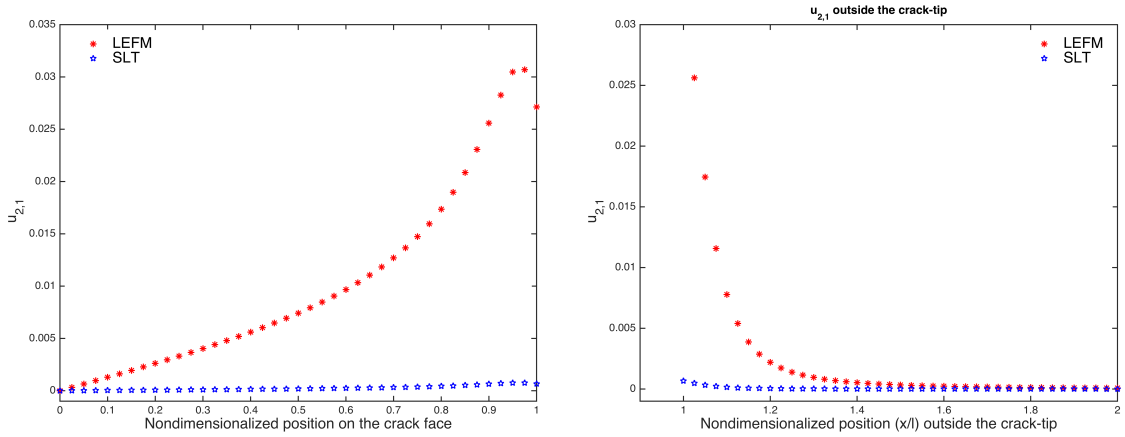

(a) $u_{2,1}$ behind the crack-tip (b) $u_{2,1}$ in-front of the crack-tip

Figure 3.23: $u_{2,1}$ along line leading up to the crack-tip.

Figures 3.21, 3.22 and 3.23 indicates the comparison of the partial derivatives of u_1 and u_2 both in the case of linear and nonlinear problems. In each case, we see that the near-tip value in the nonlinear model never become close the value from the linear problem.

3.6 Behavior of Cleavage Stress Near the Crack-Tip

The results presented in this chapter for the strain limiting model (and also in [41] and [23]) show that stresses and strains predicted by the strain limiting model are much smaller than those predicted by the LEFM model. Of course numerical simulations can never prove bounded stresses in the neighborhood of the crack-tip. However, through increasing mesh refinement one can get increasingly more reliable stress estimates to within microns of a physical crack-tip. The simulations performed to date suggest that for a centimeter long crack, the level of refinements implemented resolve the stresses to within a micron of the crack-tip, and show those predicted by the strain limiting model are one to two orders of magnitude smaller than those predicted by LEFM.

Since strains remain bounded by constitutive assumption in the limiting strain model, the crack tip cannot be a singular sink of energy unless stresses blow up much faster upon approaching the crack-tip than the LEFM solution. Assuming that the crack-tip is not a singular sink for the limiting strain model, then the classical fracture criteria used in LEFM that are based upon the singular energy sink nature of the crack-tip do not apply for the strain limiting model. Therefore One needs to develop a local fracture criterion within the class of strain-limiting elasticity models. To this end, the behavior of the cleavage stress in the neighborhood of crack-tip offers an alternative criterion and is relatively easy to implement.

In this section, we are interested in studying the behavior of the crack-tip cleavage stress for the nonlinear models. The same was also discussed in the paper of Sendova and Walton [47] for pure mode-I problem. For the plane-strain fracture on hand, we study the behavior of the cleavage stress in the neighborhood of the crack-tip. The expression for the cleavage stress is given by

$$\sigma_{\theta\theta} = \sigma_{11} \sin^2\theta + \sigma_{22} \cos^2\theta - \sigma_{12} \sin 2\theta, \tag{3.47}$$

in which θ is the polar angle. To numerically evaluate $\sigma_{\theta\theta}$, we consider a quadrant of a circle in front of crack-tip with crack-tip as the center and radius (r) 1 unit. We then estimated $\sigma_{\theta\theta}$ using (3.47) for an array of values of $\theta \in [0, \pi/2]$ and $r \in [0, 1]$ ($r \to 0^+$ is the crack-tip). We have chosen 50 equally spaced data points in $r-$ and 90 equally spaced points in $\theta-$direction and then computed the value of $\sigma_{\theta\theta}$ for each value of r and in each θ direction.

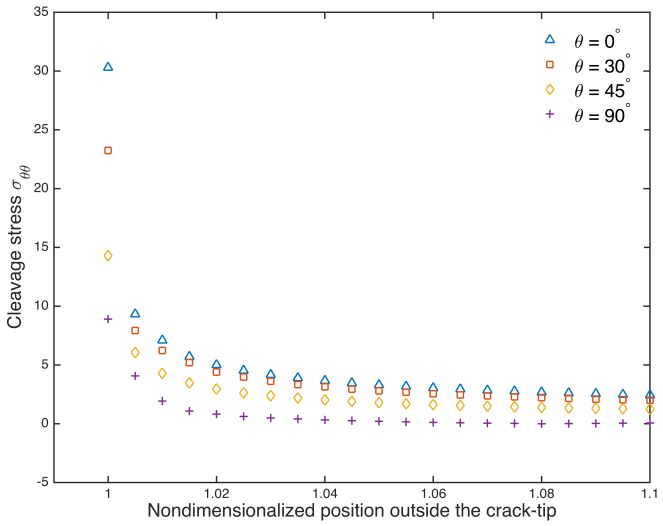

Figure 3.24: Plot of dimensionless cleavage stress $\sigma_{\theta\theta}$ along the line leading up to crack-tip for strain-limiting anisotropic model.

The computed numerical values of $\sigma_{\theta\theta}$, for a certain set of parameter values and a particular orientation of the crack, yields $\sigma_{\theta\theta}$ as a monotonically decreasing function of θ. Of all the computed values of $\sigma_{\theta\theta}$ using the relation (3.47), we noticed that the maximum occurs at $\theta = 0.0$.

Figure 3.24 depicts cleavage stress $\sigma_{\theta\theta}(r, \theta)$ for the different values of θ. In the numerical computations, we have used the parameter values such as $\beta = 2.0$, $a = 1.8$, $\sigma = 0.001$ and $\bar{\gamma}_2 = 1.0$ and the axis of the crack was assumed to be along $\boldsymbol{e}_1$ direction. It is clear from the plot that the numerical value of the cleavage stress is large when $\theta = 0$ compared to the all other values of θ. This result is in agreement with the classical linearized solution for pure mode I loading.

3.7 Conclusions

In this chapter, we have presented a computational model for the plane-strain fracture using nonlinear strain-limiting response relations. The bulk constitutive model

is a nonlinear relationship between the classical linearized strain and the Cauchy stress tensors. One will not lead to such nonlinear relationship from the linearization process within the context of classical elasticity. Also the models introduced by [34] have a distinctive advantage over classical models, in that the strains are guaranteed to be bounded in the neighborhood of a sharp crack or re-entrant corner even if the stress becomes "large". To this end, the main aim of this study whether or not the strain-limiting models predicts the classical stress singularity.

In this chapter, we have laid out an approach for implementing a conforming finite element algorithm to the solution of nonlinear fracture boundary value problem. The numerical results presented in this chapter indicate that even very near the crack-tip, both stress and strain remain much smaller in magnitude than the corresponding predictions from LEFM. The numerical results outlined in this chapter supports the asymptotic near-tip stress-strain behavior presented in the previous chapter and also in the work of Gou et al. [23]. Further, we have demonstrated numerically that the solution to the nonlinear crack problem do tend to the general solution to reference linearized model as $\beta \to 0$. When $\beta = 0$, the current model predict the same singular stress-strain concentration in the neighborhood of the crack-tip.

The nonlinear fracture model studied here doesn't predict the same singular crack-tip stress concentration, hence a fracture criterion based on the crack-tip Stress Intensity Factor (SIF) or local Energy Release Rate (ERR) is not available. Therefore for a *possible* local fracture criteria, we here implement *Critical Crack-Tip Stress (CCTS)* criterion as described by Sendova and Walton in [47]. To that end, we have studied the behavior of the cleavage stress component $\sigma_{\theta\theta}$ in a quadrant of circle with crack-tip as the center. The numerical results obtained indicates that $\sigma_{\theta\theta}$ is a monotonically decreasing function of θ with the maximum occurs when $\theta = 0$, which is in agreement with the classical LEFM solution for the pure mode-I loading.

4. A NONLOCAL FINITE ELEMENT FORMULATION OF MODE-III FRACTURE WITH SURFACE TENSION EXCESS PROPERTY*

In this chapter we study a stable nonlocal finite element implementation of an anti-plane strain mode-III[2] fracture incorporating the effects of crack-surface interfacial mechanics. The problem studied in this chapter is quasi-static and we assume no crack growth due to loading or breaking of atomic bonds. The issue addressed in this chapter is on implementing the the brittle fracture theory with surface tension excess property using stable numerical methods such as finite elements. The main emphasis is on the reformulation of the jump momentum balance boundary condition due to its inclusion of higher order tangential derivatives of the displacement.

4.1 Mode-III Fracture Problem Formulation

We consider a two-dimensional (2D) infinite, homogeneous, isotropic, linearly elastic plate Ω under far-field antiplane shear loading σ_{23}^{∞} with a straight crack Ω of length $2l$, as shown in Figure 4.1. The symbol $\otimes$ in Figure 4.1 indicate that the forces acting in the direction of outside of the plane of the paper and the symbol $\odot$ shows the direction of forces into the plane.

The assumption of anti-plane shear loading is characterized by the non-zero out of plane displacement $u_3(X_1, X_2)$ which only depend upon in-plane coordinates and is anti-symmetric about the x_2 axis. The displacements in the X, Y and Z directions

*Part of this chapter is reprinted with permission from Springer publications, "Numerical simulation of mode-III fracture incorporating interfacial mechanics" by L. A. Ferguson, M. Muddamallappa, J. R. Walton, *International Journal of Fracture*, 192(1), 47-56, 2015; Copyright 2015 by Springer Publications.

[2]Mode-III or tearing mode crack is one in which shear stress acting parallel to the plane of the crack and parallel to the crack-front.

are given by:

$$u_1(X_1, X_2) = u_2(X_1, X_2) = 0, \quad u_3(X_1, -X_2) = -u_3(X_1, X_2). \tag{4.1}$$

The only non-vanishing and independent components of the stress tensor $\boldsymbol{\sigma}$ are τ_{13} (which is anti-symmetric) and τ_{23} (which is symmetric) and the corresponding components of strain tensor $\boldsymbol{\epsilon}$ are ϵ_{13} and ϵ_{23}. We also nondimensionlize the space variables by the half-length of the crack (l) and stresses by the reference shear modulus (μ).

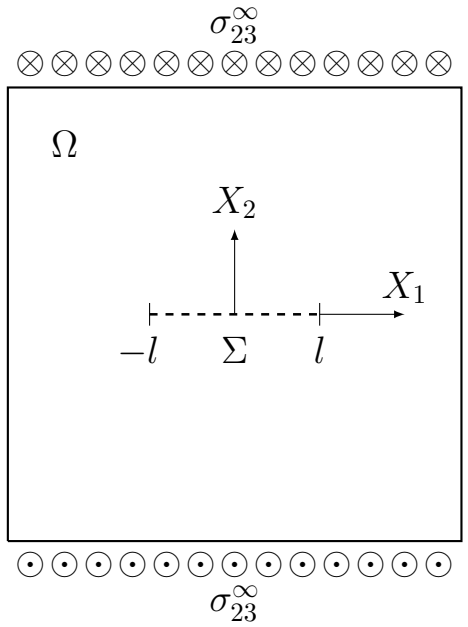

Figure 4.1: Physical configuration consisting of linear elastic plane Ω under antiplane shear loading with a crack of length $2l$.

4.2 Governing Equations

The differential momentum balance (DMB) yields the usual equilibrium equation for the classical linearized model, given by

$$\Delta u_3 + b_f = 0 \quad \text{in} \quad \Omega, \tag{4.2}$$

in which b_f is the body force term. For the case of antiplane shear, the only nonzero stress components are τ_{13} and τ_{23} and by the constitutive Hooke's law are given by

$$\tau_{13} = \frac{\partial u_3}{\partial x_1}, \tag{4.3}$$

$$\tau_{23} = \frac{\partial u_3}{\partial x_2}. \tag{4.4}$$

The symmetry in the displacement and stresses about x and y axes allow one to reduce the problem to the upper right quadrant. Therefore the resulting finite computational domain Q is the square $[0, b] \times [0, b]$ as shown in Figure 4.2. We need to take b sufficiently large to approximate the infinite problem. Also $\Gamma_0 = [0, 1] \times \{0^+\}$ represents the upper-right crack-face.

Since the DMB derived here is a linear, we use superposition principle to move the top-face solution which has the fixed loading σ_{23}^{∞} and combine with the solution on the crack-face. This means that the far-field loading σ_{23}^{∞} is now being applied to the crack-face.

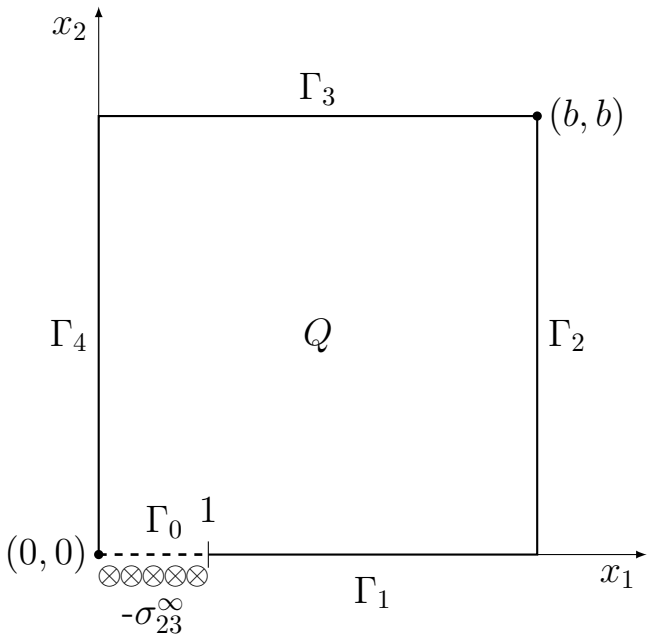

Figure 4.2: 2D finite computational domain Q with Γ_0 indicating the mode-III upper-right crack face.

4.3 Boundary Conditions

After the superposition, since the top-face load has been moved to the crack-surface, the top edge Γ_3 is traction-free i.e.

$$\nabla u_3 \cdot \mathbf{n} = 0, \tag{4.5}$$

where $\mathbf{n}$ is the unit outward normal. The right edge Γ_2 and left edge Γ_4 were also kept traction free, therefore same boundary condition (4.5) apply on these parts. Moreover, symmetry demands that the out-of-plane displacement component $u_3(x_1, 0)$ vanishes along the line ahead of the crack-tip, i.e.

$$u_3(x_1, 0) = 0, \quad \text{on} \quad \Gamma_1 \ . \tag{4.6}$$

Then significant difference between LEFM and the theory developed by Sendova and Walton in [47] occurs at the crack-surface. The interface is modeled as a *dividing surface* endowed with excess property such as surface tension. For the current anti-plane shear fracture model, we assume that the surface tension depends linearly on the curvature of the out of plane displacement of the fracture surface as

$$\tilde{\gamma} = \gamma_0 + \gamma_1 u_{3,11}(x_1, 0)\,. \tag{4.7}$$

Then the resulting jump momentum balance equation together with the superposed far-field load gives the following boundary condition over the crack-surface

$$\tau_{23}(x_1, 0) = -\gamma_1\, u_{3,111}(x_1, 0) - \sigma_{23}^{\infty}\ . \tag{4.8}$$

In (4.7) the term $(\cdot)_{,11}$ is the second order derivative in tangential direction and γ_0, γ_1 are the surface tension constants. Also note that the surface tension $\tilde{\gamma}$ and the parameters γ_0, γ_1 defined in (4.7) are all in the non-dimensional form.

4.4 Weak Formulation

To derive the weak formulation for the problem on hand we recall the resulting boundary value problem from the previous section

$$\Delta u_3 + b_f = 0 \quad \text{in} \quad Q, \tag{4.9}$$

$$\nabla u_3 \cdot \mathbf{n} = 0, \quad \text{on} \quad \Gamma_2,\ \Gamma_3,\ \Gamma_4 \tag{4.10}$$

$$u_3(x_1, 0) = 0 \quad \text{on} \quad \Gamma_1, \tag{4.11}$$

$$\tau_{23}(x_1, 0) = -\gamma_1\, u_{3,111}(x_1, 0) - \sigma_{23}^{\infty} \quad \text{on} \quad \Gamma_0\ . \tag{4.12}$$

In [47] Sendova and Walton showed that for the pure mode-I problem, when the surface tension is assumed to depend linearly on the crack-surface mean curvature (same as (4.7)), the crack-tip stresses are bounded and the crack-opening displacement takes the cusp shape at the crack-tip. They have derived a singular integrodifferential equation for the upper crack-face opening displacement on $|X_1| < 1$ from the jump momentum balance boundary conditions and the Dirichlet-to-Neumann and Neumann-to-Dirichlet maps (equations (14) and (15) in [47]). The singular integrodifferential equation was then analyzed through regularization to a second-kind Fredholm integral equation and proved that it has a unique solution (continuous not singular) for all, apart from countably many, values of the surface tension parameters γ_0 and γ_1. For the mode-III fracture BVP (4.9)-(4.12), we will use[3] the regularization approach to show that this BVP has a unique continuous solution (and hence non-singular) with bounded stresses and strains at the crack-tip. Therefore the boundary condition (4.12) is well defined even though it contains higher-order tangential derivatives than the bulk PDE (4.9).

Next to derive a weak formulation, we multiply the DMB (4.9) by a scalar test function v and integrate over the domain Q. Using integration by parts and boundary conditions (4.10)-(4.12) yields

$$\int_Q \nabla u_3 \cdot \nabla v - \int_{\partial Q} v \, \nabla u_3 \cdot \mathbf{n} = \int_Q v \, b_f \, . \tag{4.13}$$

There is no contribution from the second term on the left-hand side of (4.13) except over the crack surface. Therefore the resulting weak formulation takes the form

$$\int_Q \nabla u_3 \cdot \nabla v - \int_{\Gamma_0} v \, \tau_{23}^C(x_1, 0) = \int_Q v \, b_f \, , \tag{4.14}$$

[3]An outline of the proof is given in the section 4.7.

where the symbol $\tau_{23}^{C}(x_1, 0)$ is the JMB condition (4.12). We cannot substitute the boundary condition (4.12) into (4.14) directly since it results in a weak form with higher-order tangential derivatives that cannot be eliminated by integration by parts. Therefore the issue on hand is how to implement the boundary condition (4.12) into a numerically stable finite element formulation of the BVP. To this end, we will reformulate the boundary condition (4.12) using boundary Green's function and Hilbert's transform (Dirichlet to Neumann map).

4.5 Reformulation of the Crack-Face Boundary Condition

We consider the JMB crack surface boundary condition (4.12) and rearrange the equation to obtain

$$-u_{3,111}(x_1, 0) = \frac{1}{\gamma_1} \left[u_{3,2}(x_1, 0) + \sigma_{23}^{\infty} \right] \quad \text{on} \quad \Gamma_0 \, . \tag{4.15}$$

This can be viewed as a second-order ordinary differential equation (ODE) for $u_{3,1}$ over the interval $[0, 1]$. Hence we rewrite the above equation (4.15) as:

$$\mathcal{L}\{u_{3,1}\} = \frac{1}{\gamma_1} \left[u_{3,2}(x_1, 0) + \sigma_{23}^{\infty} \right], \tag{4.16}$$

where $\mathcal{L}\{\cdot\}$ denotes the second order, linear differential operator

$$\mathcal{L}\{y\}(x) := -\, y''(x) \, . \tag{4.17}$$

In order to complete the boundary value problem for $u_{3,1}$, we need two boundary conditions, to this end we note that the out-of-plane displacement component $u_3(x_1, x_2)$ is

an odd function in x_2, therefore $u_{3,1}(x_1, x_2)$ required to satisfy the boundary condition

$$u_{3,1}(0,0) = 0\,, \tag{4.18}$$

also the regularization on $\Gamma_0 \cup \Gamma_1$ implies that the slope of the crack-opening profile $u_{3,1}(x_1, 0)$ is continuous at the crack-tip i.e.

$$u_{3,1}(1,0) = 0\,. \tag{4.19}$$

Note that the boundary condition (4.19) is similar to equation $(29)_1$ in [47]. Finally combining (4.17), (4.18) and (4.19), we have the following two-point boundary value problem.

Definition 1. *Find* $y(x) := u_{3,1}(x, 0)$ *solving*

$$\begin{cases} \mathcal{L}\{y\}(x) = f(x), \quad 0 < x < 1 & \text{(4.20a)} \\ \qquad y(0) = 0, & \\ \qquad y(1) = 0, & \text{(4.20b)} \end{cases}$$

where $\mathcal{L}\{\cdot\}$ *is the second-order, linear differential operator defined in (4.17) and the right-hand-side function is given by*

$$f(x) = \frac{1}{\gamma_1}[u_{3,2}(x, 0) + \sigma_{23}^{\infty}]. \tag{4.21}$$

Then the Green's function $G(x, q)$ for the operator (4.17) can be computed by considering the homogeneous equation

$$0 = \mathcal{L}\{y\}(x) = -y''(x)\,, \tag{4.22}$$

and choose two solutions satisfying the boundary conditions (4.20b)

$$\begin{array}{ll} y_1(x) := x & \\ & \Longrightarrow \quad y_1(0) = 0, \\ y_2(x) := 1 - x & \quad\quad\; y_2(1) = 0. \end{array} \tag{4.23}$$

The corresponding Wronskian is

$$W(y_1, y_2)(q) = y_1(q)y_2'(q) - y_1'(q)y_2(q) \tag{4.24}$$

$$= -1. \tag{4.25}$$

Thus the Green's function is given by

$$G(x,q) = \begin{cases} -q(1-x), & 0 \le q \le x \le 1, \\ -x(1-q), & 0 \le x \le q \le 1. \end{cases} \tag{4.26}$$

Also note that

$$\int_0^1 G(x,q)\, dq = -\frac{x}{2}(1-x). \tag{4.27}$$

Then the solution to the two point boundary value problem defined in (4.20a) and (4.20b) is given by

$$u_{3,1}(x,0) = y(x) = \mathcal{G}\{f\}(x) := \int_0^1 G(x,q) f(q) dq. \tag{4.28}$$

Using (4.21) in (4.28) yields

$$\begin{aligned} u_{3,1}(x,0) &= \frac{1}{\gamma_1}\int_0^1 G(x,q)[u_{3,2}(q,0)+\sigma_{23}^{\infty}]\,dq \\ &= \frac{1}{\gamma_1}\int_0^1 G(x,q)\,u_{3,2}(q,0)\,dq - \frac{\sigma_{23}^{\infty}}{2\gamma_1}\,x(1-x). \end{aligned} \tag{4.29}$$

Now recall that the Hilbert transform gives the Dirichlet-to-Neumann map

$$u_{3,2}(x,0^+) = \mathcal{H}\{u_{3,1}\} \tag{4.30}$$

$$= \frac{1}{\pi}\fint_{-\infty}^{\infty} u_{3,1}(q,0^+)\,\frac{dq}{q-x} \tag{4.31}$$

$$= \frac{1}{\pi}\fint_0^1 u_{3,1}(q,0^+)\,\frac{2q}{q^2-x^2}\,dq, \tag{4.32}$$

since $u_{3,1}(x,0)$ is odd and u_3 vanishes outside the crack surface. In (4.30) the symbol $\mathcal{H}$ denotes the Hilbert transform, also $\fint$ denotes a Cauchy principal value. Applying the BVP solution (4.29) to this equation yields

$$\begin{aligned} u_{3,2}(x,0^+) =& \frac{1}{\pi\gamma_1}\fint_0^1\int_0^1 G(q,r)\,u_{3,2}(r,0)\,dr\,\frac{2q}{q^2-x^2}\,dq \\ &- \frac{\sigma_{23}^{\infty}}{2\pi\gamma_1}\fint_0^1 q(1-q)\,\frac{2q}{q^2-x^2}\,dq. \end{aligned} \tag{4.33}$$

We now need to simplify the two terms in the above equation (4.33). To this end we observe that since the Green's function is smooth, we change the order of integration in the double integral term and swap dummy variables. For the notational simplification,

we denote the first term by $h(x)$ and the second term by $g(x)$.

$$\begin{aligned} h(x) &:= \int\!\!\!\!\!\!-_0^1 \int_0^1 G(r,q)\, u_{3,2}(q,0)\, dq\, \frac{2r}{r^2-x^2}\, dr \\ &= \int_0^1 u_{3,2}(q,0) \int\!\!\!\!\!\!-_0^1 G(r,q)\, \frac{2r}{r^2-x^2}\, dr\, dq \\ &= \int_0^1 k(x,q)\, u_{3,2}(q,0)\, dq, \end{aligned} \tag{4.34}$$

where the inner integral simplifies to

$$\begin{aligned} k(x,q) &:= \int\!\!\!\!\!\!-_0^1 G(r,q)\, \frac{2r}{r^2-x^2}\, dr \\ &= \int_0^q -r(1-q)\left[\frac{1}{r+x}+\frac{1}{r-x}\right] dr + \int_q^1 -q(1-r)\left[\frac{1}{r+x}+\frac{1}{r-x}\right] dr \\ &= -(1-q)\left[2\int_0^q dr - x\int_0^q \frac{dr}{r+x} + x\int_0^q \frac{dr}{r-x}\right] \\ &\qquad + q\left[2\int_q^1 dr - (x+1)\int_q^1 \frac{dr}{r+x} + (x-1)\int_q^1 \frac{dr}{r-x}\right] \\ &= (q+x)\ln(q+x) + (q-x)\ln|q-x| - q(1+x)\ln(1+x) - q(1-x)\ln|1-x| \end{aligned} \tag{4.35}$$

The second integral term in (4.33) simplifies as

$$\begin{aligned} g(x) &:= \int_0^1 \frac{q(1-q)}{q+x}\, dq + \int_0^1 \frac{q(1-q)}{q-x}\, dq \\ &= \int_0^1 (1-q+x)\, dq - x(1+x)\int_0^1 \frac{1}{q+x}\, dq + \int_0^1 (1-q-x)\, dq + x(1-x)\int_0^1 \frac{1}{q-x}\, dq \\ &= 1 - x(1+x)\ln\left(\frac{1+x}{x}\right) + x(1-x)\ln\left|\frac{1-x}{x}\right|. \end{aligned} \tag{4.36}$$

Apply these results to (4.33) yields the reformulated JMB condition

$$\tau_{23}^C(x_1,0) := u_{3,2}^C(x,0) = \frac{1}{\pi\gamma_1}\int_0^1 k(x,q)\, u_{3,2}(q,0)\, dq - \frac{\sigma_{23}^\infty}{2\pi\gamma_1}\, g(x), \quad \text{on } \Gamma_C, \tag{4.37}$$

where $k(x,q)$ and $g(x)$ are given in (4.35) and (4.36), respectively. Applying this result to (4.14) yields the final weak form

$$\int_Q \nabla u_3 \cdot \nabla v + \frac{1}{\pi\gamma_1} \int_0^1 v(x,0) \int_0^1 k(x,q)\, u_{3,2}(q,0)\, dq\, dx = \int_Q v\, b_f + \frac{\sigma_{23}^{\infty}}{2\pi\gamma_1} \int_0^1 v(x,0)\, g(x)\, dx. \tag{4.38}$$

Note that this weak form has no higher-order derivatives, thus the standard FEM can now be applied. Specifically, we will solve the following.

Definition 2. *Find $u \in V$ such that*

$$a(u,v) = L(v), \quad \forall \ \ v \in V, \tag{4.39}$$

where $a(\cdot,\cdot)$ and $L(\cdot)$ are the bilinear and linear forms, respectively, given by

$$a(u,v) = \int_Q \nabla u \cdot \nabla v + \int_0^1 v(x,0) \int_0^1 K(x,q)\, \frac{\partial}{\partial y} u(q,y) \Big|_{y=0} dq\, dx, \tag{4.40}$$

$$L(v) = \int_Q v b_3 + \int_0^1 v(x,0)\, G(x)\, dx, \tag{4.41}$$

where the kernel K is given by

$$K(x,q) = \frac{1}{\pi\gamma_1}\, k(x,q), \tag{4.42}$$

$G(x)$ is given by

$$G(x) = \frac{\sigma_{23}^{\infty}}{2\pi\gamma_1}\, g(x), \tag{4.43}$$

and V is the solution and test space given by

$$V = \left\{ w(\mathbf{x}) \in H^1(Q) : \ \ w \Big|_{\Gamma_1} = 0 \right\}. \tag{4.44}$$

4.6 Numerical Implementation

For the numerical implementation of the derived model, we have used two different approaches for solving this problem using finite elements. In the first, we solve the Fredholm second type integral equation which defines the reformulated JMB condition (4.37) to obtain a numerical approximation to the Neumann boundary condition for $u_{3,2}(x,0)$ over the crack surface. Then the result can be directly applied to the original weak formulation with standard finite elements. In the second method, we solve the variational problem given in Definition 2 using a standard FEM approach, with the reformulated JMB condition included directly. We will describe these methods in more detail. In Section 4.8, we will show that both the methods are in good agreement. For the numerical implementation, we have developed the numerical code using the deal.II library [5, 6].

4.6.1 Fredholm Approximation Approach

We consider the original weak form (in the absence of body forces)

$$\int_Q \nabla u_3 \cdot \nabla v + \int_{\Gamma_C} v\, u^C_{3,2} = 0, \tag{4.45}$$

where $u^C_{3,2}(x,0)$ solves the Fredholm second kind integral equation of the second kind

$$u(x) - \int_0^1 K(x,q)\, u(q)\, dq = -G(x), \quad \text{for } 0 \le x \le 1, \tag{4.46}$$

(cf. (4.37)) where $K(x,q)$ and $G(x)$ are given in (4.42) and (4.43), respectively. For the FEM implementation of this weak form, we assemble the system using Gaussian quadrature to approximate the integrals. In this case, all we require is the value of $u^C_{3,2}$ at the quadrature points. To obtain these values, we have developed an algorithm for

numerically solving the Fredholm integral equation above. We use composite Simpson's rule to approximate the integral term, i.e.,

$$\int_0^1 K(x,q)u(q)\,dq \approx \sum_{j=0}^{n} w_j K(x,q_j)u(q_j), \tag{4.47}$$

where we have discretized the domain $[0,1]$ by a set of quadrature points $\{q_j : j = 0,\ldots,n\}$, where n is even, and $\{w_j\}$ are the corresponding quadrature weights. Although the kernel K given in (4.42) and (4.35) is not smooth, all its singular points are removable. For example, via L'Hôpital's rule,

$$\lim_{x\to q}(q-x)\ln|q-x| = 0, \tag{4.48}$$

We use collocation to obtain the value of the solution at the Simpson quadrature points, i.e., we solve the system

$$u(q_i) - \sum_{j=0}^{n} w_j K(q_i,q_j)u(q_j) = -G(q_i), \quad \text{for } i = 0,\ldots,n \tag{4.49}$$

using a known iterative technique (such as Conjugate-Gradient method). This gives a numerical approximation to the Neumann boundary condition function

$$u^C_{3,2}(x,0) \approx \sum_{j=0}^{n} w_j K(x,q_j)u(q_j) + G(x) \tag{4.50}$$

which may be applied directly to the weak form (4.45).

4.6.2 Nonlocal Approach

One of the main advantages of FEM is that the assembly of the stiffness matrix can be split up over the elements, with the contribution over each element computed

locally and then added into the global matrix. For the variational problem described in Definition 2, this is exactly what is done for the first term in the bilinear form in (4.40). However, when we discretize the double integral term

$$\int_0^1 v(x,0) \int_0^1 K(x,q) \frac{\partial}{\partial y} u(q,y) \Big|_{y=0} dq\, dx \tag{4.51}$$

over the triangulation, we have to keep track of two elements: one over which the outer integral is taken and one for the inner integral. For this reason, we call this double integral *nonlocal*.

Fortunately, such nonlocal terms, like the standard local integrals, may still be computed via Gaussian quadrature. Recall that in FEM the test and solution functions are first approximated by the set of global shape functions $\{\varphi_i\}$ so that the only nonzero contributions of the double integral occur when there is shape function support over each element. Let K_1 and K_2 be two elements from our triangulation that have nonzero intersection with the crack surface Γ_C. Then we must assemble double-integral terms of the form

$$D = \int_{K_1 \cap \Gamma_C} \varphi_1(x,0) \int_{K_2 \cap \Gamma_C} K(x,q) \frac{\partial}{\partial y} \varphi_2(q,y) \Big|_{y=0} dq\, dx, \tag{4.52}$$

where φ_1 and φ_2 have support over K_1 and K_2, respectively.

Although arbitrary quadrilaterals could be used, we assume a rectangular mesh for simplicity, so that these elements have the form

$$K_1 = [a,b] \times [0,c], \qquad K_2 = [A,B] \times [0,C]. \tag{4.53}$$

We also structure the mesh so that the crack tip coincides with an element vertex. In this case, the standard bilinear mappings which transform the unit reference element

$\hat{K} = [0,1]^2$ to these real elements reduce to

$$x(\hat{x}) = a + (b-a)\hat{x}, \qquad q(\hat{q}) = A + (B-A)\hat{q}, \tag{4.54}$$

$$0 = \hat{0}, \qquad y(\hat{y}) = C\hat{y}. \tag{4.55}$$

Applying this mapping converts the double integral in (4.52) to

$$D = \int_0^1 \varphi_1(x(\hat{x}),0) \int_0^1 K(x(\hat{x}),q(\hat{q})) \frac{\partial}{\partial \hat{y}} \varphi_2(q(\hat{q}),y(\hat{y})) \Big|_{\hat{y}=0} \frac{\partial \hat{y}}{\partial y} (B-A)\, d\hat{q}\, (b-a)\, d\hat{x} \tag{4.56}$$

$$= \int_0^1 \hat{\varphi}_1(\hat{x},0) \int_0^1 K(x(\hat{x}),q(\hat{q})) \frac{\partial}{\partial \hat{y}} \hat{\varphi}_2(\hat{q},\hat{y}) \Big|_{\hat{y}=0} \frac{1}{C} (b-a)(B-A)\, d\hat{q}\, d\hat{x}, \tag{4.57}$$

where $\hat{\varphi}_1$ and $\hat{\varphi}_2$ are the corresponding reference shape functions.

Finally, we replace both integrals with a 1D Gauss quadrature formula

$$\int_0^1 f(\hat{x})\, d\hat{x} = \sum_{t=1}^{n} \hat{\omega}_t f(\hat{x}_t), \tag{4.58}$$

where $\{\hat{x}_t\}$ and $\{\hat{\omega}_t\}$ are the quadrature points and weights, respectively. This yields

$$D = (b-a)\frac{B-A}{C} \sum_{t,s}^{n} \hat{\omega}_t\, \hat{\omega}_s\, \hat{\varphi}_1(\hat{x}_t,0)\, K(x(\hat{x}_t),q(\hat{x}_s)) \frac{\partial}{\partial \hat{y}} \hat{\varphi}_2(\hat{x}_s,\hat{y}) \Big|_{\hat{y}=0}. \tag{4.59}$$

This term is assembled in the stiffness matrix as usual, with an extra loop for the second application of the quadrature rule. However, it should be noted that this will typically result in a nonsymmetric matrix. In addition, note that the kernel function K is computed at quadrature points in the real elements K_1 and K_2, not at the reference quadrature points.

In effect, this approach is doing the same thing as the Fredholm approach discussed

in Section 4.6.1, in that the interior integral is approximated using a quadrature rule. The significant difference is that in this nonlocal method, the collocation points over the surface are not solved for separately, but rather included and solved for in the global system.

4.7 Parameter Determination

The undetermined parameters in the general surface-mechanics fracture theory developed by Sendova and Walton in [47], are the surface tension constants γ_0 and γ_1. But for the fracture model and the loading condition considered in this work, γ_1 is the only undetermined parameter. This value is a material property that can be determined using calibration experiments. However, even without this calibration, we can still get an idea of the correct range for this value and for which the solution to the fracture BVP exhibits bounded crack-tip stress and strain. In this section, we will prove that there is a lower bound on this range that will guarantee bounded crack-tip stresses and a cusp-like opening profile.

We showed in Sections 4.5 and 4.6.1 that the JMB condition may be reformulated as a Fredholm equation of the second kind (4.46). In standard form, this equation is given by

$$\gamma_1 u(x) - \mathcal{K}[u](x) = -\frac{\sigma_{23}^{\infty}}{2\pi}\, g(x), \quad \text{for } \ 0 \le x \le 1, \tag{4.60}$$

where $\mathcal{K}$ is the integral operator

$$\mathcal{K}[\psi](x) = \frac{1}{\pi}\int_0^1 k(x,q)\,\psi(q)\,dq, \tag{4.61}$$

and the kernel k and data function g are given by (4.35) and (4.36), respectively.

Theorem 4.7.1. *The Fredholm integral equation in* (4.60) *has a unique, continuous solution* $u(x) \in [0,1]$ *for all but countably many values of* γ_1.

Proof. We already noted in (4.48) that $k(x,q)$ has a limit of zero when $x \to q$, and this holds even for $q = 1$. Similarly, the other logarithmic singularities are removable by their coefficients. Thus the kernel is a continuous function everywhere in $[0,1]^2$ except for the set of removable discontinuity points $S = \{(x,q)\} \in [0,1]^2 : x = \{1,q\}\}$, which is a set of measure zero in $\mathbb{R}^2$. Thus k is square integrable, i.e., $k(x,q) \in L^2([0,1]^2)$. It follows by definition that $\mathcal{K}$ is a Hilbert-Schmidt operator. As a consequence, $\mathcal{K}$ is bounded, compact, and has a countable spectrum. Applying the Fredholm Alternative, we see that (4.60) has a unique solution in $C[0,1]$ if and only if γ_1 is not an eigenvalue of $\mathcal{K}$. Since the spectrum is countable, this concludes the proof. □

Since the JMB condition requires the $u_{3,2}(x,0)$ be a solution to this Fredholm equation, then by Hooke's law, we have shown that the shear stress τ_{23} along the crack surface must be bounded for all but countably many values of γ_1. To find a lower bound for these values, we need a bound on the spectral radius of the integral operator $\mathcal{K}$, which may be obtained using the Hilbert-Schmidt norm. Thus, we require that

$$|\gamma_1| > ||\mathcal{K}||_{HS} = \frac{1}{\pi} \|k(x,q)\|_{L^2} \geq \rho(\mathcal{K}). \tag{4.62}$$

We used Mathematica® to approximate the value of this norm using double numerical integration and obtained the value $\gamma_1^{\min} = 0.1023473774$. The simulations presented below show clearly that, given $|\gamma_1| > \gamma_1^{min}$, the numerical solution and corresponding crack-tip stress/strain to the fracture BVP (4.9)-(4.12) and the reference linearized elastic model agree to high accuracy away from the crack tip. It is only near the crack tip that the two solutions differ with the linearized elastic solution exhibiting the customary square-root singularity in stress and strain while the surface-mechanics solution in stress and strain remains much smaller and bounded.

4.8 Simulation Results

In this section we investigate the numerical solution of the surface-mechanics model. In our finite element code and in all the following calculations we take the half-length of the body $b = 8$ and due to symmetry of the out-of-plane displacement the computational problem can be reduced to upper-quarter plane. In the first step the problem was solved using a uniform coarse mesh and then it was adaptively refined. A major issue in generating adaptive meshes for the computations is how to estimate which cell is to be refined or coarsened. To this end there are number of studies available in the finite element literature [4, 22] which provides a criteria for the adaptive mesh refinements. In this paper we employ a posterior error estimator developed for Laplace equation by Gago et al. [22] and the same as been implemented in the *deal.II* library. The numerical code exploits the *KellyErrorEstimator* class of the *deal.II* library to get adaptive meshes for simulations.

In our numerical code, the initial uniform coarse mesh was adaptively refined fifteen-times so that the final mesh had close to $1,000,000$ degrees of freedom, with over 1,100 elements along the crack surface. Table 4.1 shows the average number of total cells, total DOF, and number of cells over the crack surface used for a square domain with $b = 8$. The zeroth refinement cycle refers to the initial coarse mesh of the domain, which contains 64 cells and 1 cell on the crack-face. We typically ran the program for 15 refinement cycles, for which the final cycle has more than a thousand cells along the crack face.

Table 4.2 shows the convergence of the center-node displacement across the refinement cycles. Since there is only one independent displacement component, hence the center-node displacement is the value $u_3(0, 0)$.

Cycle	Total Cells	Total DOF	Crack Cells
0	64	81	1
1	124	152	2
2	238	254	4
3	454	521	8
4	865	968	16
5	1,645	1,805	32
6	3,127	3,368	58
7	5,944	6,301	97
8	11,296	11,810	121
9	21,454	22,167	188
10	40,723	41,762	230
11	77,116	78,757	364
12	145,846	148,237	438
13	276,286	279,930	627
14	522,526	528,418	896
15	987,541	997,011	1,166

Table 4.1: Total number of cells, degree of freedom and crack cells for each refinement cycles of the square domain

Cycle	$\gamma_1 = 0.0$	$\gamma_1 = 0.5$	$\gamma_1 = 1.0$	$\gamma_1 = 2.0$	$\gamma_1 = 4.0$
0	0.00089573	0.00014256	7.12801e-05	3.56401e-05	1.78236e-05
1	0.000915728	0.000164825	8.24126e-05	4.12063e-05	2.06032e-05
2	0.000958142	0.0001677034	8.35169e-05	4.17585e-05	2.08792e-05
3	0.000981447	0.000167313	8.36565e-05	4.18283e-05	2.091412e-05
4	0.00099378	0.00016735	8.36752e-05	4.18376e-05	2.09188e-05
5	0.00100012	0.000167357	8.36786e-05	4.18393e-05	2.09196e-05
6	0.0010034	0.000167362	8.36812e-05	4.18406e-05	2.09203e-05
7	0.00100506	0.00016737	8.36848e-05	4.18424e-05	2.09212e-05
8	0.00100535	0.000167376	8.36881e-05	4.1844e-05	2.09222e-05
9	0.00100591	0.00016738	8.36902e-05	4.18451e-05	2.09225e-05
10	0.00100633	0.000167382	8.36904e-05	4.18456e-05	2.09225e-05
11	0.00100655	0.000167382	8.36909e-05	4.18459e-05	2.09225e-05
12	0.00100666	0.000167382	8.36911e-05	4.18459e-05	2.09225e-05
13	0.00100676	0.000167382	8.36911e-05	4.18459e-05	2.09225e-05
14	0.00100676	0.000167382	8.36911e-05	4.18459e-05	2.09225e-05
15	0.00100676	0.000167382	8.36911e-05	4.18459e-05	2.09225e-05

Table 4.2: Convergence of the center node displacement for various surface tension parameter γ_1 across refinement cycles.

4.8.1 Error Reduction Factor

Here we study "Error Reduction Factor" similar to the one studied for the nonlinear problem in Chapter 3. For the anti-plane strain problem studied here, the quantity ERF is defined through the relationship as:

$$\text{ERF} = \frac{|u_3^{LR}(0,0) - u_3^{i}(0,0)|}{|u_3^{LR}(0,0) - u_3^{i-1}(0,0)|}, \quad i = 2, 3, \ldots LR, \tag{4.63}$$

in which the term $u_3^{LR}(0,0)$ denotes the center-node displacement of the out-of plane displacement component $u_3(x_1,\, x_2)$ at the last-refinement and we compute this quantity as a function of the number of degrees of freedom. The computed quantity, ERF, is approximately 2.0, which is reasonable for the linear finite element. Figure 4.3 depicts the *log-log* plot of the difference in the *error*, which is the difference in the center-node displacement $(u_3(0,\ 0))$ of the current refinement level with the last refinement level. We notice that the error is reduced considerably for the higher values of the surface-tension modeling parameter γ_1.

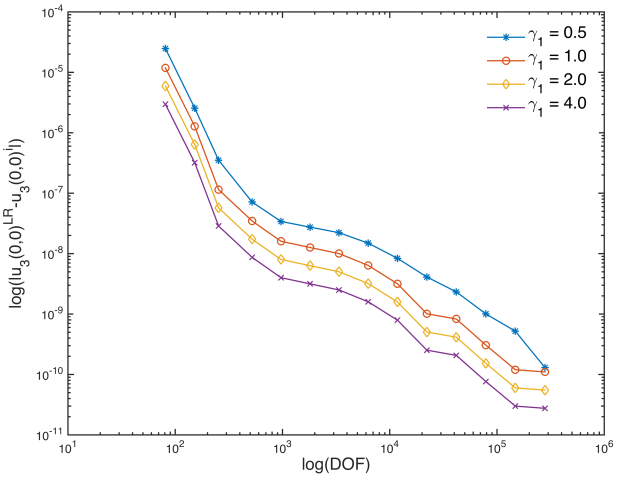

Figure 4.3: The *log-log* plot of the error as a function of the degrees of the freedom.

Figures 4.4 and 4.5 shows the solution of the Fredholm integral equation (4.46) for various values of the surface-tension parameter γ_1. Figure 4.4 indicates the solution reduces considerably for the values of γ_1 greater than the lower bound of the Hilbert-Schmidt norm $\gamma_1^{\min}$.

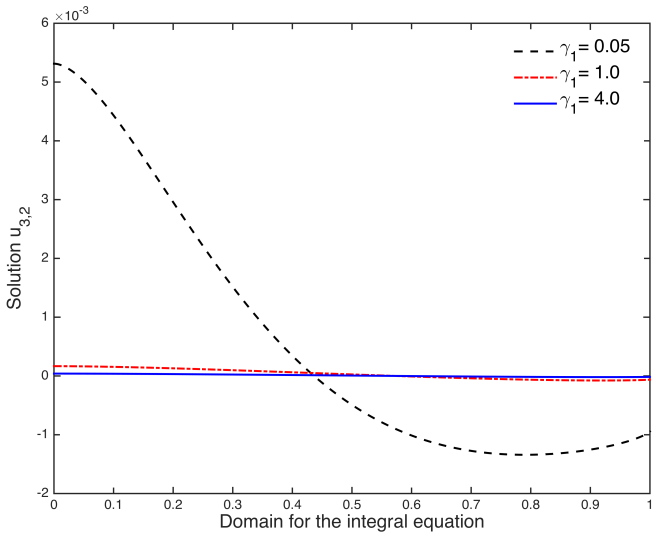

Figure 4.4: Solution of the integral equation for different values of γ_1.

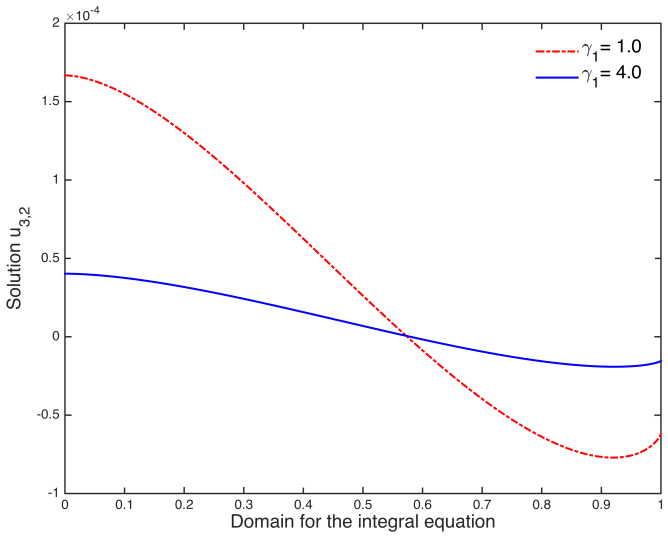

Figure 4.5: Solution of the integral equation for values of γ_1 greater than $\gamma_1^{\min}$.

Figure 4.6 depicts the solution of (4.38) for the parameters $\sigma_{23}^{\infty} = 0.001$ and $\gamma_1 = 1$. The solution plot depicts that the displacements are larger on the crack-surface than on far-away region in the domain and the plot also shows the displacement in the entire body including the applied boundary condition from the symmetry.

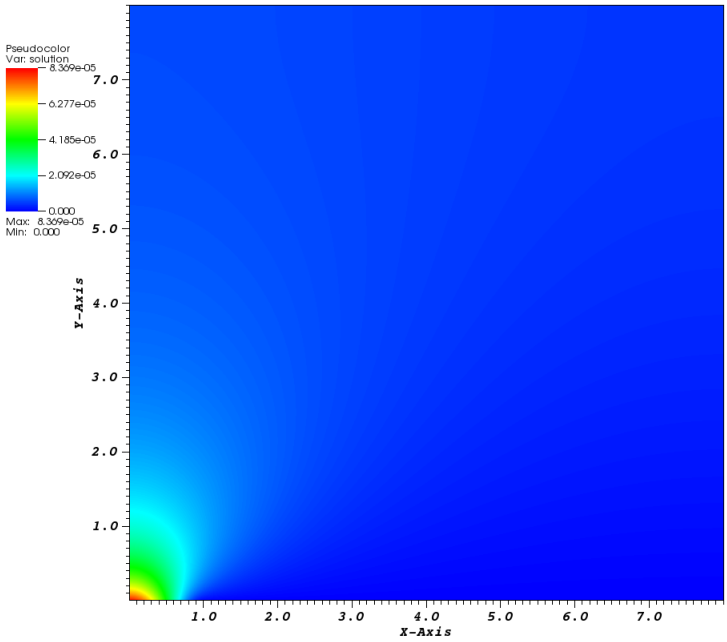

Figure 4.6: 2D plot of the solution for the parameters $\sigma_{23}^{\infty} = 0.001$ and $\gamma_1 = 1$.

Figure 4.7 shows the comparison of the two method implemented and both methods agree very well. The l^2-norm of the difference of the solution on the crack-surface is 1.5286E−05 and it is considered as reasonable as the two methods uses different quadrature points. For the remainder of this section, all results were obtained using the nonlocal FEM implementation. The Figure 4.7 is consistent with the cusp-shaped displacement profile predicted by the theoretical results [47]. Figure 4.8 demonstrates how the surface tension parameter γ_1 affects the crack-opening displacement. Even for the small surface-tension parameter the crack-profile is a nice cusp-shaped and the crack-faces closes with a sharp crack-tip, which is a great improvement in the corresponding prediction from LEFM.

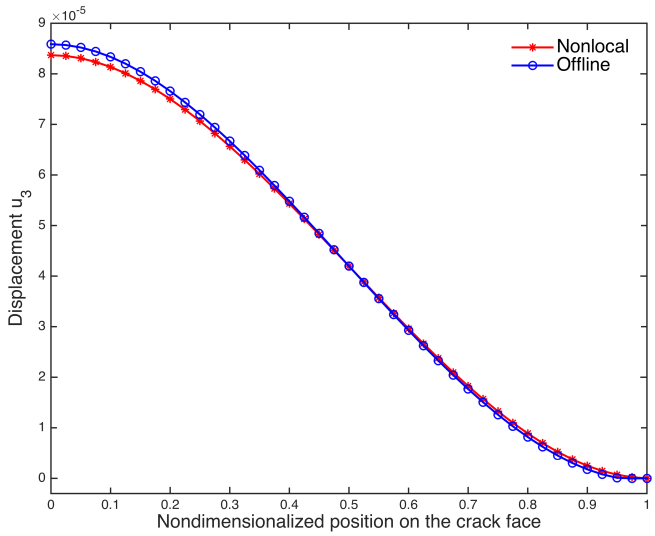

Figure 4.7: Comparison of both FEM implementations and parameters used in the computations are $\sigma_{23}^{\infty} = 0.001$ and $\gamma_1 = 1$.

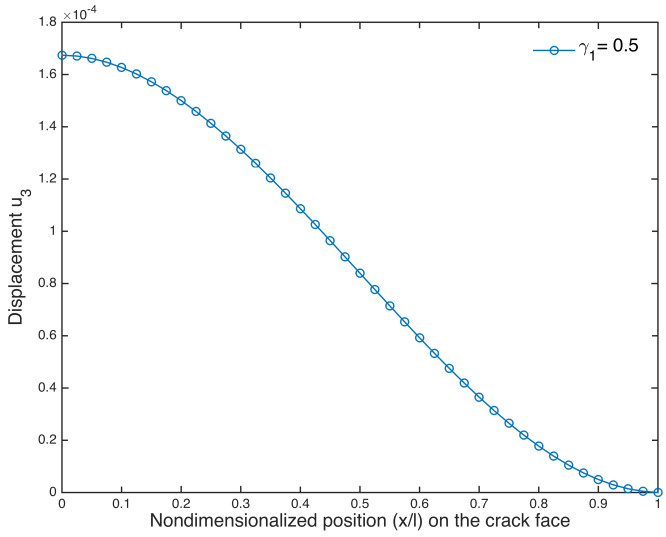

Figure 4.8: Crack-opening displace profile for the surface-mechanics model with parameter values $\sigma_{23}^{\infty} = 0.001$ and $\gamma_1 = 0.5$.

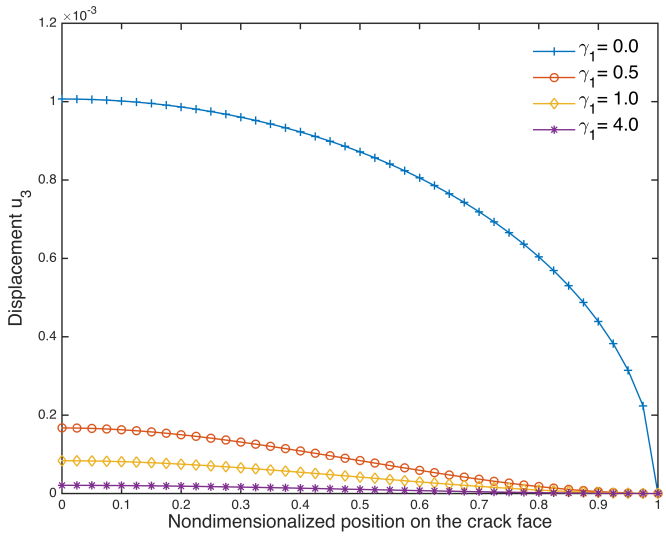

Figure 4.9: Crack-surface displacement (u_3) for various values surface-tension parameter and fixed $\sigma_{23}^{\infty} = 0.001$.

Figure 4.9 demonstrates the effect of the surface tension parameter on the crack-surface solution. We observe that for $\gamma_1 = 0.0$ the crack-surface is elliptical (which is same of the LEFM crack-surface prediction) and for the higher values of γ_1 the crack-surface is cusped opening shape with significantly reduced displacement. Hence one can recover the classical LEFM elliptical solution for $\gamma_1 = 0.0$. Even for smaller nonzero values of γ_1 we see cusping although the rest of the surface profile is closer to the standard elliptical LEFM solution. Figure 4.10 depicts the near-tip stress τ_{23} both for LEFM and surface-mechanics model. It is clear from the graph that our LEFM numerical results are consistent with the classical $\frac{1}{\sqrt{1-x}}$ stress singularity. An important observation from Figure 4.10 is that in the case of surface-mechanics model, the near-tip stress values are orders of magnitude smaller compared with the corresponding predictions of LEFM. This result is in good agreement with the previous studies concerning the stress-concentration at the straight mode-I [47] and mixed-mode

(combination of pure mode-I and mode-II) [53] crack-tips.

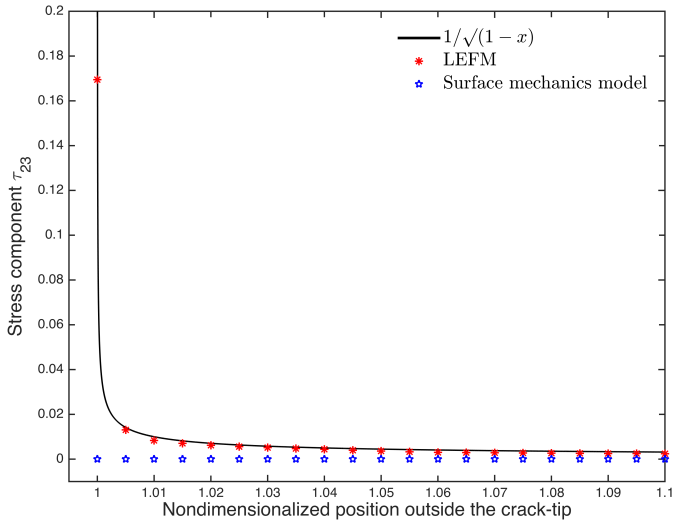

Figure 4.10: Comparison of the near-tip stress component τ_{23} for LEFM and surface-mechanics model with parameter values $\sigma_{23}^{\infty} = 0.001$ and $\gamma_1 = 1.0$.

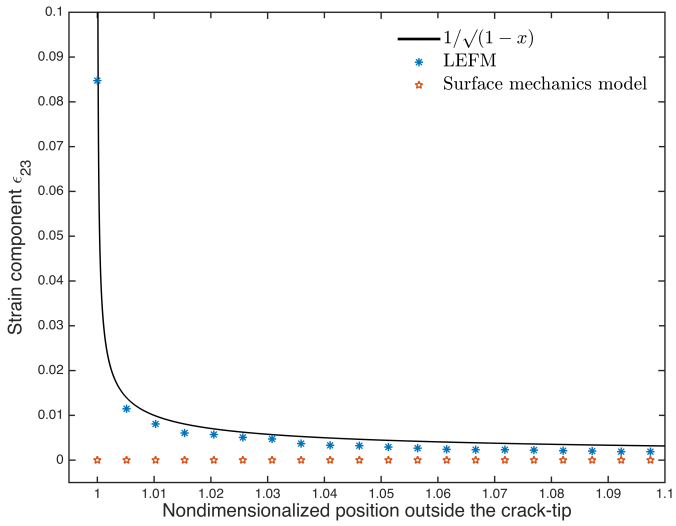

Figure 4.11: Comparison of the near-tip strain component ϵ_{23} for LEFM and surface-mechanics model with parameter values $\sigma_{23}^{\infty} = 0.001$ and $\gamma_1 = 1.0$.

The near-tip strain component ϵ_{23} both for LEFM and surface-mechanics model is shown in Figure 4.11. As in Figure 4.10 the LFEM numerical results are very close to the classical $\frac{1}{\sqrt{1-x}}$ singularity. But the surface-mechanics model, as proved theoretically in [47], predicts bounded crack-tip strains. The computations for both Figures 4.10 and 4.11 are done with the surface-tension parameter $\gamma_1 = 1.0$, but one can recover the classical singular stress-strain singularity with $\gamma_1 = 0.0$.

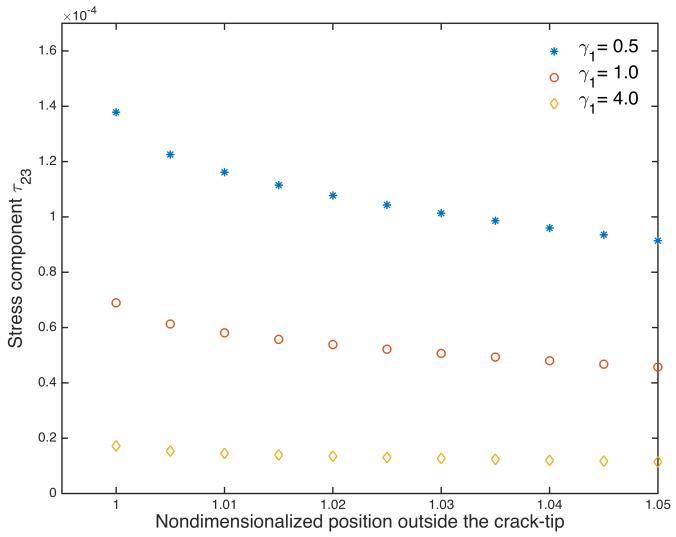

Figure 4.12: Near-tip stress component τ_{23} for various values surface-tension parameter and fixed $\sigma_{23}^{\infty} = 0.001$

Stress component τ_{23} obtained, for increasing surface-tension parameter γ_1, along line directly ahead of the crack-tip is depicted in Figure 4.12. It is clear from the graph that the near-tip stress decreases with increasing value of γ_1. Higher values of γ_1 decreases the crack-face displacement as depicted in Figure 4.9 and also overall displacement in the body. Hence the near-tip stresses are small even very near the crack-tip.

Effect of top-face shear-load on the crack-surface displacement u_3 is shown in Figure 4.13. The crack-face displacement increases with the increasing load. Also another important result of the present investigation is that the surface-mechanics model predicts the crack-faces closed with a sharp crack-tip. In addition, Figure 4.14 depicts the effect of top-face shear-load on the near-tip stress component τ_{23} and graph also indicates that increase in top-face load increases the near-tip stresses.

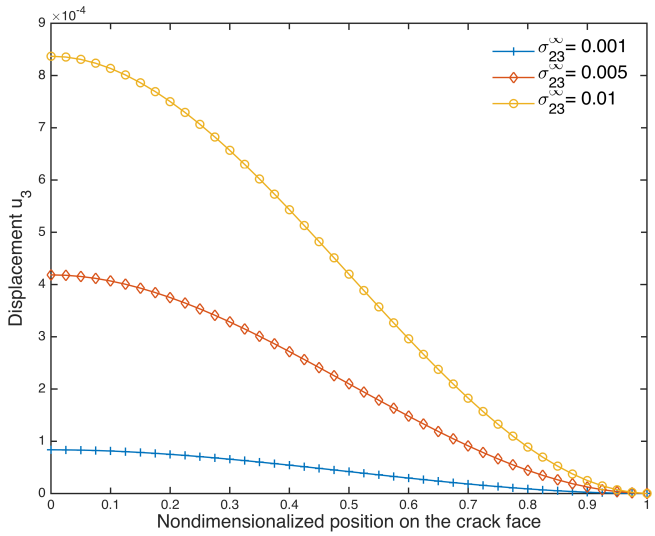

Figure 4.13: Effect of shear-load on the crack-surface displacement u_3 and $\gamma_1 = 1$

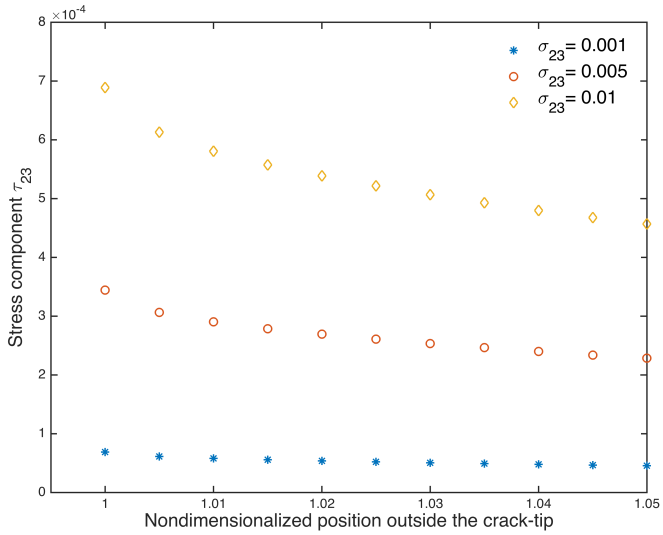

Figure 4.14: Effect of shear-load on the near-tip stress component τ_3 and $\gamma_1 = 1$

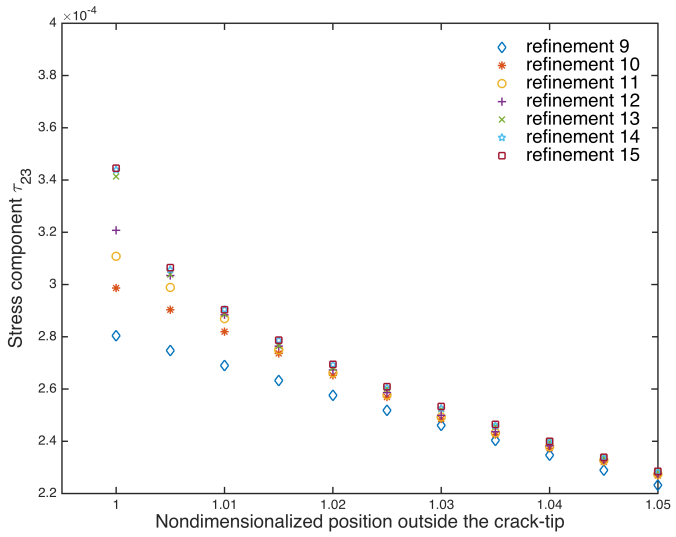

Figure 4.15: Convergence of the stress component τ_{23} for parameter value $\gamma_1 = 1$

Figure 4.15 shows the convergence of the numerical-value of stress component τ_{23} for the various refinement levels. The adaptive refinements of the computational domain increases the mesh density in the neighborhood of the crack-tip and there by approximating the crack-tip singularity very well.

4.9 Conclusions

In this contribution, we have demonstrated an approach for the numerical implementation of the surface-mechanics model using FEM. Modeling crack-surface excess property leads to higher order tangential derivatives [47,48,53] and the implementation using stable numerical method such as finite elements was not addressed previously. In this chapter, we have developed an approach to reformulate the JMB condition using boundary Green's function and the Dirichlet to Neumann map. The reformulated boundary condition for the Neumann data reduces to Fredholm second kind integral equation. The actual FEM implementation was conducted using two slightly different

methods. In the first, the reformulated JMB condition was solved separately to obtain a numerical approximation to the Neumann condition on the crack surface, which was then included using a standard FEM procedure. In the second, a nonlocal FEM computation was employed to include the Neumann condition directly.

In Section 4.8 we have shown that both the FEM implementations agree well with each other. A nonzero curvature-dependent surface tension produces bounded crack-tip stress and a cusp-like crack opening profile. Another important result of the present investigation that the crack-faces closes with a sharp crack-tip. All of which are in marked distinction with the classical linearized elasticity model.

5. CONCLUSIONS AND FUTURE WORK

In this chapter, we summarize the main contents along with the contributions of this dissertation and briefly discuss possible future work.

5.1 Summary

This dissertation has presented the asymptotic and numerical study of two brittle fracture theories. The class of response relations used for formulating the strain-limiting elasticity theory utilizes a nonlinear relation between linearized strain tensor and Cauchy stress tensor. The general class of implicit elasticity models were introduced by Rajagopal in [34]. The linearization of implicit nonlinear models always leads to linearized strain as a nonlinear function of Cauchy stress. But the same procedure for the traditional Cauchy or Green elastic models give rise to the classical linearized elasticity relations in the infinitesimal strain limit. Also the classical elastic model predicts that the strains, in the neighborhood of the crack-tip, varies like $\frac{1}{\sqrt{r}}$ (where r is the radial distance from the crack-tip). Therefore crack-tip strain singularity violates the basic assumption through which the classical model has been derived. But the new class of response relations introduced by Rajagopal [34–37, 39, 40] restrict the strains uniformly to a physically realistic level. In a recent paper [41] Rajagopal and Walton initiated a study of brittle fracture for a single anti-plane shear crack, using a class of strain-limiting nonlinear constitutive models. They showed that the new theory not only removes the classical square-root order singularity in strains but also predicts bounded stresses in the vicinity of the crack-tip.

In Chapter 2, we extend the previous study of the brittle fracture in the context of strain-limiting theory of elasticity to a more challenging plane-strain fracture setting. The problem considered in Chapter 2 was that of a single, plane-strain crack in

an infinite planar body governed by strain-limited infinitesimal fracture model. The model incorporates the classical boundary conditions. Our main aim was to investigate whether the fracture BVP admits singular crack-tip stress behavior. We presented arguments based upon asymptotic and numerical techniques that the limiting strain model considered does not admit crack-tip stress singularity within the specified class of expansions. There remains open to develop a vector valued finite element based solution algorithm because the asymptotic study only give some qualitative nature of the solution near the crack-tip.

A finite element model for the plane-strain pure mode-I fracture is presented in Chapter 3. The main purpose of the work presented in Chapter 3 was to study a stable numerical implementation of the nonlinear strain-limiting anisotropic response relations combined with the classical fracture boundary conditions. Using a inverted nonlinear constitutive relation and equilibrium equation, we obtain a system of second order quasilinear PDEs. The linearized version of the strong form was derived using damped Newton's method and a conforming finite element formulation was utilized to get the numerical solution. The numerical results indicate that even very near the crack tip, both stress and strain remain much smaller in magnitude than the corresponding predictions from linearized elastic fracture mechanics (LEFM). Also of interest was the behavior of the cleavage stress near the crack-tip and same has been studied for the pure mode-I problem in [47]. The obtained results show that the cleavage stress is $\sigma_{\theta\theta}$ as a monotonically decreasing function of θ (where θ is the polar angle), with the maximum occurs at $\theta = 0.0$.

In the second part of the dissertation (ie in Chapter 5), we study the numerical implementation of the recently developed continuum-surface mechanics model. The fracture-surface is modeled as a two dimensional *dividing surface* endowed with excess property (such as surface tension) and the material behavior in the bulk phase is

modeled by the classical linearized elasticity. However, such approach leads to higher-order tangential derivative on the crack-surface and a numerically stable finite element implementation was not straight forward, because the shape functions needed higher regularity on one part of the domain compared with the rest of the domain. We propose a reformulation of the crack-surface boundary condition as a Fredholm second kind integral equation and for the actual FEM implementation we studied two different approaches. In the first, the Fredholm integral equation was solved separately using product trapezoidal rule and then explicit Neumann data was utilized directly in the FEM simulation. In the second approach, the nonlocal boundary condition was utilized directly in the assembly of the global system during the standard FEM procedure. Both FEM implementations agree each other well and more importantly both approaches predict bounded crack-tip stress and strain. Also, a nonzero curvature-dependent surface tension produces cusp-like crack opening surface and the crack-faces closes with a sharp crack-tip.

5.2 Future work

In this dissertation, we successfully demonstrated an approach for implementing the curvature-dependent surface tension excess property continuum-surface model. The numerical results demonstrate that, for a single anti-plane strain crack, both the crack-tip stress/strain are bounded and also predict a cusp-shaped crack-opening profile with a sharp crack-tip. A similar reformulation and numerical approach can be applied for more complicated geometries such as mode-I and mixed-mode fracture problems. For a more challenging plane-strain mixed mode fracture, the curvature-dependent surface tension model takes the form:

$$\tilde{\gamma} := \gamma_0 + \gamma_1 H(X_1) \tag{5.1}$$

in which $H(X_1)$ denotes the mean-curvature of the deformed upper crack-surface. The linearized form of $H(X_1)$ takes the form

$$H(X_1) = u_{2,11}(X_1, 0^+) + \text{h.o.t.} \tag{5.2}$$

Then the corresponding linearized JMB equations along with superposition of far-field loading yields

$$\sigma_{22}(X_1, 0) = -\tilde{\gamma}\, u_{2,11}(X_1, 0) - \sigma_{22}^{\infty} \tag{5.3}$$

$$\sigma_{12}(X_1, 0) = -\tilde{\gamma}\,'(X_1) - \sigma_{12}^{\infty} \tag{5.4}$$

for $|X_1| < 1$. Then in [53] a modified surface tension model was studied and takes the form

$$\gamma = \gamma_0 + \gamma_1\, u_{1,1}(X_1, 0) + \gamma_2\, u_{1,111}(X_1, 0) + \gamma_3\, u_{2,11}(X_1, 0). \tag{5.5}$$

For the mixed-mode problem the only symmetry that exists is that the displacement vector field is symmetric through the origin. That is

$$\boldsymbol{u}(-X_1, -X_2) = -\boldsymbol{u}(X_1, X_2). \tag{5.6}$$

Hence the problem can be studied in upper-half plane. The differential momentum balance yields a standard equilibrium equation, given by

$$\operatorname{Div} \mathbf{T} = \mathbf{0}, \tag{5.7}$$

in which the Cauchy stress tensor is given by

$$\mathbf{T}(\boldsymbol{u}) = 2\,\boldsymbol{\epsilon}(\boldsymbol{u}) + \nu \operatorname{tr}(\boldsymbol{\epsilon}(\boldsymbol{u}))\,\mathbf{I}. \tag{5.8}$$

The weak formulation can be obtained by multiplying (5.7) by a test function $\boldsymbol{v}$ and integrate over domain

$$a(\boldsymbol{u}, \boldsymbol{v}) - \int_{\Gamma^c} \boldsymbol{v} \cdot \mathbf{T}\mathbf{n} = 0, \tag{5.9}$$

where $a(\cdot, \cdot)$ is the standard elasticity bilinear form, Γ_c is the crack-face and $\mathbf{n}$ is the normal vector. The boundary term vanishes everywhere except the crack surface, so that the resulting weak form is given by

$$a(\boldsymbol{u}, \boldsymbol{v}) + \int_{\Gamma^c} \gamma_0 u_{2,1}\, v_{2,1} + \int_{\Gamma^c} \sigma_{12}^c\, v_1 = \int_{\Gamma^c} \sigma_{22}^\infty\, v_2, \tag{5.10}$$

for the term σ_{12}^c we can use Hooke's law and rewriting the above equation:

$$a(\boldsymbol{u}, \boldsymbol{v}) + \int_{\Gamma^c} \gamma_0 u_{2,1}\, v_{2,1} + \int_{\Gamma^c} (u_{1,2} + u_{2,1})\, v_1 = \int_{\Gamma^c} \sigma_{22}^\infty\, v_2 \tag{5.11}$$

$$a(\boldsymbol{u}, \boldsymbol{v}) + \int_{\Gamma^c} \gamma_0 u_{2,1}\, v_{2,1} + \int_{\Gamma^c} u_{1,2}\, v_1 + \int_{\Gamma^c} u_{2,1}\, v_1 = \int_{\Gamma^c} \sigma_{22}^\infty\, v_2, \tag{5.12}$$

The main issue at hand is to reformulate the boundary condition (5.4) for $u_{2,1}$. To this end one make use of the approach developed in this dissertation and the resulting weak form will not contain any higher order tangential derivatives. Another question is to find the domain in which the parameters of the curvature-dependent surface tension may vary, so that the model yields a physically reasonable solution for the crack profile.

Another interesting problem within the context of surface-mechanics fracture models is to include body force correction term along with bulk material response relations. In [46] it was conjectured that the incorporation of a mutual body force term leads to a compact perturbation of the singular integro-differential operator after linearization of the jump momentum balance boundary conditions under the assumption of small strains. The question is to verify whether the compact operator yields bounded

stresses and strains and a cusp-shaped crack opening profile. Another direction in which the analysis and the computational approach developed in both [19, 46] can be extended to the case of 3D cracks and interfacial fracture problems.

Further, there are several research opportunities motivated by the research on implicit constitutive material models by Rajagopal and subsequent use of sub-class of implicit models (such as strain-limiting elasticity models) in brittle fracture modeling ([41], [23]). One can extend the finite element implementation proposed in this disseration to the more general theory of fracture developed by Sendova and Walton in [47] for the nonlinear elasticity and nonlinear surface-mechanics. Simultaneously one can study, along with an appropriate fracture criterion, crack-growth and propagation within the context of both fracture models studied in this dissertation. Also, another interesting problem within the context of the two theories studied in this dissertation is the penny-shaped crack. The 3D elasticity problems are ultimately interesting to explore using the two modeling approaches studied in this dissertation.

REFERENCES

[1] F. F. Abraham, *The atomic dynamics of fracture,* J. Mech. Phys. Solids, 49 (2001), pp. 2095-2111.

[2] K. E. Atkinson, *The numerical solution of integral equations of the second kind,* volume 4 of Cambridge Monographs on Applied and Computational Mathematics, Cambridge University Press, Cambridge, 1997.

[3] W. Bangerth, Video lectures on *deal.II* library, Video Lectures for Math 676, Spring 2013, Texas A&M University. All the video lectures can accessed through the website `http://www.math.tamu.edu/~bangerth/videos.html`.

[4] W. Bangerth and R. Rannacher, *Adaptive Finite Element Methods for Differential Equations*, Birkhäuser Verlag, 2003.

[5] W. Bangerth, R. Hartmann, and G. Kanschat, *deal.II – A general-purpose object-oriented finite element library,* ACM Trans. Math. Softw., 33-4 (2007), pp. 24/1-24/27.

[6] W. Bangerth, T. Heister, L. Heltai, G. Kanschat, M. Kronbichler, M. Maier, B. Turcksin and T. D. Young, *The deal.II Library, Verion 8.1,* arXiv preprint, URL `http://arxiv.org/abs/1312.2266v4`, 2013.

[7] R. C. Bridges, *Implicit rate-type models for elastic bodies: development, integration, linearization and application*, Ph. D. dissertation, Texas A&M University, College Station, TX, 2011.

[8] R. C. Bridges and K. R. Rajagopal, *Implicit constitutive models with a thermodynamic basis: a study of stress concentration,* ZAMP, 66 (2015), pp. 191-208.

[9] K. B. Broberg, *Cracks and fracture*, Academic Press, 1999.

[10] M. Bulíček, J. Málek, E. Süli, *Analysis and approximation of a strain-limiting nonlinear elastic model,* Math. Mech. Solids, 20-1, (2015), pp. 92-118.

[11] M. Bulíček, J. Málek, K. R. Rajagopal and E. Süli, *On elastic solids with limiting small strain: modelling and analysis,* Eur. Math. Soc. S. M. Sci., 1-4, (2014), pp. 283-332.

[12] M. Bulíček, J. Málek, K. R. Rajagopal and J. R. Walton, *Existence of solutions for the anti-plane stress for a new class of 'strain-limiting' elastic bodies,* in press Calc. Var.& Part. Diff. Eqns, DOI 10.1007/s00526-015-0859-5.

[13] R. Bustamante and K. R. Rajagopal, *A note on plane strain and plane stress problems for a new class of elastic bodies,* Math. Mech. Solids, 15-2 (2010), pp. 229-238.

[14] R. Bustamante and K. R. Rajagopal, *Solutions of some simple boundary value problems within the context of a new class of elastic materials,* Int. J. Non-Lin. Mech., 46-2 (2011), pp. 376-386.

[15] R. Bustamante and K. R. Rajagopal, *On the inhomogeneous shearing of a new class of elastic bodies,* Math. Mech. Solids, 17-7 (2012), pp. 762-778.

[16] R. Bustamante and K. R. Rajagopal, *On a new class of electroelastic bodies I,* Proc. R. Soc. Lond. A, 469-2149, (2013).

[17] R. Bustamante and K. R. Rajagopal, *On a new class of electroelastic bodies II. Boundary value problems,* Proc. R. Soc. Lond. A, 469-2155, (2013).

[18] A. Ern and J-L. Geurmond, *Theory and practice of finite elements*, Spinger-verlag, New-York, ISBN-978-0-387-20880-0, 2004.

[19] L. A. Ferguson, *Brittle fracture modeling with a surface tension excess property*, Ph. D. dissertation, Texas A&M University, College Station, TX, 2012.

[20] L. A. Ferguson, M. Muddamallappa and J. R. Walton, *Numerical simulation of mode-III fracture incorporating interfacial mechanics,* Int. J. Frac., 192 (2015), pp. 47-56.

[21] E. E. Gdoutos, *Fracture mechanics: an introduction*, Springer, 2005.

[22] J. P. de S. R. Gago, D. W. Kelly, O. C. Zienkiewicz and I. Babuška, *A posteriori error analysis and adaptive processes in the finite element method: Part II - Adaptive Mesh Refinement,* Int. J. Num. Meth. Eng., 19 (1983), pp. 1621-1656.

[23] K. Gou, M. Mallikarjuna, K. R. Rajagopal and J. R. Walton, *Modeling fracture in the context of a strain-limiting theory of elasticity: A single plane-strain shear crack,* Int. J. Eng. Sci., Special Issue on "Qualitative Methods in Engineering Science", 88 (2015), pp. 73-82.

[24] M. E. Gurtin, *An introduction to continuum mechanics*, Academic Press, New York, 1981.

[25] C. Grossmann, H.-G. Ross, and M. Stynes, *Numerical treatment of partial differential equations*, Springer-Verlag, 2007.

[26] V. Kulvait, J. Málek and K. R. Rajagopal, *Anti-plane stress state of a plate with a V-notch for a new class of elastic solids,* Int. J. Frac., 179 (2013), pp. 59-73.

[27] M. Kambapalli, K. Kannan and K. R. Rajagopal, *Circumferential stress waves in a non-linear cylindrical annulus in a new class of elastic materials,* Q. J. Mech. App. Mech, 67-2, (2014), pp. 193-203.

[28] T.-N. Mai and J. R. Walton, *On strong ellipticity for implicit and strain-limiting theories of elasticity,* Math. Mech. Solids., 20-2 (2015), pp. 121-139.

[29] T.-N. Mai and J. R. Walton, *On monotonicity for strain-limiting theories of elasticity,* J. Elasticity, 120 (2015), pp. 39-65.

[30] N. Moes, J. Dolbow and T. Belytschko, *A finite element method for crack growth without remeshing,* Int. J. Numer. Meth. Engng., 46, (1999), pp. 131150.

[31] E.-S. Oh, J. R. Walton, and J. C. Slattery, *A theory of fracture based upon an extension of continuum mechanics to the nanoscale,* J. Appl. Mech., 73-5 (2008), pp. 792798.

[32] A. Ortiz, R. Bustamante, and K. R. Rajagopal, *A numerical study of a plate with a hole for a new class of elastic bodies,* Acta Mech., 223-9 (2012), pp. 1971-1981.

[33] A. Ortiz, R. Bustamante, and K. R. Rajagopal, *A numerical study of elastic bodies that are described by constitutive equations that exhibit limited strains,* Int. J. Solids Structures, 51 (2014), pp. 875-885.

[34] K. R. Rajagopal, *The elasticity of elasticity,* ZAMP, 58-2 (2007), pp. 309-317.

[35] K. R. Rajagopal, *On a new class of models in elasticity,* Math. & Comp. App., 15 (2010), pp. 506-528.

[36] K. R. Rajagopal, *Non-linear elastic bodies exhibiting limiting small strain,* Math. Mech. Solids, 16-1 (2011), pp. 122-139.

[37] K. R. Rajagopal, *Conspectus of concepts of elasticity,* Math. Mech. Solids, 16-5 (2011), pp. 536-562.

[38] K. R. Rajagopal, *Particle-free bodies and point-free spaces,* Int. J. Eng. Sci., 72 (2013), pp. 155-176.

[39] K. R. Rajagopal, *On the nonlinear elastic response of bodies in the small strain range,* Acta Mech., 225 (2014), pp. 1545-1553.

[40] K. R. Rajagopal and A. R. Srinivasa, *On the response of non-dissipative solids,* Proc. R. Soc. Lond. A, 463 (2007), pp. 357-367.

[41] K. R. Rajagopal and J. R. Walton, *Modeling fracture in the context of a strain-limiting theory of elasticity: A single anti-plane shear crack,* Int. J. Frac., 189-1 (2011), pp. 39-48.

[42] S. M. Mallikarjunaiah and J. R. Walton, *On the direct numerical simulation (DNS) of an anti-plane shear crack in a new class of elastic bodies,* Proceedings of US National Congress on Theoretical and Applied Mechanics, 2014.

[43] S. M. Mallikarjunaiah and J. R. Walton, *On the direct numerical simulation of plane-strain fracture in a class of strain-limiting anisotropic elastic bodies,* Int. J. Frac., 192 (2015), pp. 217-232.

[44] S. M. Mallikarjunaiah and J. R. Walton, *On the interaction of an anti-plane shear wave with a re-entrant notch in a strain limiting nonlinear elastic body,* under review.

[45] M. H. Sadd, *Elasticity: theory, applications and numerics,* second edition, Elsevier, 2009.

[46] T. Sendova, *A new approach to the modeling & analysis of fracture through an extension of continuum mechanics to the nanoscale,* Ph. D. dissertation, Texas A&M University, College Station, TX, 2008.

[47] T. Sendova and J. R. Walton, *A new approach to the modeling and analysis of fracture through extension of continuum mechanics to the nanoscale,* Math. Mech. Solids, 15-3 2010, pp. 368-413.

[48] T. Sendova and J. R. Walton, *The Effect of Surface Tension in Modeling Interfacial Fracture,* AIP Conf. Proc., Vol. 1301 (2010), pp. 291 - 300.

[49] J. C. Slattery, E.-S. Oh and K. B. Fu, *Extension of continuum mechanics to the nanoscale,* Chem. Eng. Sci., 59-21 (2004), pp. 4621-4635.

[50] S. A. Silling, *Reformulation of elasticity theory for discontinuities and long-range forces,* J. Mech. Phys. Solids, 48 (2000), pp. 175209.

[51] J. R. Walton, *Lecture notes on Linear Algebra, Tensor Algebra and Tensor Calculus,* Lecture notes for Math 603, Fall 2012, Texas A&M University.

[52] J. R. Walton, *A note on fracture models incorporating surface elasticity,* J. Elasticity, 109-1 (2012), pp. 95-102.

[53] J. R. Walton, *Plane-strain fracture with curvature-dependent surface tension: mixed-mode loading,* J. Elasticity, 114-1 (2014), pp. 127-142.

[54] S-Q. Zhang, S.-J. Li, M.-T. Jia, Y. L. Hao, and R. Yang, *Fatigue properties of a multifunctional titanium alloy exhibiting nonlinear elastic deformation,* Scripta Materialia, 60 (2009), pp. 733-736.